Photonic antennas to boost the light and chiral matter interactions

Lingfei Cui

To cite this version:

Lingfei Cui. Photonic antennas to boost the light and chiral matter interactions. Materials Science [cond-mat.mtrl-sci]. Sorbonne Université, 2023. English. NNT : 2023SORUS392 . tel-04379318

HAL Id: tel-04379318
https://theses.hal.science/tel-04379318

Submitted on 8 Jan 2024

Sorbonne Université

Physique et Chimie des Matériaux (ED 397)

L'Institut des NanoSciences de Paris (INSP) / Nanostructures et optique

Antennes photoniques pour amplifier les interactions entre la lumière et la matière chirale

Par Lingfei CUI

Thèse de doctorat de la physique, de la particule à la matière condensée

Dirigée par Bruno GALLAS et Mathieu MIVELLE

à l'Institut des NanoSciences de Paris

Soutenance le 8 Décembre 2023

Devant un jury composé de :

BAUDRION, Anne-Laure	Maître de Conférence	(Rapporteure)
BATTIE, Yann	Professeur	(Rapporteur)
PARIGI, Valentina	Professeure	(Présidente)
PELLARIN, Michel	Directeur de recherche	(Examinateur)
MIVELLE Mathieu	Chargé de Recherche	(Directeur de thèse)
GALLAS Bruno	Chargé de Recherche	(Directeur de thèse)

Contents

Chapter 1 Introduction

1.1 Motivation

The detection of molecules based on fluorescence or Raman scattering has been widely studied and is currently used in industry and laboratories. However, many organic molecules of interest are chiral, and their chemical and biological properties depend on their enantiomer as well as on the chirality of their secondary structure. The quantity and chirality of biomolecules are classically determined by measuring the differential absorption between the two opposite circular polarizations (chiroptic method). However, this method is limited by the low differential absorption of chiral molecules, which is of the order of 10^{-3} in the UV part of the spectrum. Plasmonic resonators have the ability to resonantly interact with light and are characterized by a moderate quality factor and a low effective volume. This resonant interaction allows (i) to increase the coupling between molecules and light and (ii) to control the polarization properties of light. So far, the latest advances concern the implementation of nanostructured chiral surfaces with gammadion-type resonators [1,2,3] or stacked twisted resonators[4] that interact preferentially with a given helicity of light. However, the mechanism behind the differential response of biomolecules coupled to chiral resonators to circularly polarized light is still unclear, preventing the optimization of such detection. Moreover, in the research published so far, two different chiral sensors are needed to interact with right- and left-handed circularly polarized light, which requires complex calibration procedures. During the course of my PhD, I have studied the use of anisotropic achiral nanostructures to interact with chiral molecules. Indeed, they have the significant advantage over chiral nanostructures of changing the sign of the circular dichroism by controlling the incident polarization or the direction of propagation.[5,6] Indeed, the symmetries of the electromagnetic field in close proximity to the resonators can be manipulated at will by changing illumination conditions hence providing a unique tool for studying the origin of the electromagnetic coupling between chiral biomolecule and nanoresonators.

Consequently, in my PhD project I propose to use plasmonic nanoresonators to increase the light - “chiral matter” interactions in order to detect and study chiral molecules. I will use the concept of achiral plasmonic nanostructures (nanoslits) to develop innovative nanoresonators that will be used, once functionalized, to detect chiral biomolecules with enantiomer sensitivity. Indeed, achiral resonators can generate both signs of chiral fields as opposed to chiral resonators which would make their use very flexible. This work implies characterizing, describing and understanding the origins of chiral fields and how to make them homogeneous. Through the study of nanoslits, I demonstrate numerically and theoretically how to design a nanosource of pure superchiral light, free of any background and for which the sign of the chirality is tunable on-demand in wavelength and polarization. In the perspective, I will present experimental methods that could monitor the CD via fluorescence emission (FDCD for Fluorescence Detected Circular Dichroism) in the case of light harvesting molecules for molecules that need to be excited in the UV, autofluorescence may be used in conjunction with aluminum resonators[7]. Without loss of generality, these considerations lead to the decision of investigating plasmonic resonators with resonance at 680 nm which correspond to the chiral absorption band of LHCII. The idea of blocking the excitation beam to collect only the emission of the chiral molecules leaded to the idea of investigating the resonances of openings in an opaque layer of gold.

1.2 Thesis outline

The manuscript is organized as follow: an Introduction Chapter, three Chapters and one Conclusion Chapter in which I will also present some perspective for this work.

Chapter 2 serves as a comprehensive foundation for our exploration of the world of chirality and its detection. I begin by delving into the essence of chirality in Section 2.1. In Section 2.2, I shift the focus to the detection of chirality using light. Here I discuss polarized light and its characteristics: optical activity, circular dichroism, and optical chirality density. These concepts will be essential tools in my work. Section 2.3 brings into the realm of resonators and chiral media, explaining the critical role they play in harnessing and manipulating light at the nanoscale. This section explores plasmonic resonators, chiral/achiral resonators, and their applications in chiral sensing and spectroscopy. Finally, Section 2.4 introduces the numerical methods, specifically finite-difference time-domain simulation techniques, which is the method I used for modeling and understanding these complex optical interactions.

Chapter 3 presents the study of the localized surface plasmon resonances of nanoslits and the properties of the chirality density inside the open volume of the nanoslits. In Section 3.1, I begin my investigation by exploiting the principle of Babinet and the behavior of achiral plasmonic nanoslits to unravel chiral light phenomena, offering a novel perspective on the generation of chiral fields at the nanoscale. In Section 3.2, I delve deep into the intricacies of the nanoslit's properties. The stage is set here with a comprehensive presentation of the setup parameters for FDTD simulations, from nanoslit structure to mesh accuracy as convergence is key to capture the essence of nanoslit plasmon resonances. In Section 3.3, I further explore the electromagnetic fields of nanoslits. This exploration allows the study of the distributions of electric and magnetic fields in nanoslits for different polarization states of the incident wave. These analyses will contribute to the subsequent analysis of chiral field distributions in nanoslits. Section 3.4 unravels the uniform chirality density exhibited by nanoslits. Here I explore how changes in polarization angle and wavelength can excite and manipulate this chirality density, opening the way to tailored optical responses. Section 3.5 compares nanoslits with their nanorod counterparts. This comparative analysis highlights the special features of nanoslits: unlike nanorods, they exhibit uniform chirality density. Section 3.6 introduces the point-like magnetic dipole model. As I study deeper into this model, it proves to be a powerful tool for accurately reproducing simulation results and providing insight into the uniform chirality density within nanoslits. Finally, in Section 3.7, I investigate the robustness of the chiral field exhibited by nanoslits. Through a careful parametric study, I uncover that nanoslits maintain their optical properties, in particular their uniform chirality, even in the face of shape variations. However, I also recognize the nuanced effects of size and rounded edges on wavelength shifts, underscoring the need for precision in the fabrication process.

Chapter 4 provides a systematic approach to understanding the optical phenomena presented in Chapter 3. Section 4.1 presents an informative overview of multifaceted techniques for characterizing and optimizing nanostructures. These include traditional simulation methods, genetic algorithms, deep learning algorithms, and Jones matrix. In Section 4.2, I discuss a linkage between nearfield and far-field phenomena. Section 4.3 introduce into the behavior of the nanoslit by examining its resonant modes (longitudinal mode and transverse mode). These modes provide significant insights into the optical properties of nanoslits and broaden our understanding of their distinctive characteristics. I develop a hybrid method based on the relation between the excitation in the far-field and the distribution of the electromagnetic nearfield using a generalized Jones matrix formalism. In Section 4.4, a comparison is made between the hybrid method and FDTD simulations. The analysis of the results shows that the hybrid method accurately represents the polarization state and electromagnetic properties of light within nanoslits for any illumination condition. Section 4.5 presents an optimization study where I integrate the insights obtained from preceding sections with conventional optimization algorithms, facilitating the expedient achievement of optimal conditions for maximizing chirality density within nanoslits.

Chapter 2

Concepts and Methods in Chirality

2.1 Introduction to chirality

Chirality is a fundamental concept in chemistry that deals with the asymmetry, or handedness, of molecules and objects. More than a century ago, Lord Kelvin[8] conceptualized chirality, but it would be several decades before the term found its place as a central concept in chemistry textbooks. The term "chiral" comes from the Greek word "kheir," meaning "hand," which aptly reflects the idea that chirality is akin to the distinction between a left hand and a right hand which are mirror images of each other, but they cannot be superimposed. The two mirror images are named enantiomers.

Chiral structures abound in nature at multiple hierarchical levels, ranging from chiral amino acid molecules to the double helix configuration of DNA biomacromolecules, enzyme at nanometer scale, and even observable phenomena such as plant tendrils and galaxies. (Figure 1)

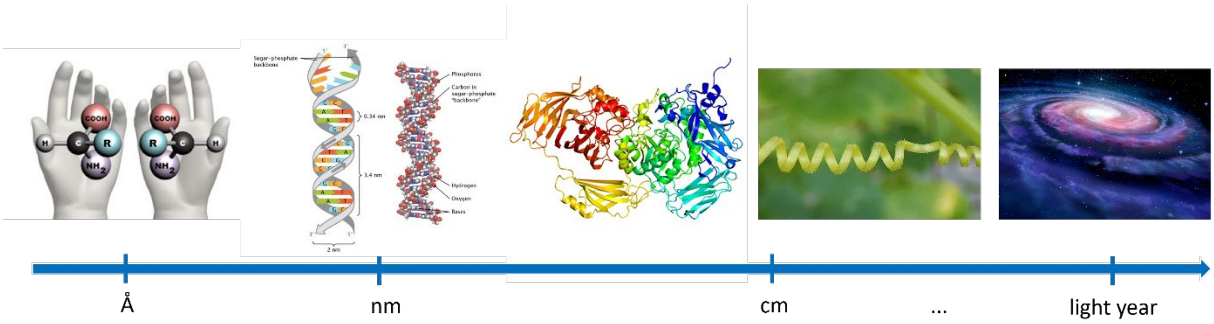

Figure 1 *Chiral architectures in nature at various scales, from enantiomeric molecule at sub-nanometer scale to DNA and enzyme at nanometer scale, further, to living system and galaxy at macroscopic scale.*

In chemistry, many organic molecules are chiral. For example, amino acids, which are the building blocks of proteins, can exist in chiral forms, the L- and D-enantiomers[9]. In the context of life sciences, the majority of amino acids are in the L configuration, with the notable exception of glycine which is achiral. Amino acids in the L-configuration play a crucial role in biological processes, serving as the building blocks of proteins and contributing to various biological functions. Conversely, when sugars are studied in the life sciences, they typically adopt the D configuration, which is important for understanding their biological roles and interactions in living organisms. Another example at a higher structural level concerns temporins which are antibacterial peptids. Their conformation in α-helix is associated with their anti-bacterial activity. [10] Biological structures such as DNA are also chiral[11]. The chirality of

DNA is not just a structural feature, but a fundamental aspect of its biological function. It influences processes such as replication, protein interactions, DNA packaging and repair, and may have played a role in the evolution of life as we know it.

Chirality extends its influence on materials science and nanotechnology. Chiral materials can have unique optical properties that can be exploited in various applications, including sensors [12] and displays [13]. Chiral sensors can be designed to detect specific biomolecules with high selectivity. Cholesteric liquid crystals are chiral materials commonly used in displays such as e-readers and electronic shelf labels. They have the ability to reflect certain wavelengths of light due to their supramolecular chirality. By applying an electric field, the pitch of the chiral structure can be tuned to change the color reflected by the display. This allows the creation of low power, bistable, high contrast reflective displays.

In summary, chirality is a fundamental concept that transcends chemistry and extends its influence into various scientific disciplines, from drug development to materials science to the search for the origin of life. This seemingly simple concept of handedness holds the key to a deeper understanding of the world around us.

2.1.1 Conclusion

In this section I have introduced the knowledge of chirality and enantiomers. Chirality, the property of asymmetry or handedness, was defined as the inability of a molecule or object to be superimposed on its mirror image. The importance of chirality in both chemistry and biology became clear as we delved into its meaning. The role of chirality in drug development, biomolecular interactions, nutrition, and materials science highlighted its multifaceted impact on our understanding of the natural world.

2.2 Detection of chirality using light

2.2.1 Polarized light

The description of the interaction of light with chiral objects can only be understood within the framework of electromagnetics. Light is described as the superposition of an electric field $\boldsymbol{E}$ and a magnetic field $\boldsymbol{B}$ related to one another through the Maxwell's equations:

$$\boldsymbol{\nabla} \wedge \boldsymbol{E} = -\frac{\partial \boldsymbol{B}}{\partial \mathrm{t}} \tag{1)}$$

$$\boldsymbol{\nabla} \wedge \boldsymbol{B} = \mu_0 \boldsymbol{J} + \mu_0 \varepsilon_0 \frac{\partial \boldsymbol{D}}{\partial \mathrm{t}} \tag{2)}$$

$$\boldsymbol{\nabla}.\boldsymbol{E} = \rho/\varepsilon_0 \tag{3)}$$

$$\nabla.\boldsymbol{B} = 0 \tag{4)}$$

In the absence of sources, $\boldsymbol{J}$ and ρ are equal to zero. In linear media, the microscopic charges and currents are taken into account by defining the auxiliary fields $\boldsymbol{D} = \varepsilon_0 \varepsilon_r \boldsymbol{E}$ and $\boldsymbol{H} = \boldsymbol{B}/\mu_0 \mu_r$, where ε_0 and μ_0 are permittivity and permeability of vacuum and ε_r and μ_r are relative permittivity and permeability which capture the response of matter to the electric and magnetic fields. At optical wavelength, μ_r=1.

Without going into detail, it can be shown that any electromagnetic field can be decomposed into an infinite number of monochromatic fields with an angular frequency ω, and each of these can be further decomposed into an infinite number of plane waves with a wave vector $\boldsymbol{k}$. Mathematically, the Fourier integral theory expresses the above relationship:

$$\boldsymbol{E}(\boldsymbol{r}, t) = \int_{\omega} \int_{\boldsymbol{k}} \boldsymbol{E}(\boldsymbol{k}, \omega) e^{-i(\omega t - \boldsymbol{k}.\boldsymbol{r})} d\boldsymbol{k}\, d\omega \tag{5)}$$

To study the polarization of light, we need only consider one elementary component of this decomposition: the monochromatic plane wave, characterized by an angular frequency ω and a wave vector $\boldsymbol{k}$.

In infinite media and in the case of homogeneous plane waves, the Maxwell equation $div\boldsymbol{E} = 0$ imposes the orthogonality of the vectors $\boldsymbol{E}$ and $\boldsymbol{k}$. If *Oz* is the direction of wave propagation, $\boldsymbol{k} = k\hat{\boldsymbol{z}}$, the electric field vector $\boldsymbol{E}$ is expressed in complex notation with a time dependence such as $e^{-i\omega t}$:

$$\boldsymbol{E}(z,t) = \boldsymbol{E_0} e^{-i(\omega t - kz)} \tag{6)}$$

with $k = nk_0 = n\frac{\omega}{c}$, where $n = \sqrt{\varepsilon_r}$ is the refractive index seen by the wave in the direction of propagation. *c* is the speed of light. $\boldsymbol{E_0}$ is a complex vector, located in the wave plane, which characterizes the polarization state. In the orthonormal Cartesian frame *Oxy* of unit vectors $\hat{\boldsymbol{x}}$ and $\hat{\boldsymbol{y}}$, we have:

$$\boldsymbol{E_0} = A_x e^{\mathrm{i}\phi_x} \hat{\boldsymbol{x}} + A_y e^{\mathrm{i}\phi_y} \hat{\boldsymbol{y}} \tag{7)}$$

In this decomposition, A_x and A_y are positive real constants and the phases ϕ_x and ϕ_y are also defined within 2π. In a plane wave of equation 6), the real cartesian components of vector $\boldsymbol{E}(z,t)$ can be written as:

$$\boldsymbol{E_x}(z,t) = A_x \cos(\omega t - kz - \phi_x) \tag{8)}$$

$$\boldsymbol{E_y}(z,t) = A_y \cos(\omega t - kz - \phi_y) \tag{9)}$$

The time evolution of the vector $\boldsymbol{E}(z,t)$ describes the polarization state of the optical wave under consideration. This state is fully characterized by the complex vector $\boldsymbol{E_0}$.

If we associate a point N with the extremity of the vector $\boldsymbol{E}(z,t)$, this point generally describes an ellipse located in the wave plane. This is an ellipse composed of two oscillations of the same frequency, with different amplitudes and phases. Since the state of polarization is, by definition, related to the time evolution of the electric field vector, the most general state of polarization of a monochromatic plane wave in a homogeneous medium is an elliptic state of polarization.

If $\phi = \phi_y - \phi_x$ is the phase shift between the orthogonal oscillations $\boldsymbol{E_x}(t)$ and $\boldsymbol{E_y}(t)$, the general expression for elliptical polarization is:

$$\boldsymbol{E_x}(t) = A_x \cos(\omega t) \tag{10)}$$

$$\boldsymbol{E_y}(t) = A_y \cos(\omega t - \phi) \tag{11)}$$

The direction of rotation of the current point N on the ellipse naturally depends on the sign of the phase angle ϕ.

In addition, there are two special polarization states that will be present: linear polarization and circular polarization. Linear polarization refers to a state of polarization in which the electric field vector of an electromagnetic wave oscillates in a single, fixed direction as the wave propagates through space. Circularly polarized light is characterized by a constant magnitude of the electric field, but with its direction continuously changing in a circular motion. There are two forms of circular polarization: right-handed (clockwise rotation) and left-handed (counterclockwise rotation). Circular polarization occurs when the phase difference between the horizontal and vertical components is ±π/2 (-90 degrees or 90 degrees):

$$\boldsymbol{E_x}(t) = A_x \cos(\omega t) \tag{12)}$$

$$\boldsymbol{E_y}(t) = \pm A_y \sin(\omega t) \tag{13)}$$

For convenience in describing a polarization state, we usually give parameters of an elliptic polarization state. Figure 2 shows the various parameters used to characterize the polarization state. In linear media, only the relative amplitudes of Equations 12) and 13) are useful and the polarization state can fully describe using angles.

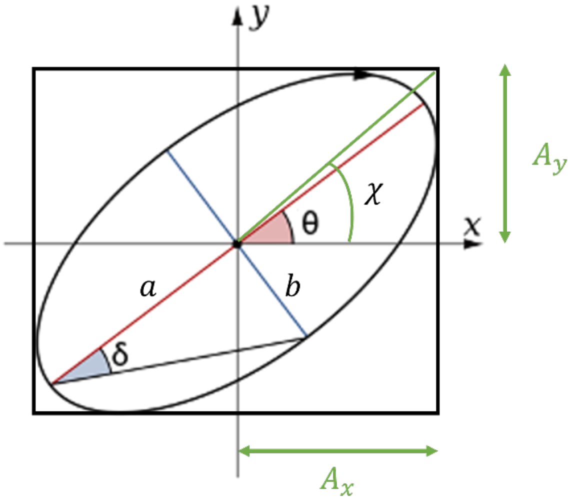

Figure 2 *parameters of an elliptical polarization state*

The angles θ and δ characterize the orientation and ellipticity of the ellipse. The polarization angle θ represents the orientation or tilt of the ellipse with respect to a reference axis, usually the horizontal axis (x-axis). The angle δ characterizes the ellipticity of the polarization state. When δ is $\pm\pi/4$, the ellipse is a perfect circle. When $\delta = -\pi/4$, left-handed circular polarization is formed. When $\delta = \pi/4$, right-handed circular polarization is formed. The tilt angle χ is defined by the ratio of A_y to A_x. The relations among these quantities are:

$$\tan 2\theta = \frac{2A_xA_y}{A_x^2 - A_y^2}\cos\phi \qquad 14)$$

$$\tan\delta = \frac{b}{a} \qquad 15)$$

$$\tan\chi = \frac{A_y}{A_x} \qquad 16)$$

2.2.2 Jones vector

R. Clark Jones[14] introduced in 1941 a formalism for describing the propagation of polarized light through anisotropic crystals. I will introduce this formalism here and will use it to express the polarization of light in Chapter 4. The Jones vector is a two-component column vector that represents the amplitude and phase of an electric field. In the Cartesian frame *Oxy*, according to Eq. 7), the general form of the Jones vector is:

$$\boldsymbol{V} = \begin{bmatrix} A_xe^{i\phi_x} \\ A_ye^{i\phi_y} \end{bmatrix} \qquad 17)$$

In general, a state of elliptical polarization can be represented by a normalized Jones vector dependent on two parameters: the tilt angle χ defined in Figure 2 and the phase difference ϕ, as follows:

$$\boldsymbol{V}(\chi,\phi) = \begin{bmatrix} \cos\chi \\ \sin\chi e^{i\phi} \end{bmatrix} \qquad 18)$$

It is useful to represent any elliptical state using the polarization angle θ and the ellipticity δ. In the proper frame of the ellipse, the Jones vector is written as follows:

$$\boldsymbol{V} = \begin{bmatrix} \cos\theta\cos\delta - i\sin\theta\sin\delta \\ \sin\theta\cos\delta + \mathrm{i}\cos\theta\sin\delta \end{bmatrix} \tag{19)}$$

The typical Jones vectors for linearly polarized light with a polarization angle θ, and the Jones vector can be represented as:

$$\boldsymbol{V} = \begin{bmatrix} \cos\theta \\ \sin\theta \end{bmatrix} \tag{20)}$$

For circular polarization, Equations 12) and 13) can be presented as the Jones vector:

$$\boldsymbol{V} = \frac{1}{\sqrt{2}}\begin{bmatrix} 1 \\ \mathrm{i}\cdot\mathrm{sign}(\delta) \end{bmatrix} \tag{21)}$$

2.2.3 Jones matrix

The Jones matrix is a fundamental concept in polarization optics used to describe the behavior of light as it passes through an optical element, such as a polarizer, a retarder, or a waveplate. It provides a mathematical representation of how the polarization state of light changes when it interacts with these elements.

Let us consider an optical element that transforms the incoming Jones vector $\begin{bmatrix} E_{inc,x} \\ E_{inc,y} \end{bmatrix}$, decomposed on x and y polarizations basis, into an outgoing Jones vector $\begin{bmatrix} E_{out,x} \\ E_{out,y} \end{bmatrix}$. This transformation can be represented by a 2×2 matrix called the Jones matrix J defined as follows:

$$J = \begin{bmatrix} J_{xx} & J_{xy} \\ J_{yx} & J_{yy} \end{bmatrix} \tag{22)}$$

Each element of the Jones matrix (J_{xx}, J_{xy}, J_{yx} and J_{yy}) represents the complex amplitude change and phase shift experienced by the corresponding polarization component as it passes through the optical element. The relation between the outgoing and incoming Jones vector is:

$$\begin{bmatrix} E_{out,x} \\ E_{out,y} \end{bmatrix} = J\begin{bmatrix} E_{inc,x} \\ E_{inc,y} \end{bmatrix} \tag{23)}$$

This transformation can be used to describe the effect of any optical element on the polarization state of light.

In the next part I will discuss the interaction of matter with circularly polarized light. With that aim, it is convenient to express the Jones matrix in the circular polarization basis where the unit Jones vectors [1 0] and [0 1] actually represent right-circular polarization and left-circular polarization, respectively. For propagation along z in a medium of polarization dependent refractive index $\tilde{n}^{\pm} = (n^{\pm} + ik^{\pm})$ on the path of length l, J can be written:

$$J = \begin{bmatrix} e^{ik^{+}l} & 0 \\ 0 & e^{ik^{-}l} \end{bmatrix} = \begin{bmatrix} e^{i\frac{2\pi}{\lambda}(n^{+}+ik^{+})l} & 0 \\ 0 & e^{i\frac{2\pi}{\lambda}(n^{-}+ik^{-})l} \end{bmatrix} = e^{i\frac{2\pi}{\lambda}n^{-}l} \begin{bmatrix} e^{i\frac{2\pi}{\lambda}(n^{+}-n^{-})l} e^{-\frac{2\pi}{\lambda}k^{+}l} & 0 \\ 0 & e^{-\frac{2\pi}{\lambda}k^{-}l} \end{bmatrix} \tag*{24)}$$

$$J = e^{i\frac{2\pi}{\lambda}n^{-}l} \begin{bmatrix} e^{i\alpha l} e^{-\frac{2\pi}{\lambda}k^{+}l} & 0 \\ 0 & e^{-\frac{2\pi}{\lambda}k^{-}l} \end{bmatrix} \tag*{25)}$$

Where $\alpha = \frac{2\pi}{\lambda}(n^{+} - n^{-}) = \frac{2\pi}{\lambda}\Delta n$.

2.2.4 Chirality and optical activity

The history of optical activity begins in the early 19th century, at a time when scientists were beginning to unravel the wavelike nature of light. In 1811, French physicist François Jean Dominique Arago[15,16] observed that some substances could rotate the plane of polarized light as it passed through them. However, it was not until 1815 that the French physicist Jean-Baptiste Biot[17,18] made significant progress in understanding this puzzling behavior. Biot's investigations into the polarization of light led to the discovery that certain substances possess the remarkable ability to rotate the plane of polarized light. This peculiar property, first observed in naturally occurring substances such as quartz crystals and sugar solutions, marked the birth of optical activity as a distinct scientific field. The following decades witnessed a flurry of activity as scientists sought to understand the underlying principles of optical activity. Augustin-Jean Fresnel's[19] wave theory of light and Jean-Baptiste Biot's collaboration with Félix Savart[20] furthered the understanding of optical rotation. It was the pioneering work of French chemists Louis Pasteur[21,22] and Jean-Bernard-Léon Foucault in the mid-19th century that established the link between molecular asymmetry and optical activity in their studies of tartaric acid, a compound found in grape juice.

Optical Rotatory Dispersion (ORD) is a fundamental spectroscopic technique that plays a central role in the elucidation of the structural and chiral properties of organic molecules.[23] First introduced in the early 20th century, ORD measures the spectroscopic dependence of the rotation axis experienced by linearly polarized light as it passes through an optically active (chiral) substance. Linearly polarized light can be represented as a combination of left circularly polarized (LCP) and right circularly polarized (RCP) light, each of equal amplitude. Initially, before the linearly polarized light enters the chiral medium, there is no rotation in the orientation of the plane of polarization of the light. (Figure 3) When exposed to chiral substances, LCP and RCP light exhibit different refractive behavior.

In a transparent material (Pasteur experiments), the absorption coefficient for any polarization state is zero which simplifies the Jones matrix of Equation 25) with $k^{\pm} = 0$. If the incident polarization is linear, its expression in the RCP/LCP basis is $\boldsymbol{V^L} = \frac{1}{\sqrt{2}}\begin{bmatrix}1\\1\end{bmatrix}$. According to Equation 25) the transmitted Jones vector is $\frac{e^{i\frac{2\pi}{\lambda}n^{-}l}}{\sqrt{2}}\begin{bmatrix}e^{i\alpha l}\\1\end{bmatrix}$, which is a linear polarization rotated by α/2. The angle α is an intrinsic property of a chiral chemical compound, called specific rotation.[24]

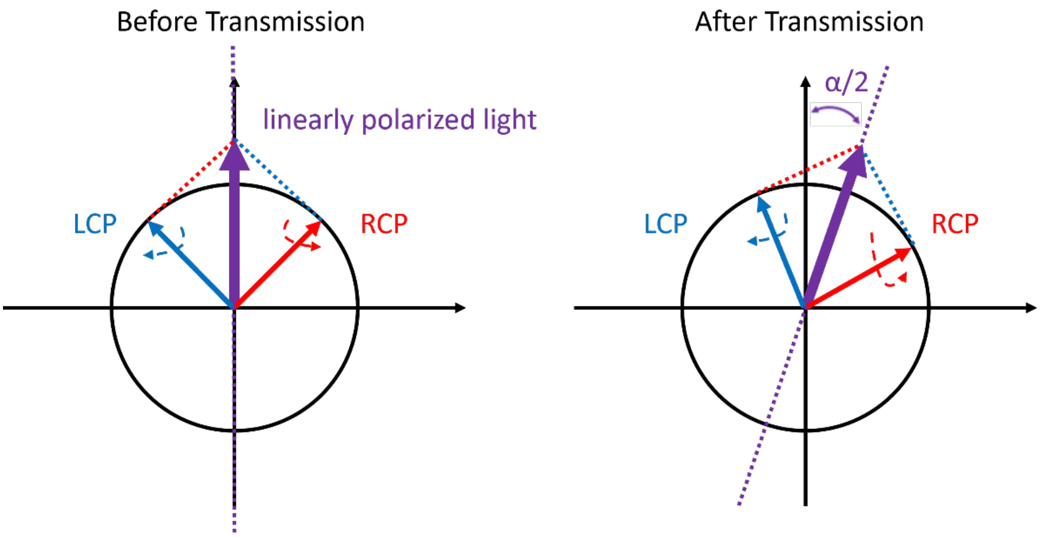

Figure 3 *Schematics of ORD. The purple arrows represent linearly polarized light, the blue and red arrows represent left- and right-handed circularly polarized light, respectively, and α/2 is the angle of rotation after the polarized light has propagated through the chiral medium.*

Values for specific rotation α are reported in units of deg·mL·g^{-1}·dm^{-1}, which are often shortened to degrees, where in the other components of the unit are tacitly assumed. [25] If the wavelength of the light used is 589 nanometers (the sodium D line), the symbol "D" is used. The sign of the rotation (+ or −) is always given. Some common compound examples are given here (Table 1):

Table 1 The measured specific rotation α for different compounds

Compound name	α_D^{20} (deg·mL·g^{-1}·dm^{-1})	Δn
(S)-2-Bromobutane	+23.1	$7.6\ 10^{-5}$
(R)-2-Bromobutane	-23.1	$-7.6\ 10^{-5}$
D-Sucrose[26]	+66.37	$2.2\ 10^{-4}$
D-Lactose[26]	+52.3	$1.7\ 10^{-4}$
Taxol A[27]	-49	$-1.6\ 10^{-4}$

The sign of α indicates the direction in which the compound rotates plane-polarized light, with a positive value indicating clockwise rotation (dextrorotary) and a negative value indicating counterclockwise rotation (levorotary). The Δn values presented in Table 1 are very small, as a result, the actual angular rotation of plane-polarized light caused by a low molecule concentration can be extremely small, making it difficult to measure accurately without specialized equipment and careful experimental techniques. For single molecules, direct detection of their specific rotation α would be extremely challenging due to the minuscule angular changes involved.

2.2.5 Circular Dichroism (CD)

Like ORD, CD spectroscopy uses circularly polarized light, but it evaluates the difference in absorption[23] of left- and right-handed circularly polarized light by a chiral sample over a range of wavelengths (Figure 4). This difference in absorption, known as the circular dichroism signal, provides insight into the secondary and tertiary structure of molecules, making CD a powerful tool for studying protein folding, DNA conformation, and molecular chirality.[28,29]

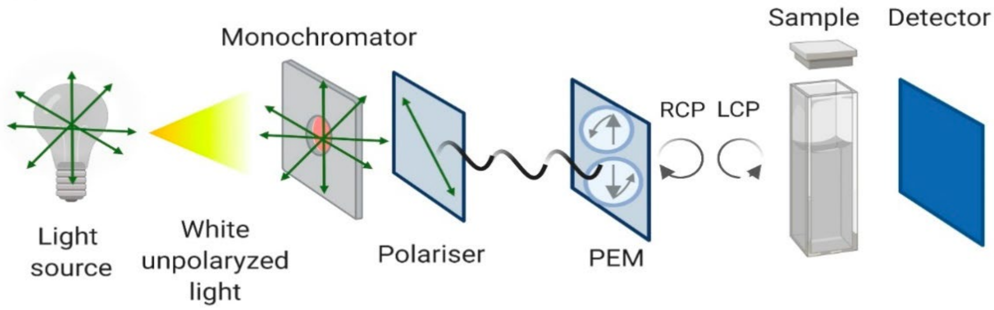

Figure 4 *Schematic representation of the Circular Dichroism instrument configuration.*[30]

In 2.2.2 and 2.2.3, we discussed the Jones vector and matrix, so we have the transmitted intensity is A=***V****. ***V***. For incident right-handed circular polarization, the transmitted Jones vector is $V^+ = e^{i\frac{2\pi}{\lambda}n^- l}\begin{bmatrix} e^{i\alpha l}e^{-\frac{2\pi}{\lambda}k^+ l} \\ 0 \end{bmatrix}$;and for left-handed circular polarization, the transmitted Jones vector is $V^- = e^{i\frac{2\pi}{\lambda}n^- l}\begin{bmatrix} 0 \\ e^{-\frac{2\pi}{\lambda}k^- l} \end{bmatrix}$. We obtain then:

$$A^{\pm} = \left(e^{-\frac{4\pi}{\lambda}k^{\pm} l}\right) \tag*{26)}$$

Consequently, the $\mathrm{CD} = 2\frac{A^+ - A^-}{A^+ + A^-}$, depends only on the extinction coefficients for LCP and RCP of the material. However, the CD is generally reported in terms of ellipticity in millidegrees (δ).

In biological research, it is important to remember that for most, if not all, the observed CD signals are extremely small. It is common to observe ellipticities of about 10 millidegrees (mdeg). This means that the difference in absorbance between the two circularly polarized components is approximately 3×10^{-4} absorbance units[31]. In addition, the different types of regular secondary structure found in proteins give rise to characteristic deep-UV CD spectra (Figure 5).

The low values of the optical rotation and circular dichroism, associated with the small differences between the optical constants of most molecules for right and left circular polarizations hints towards the need of exacerbating the interaction between light and matter if one wants to reduce the quantity of matter needed to produce a detectable signal on small quantity of matter.

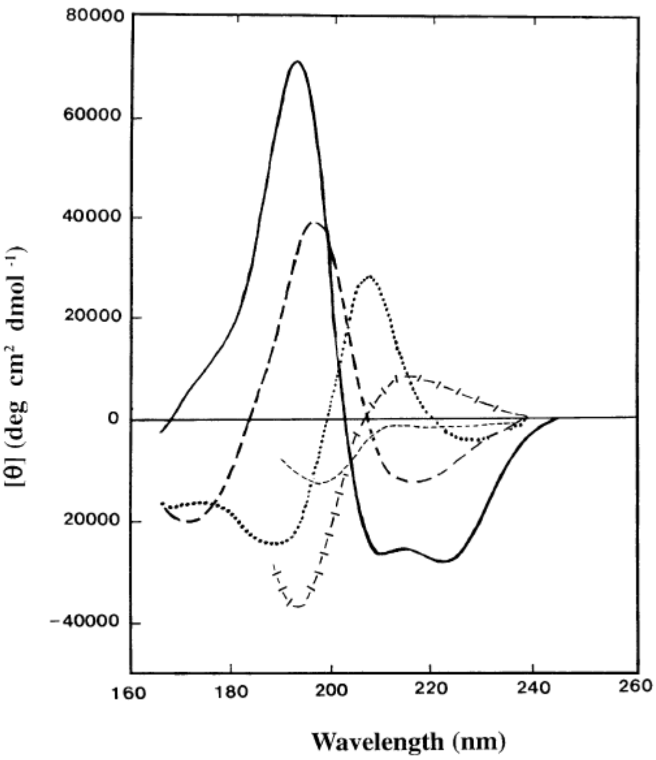

Figure 5 *Far UV CD spectra associated with various types of secondary structure. Solid line, α-helix; long dashed line, anti-parallel β-sheet; dotted line, type I β-turn; cross dashed line, extended 3_1-helix or poly (Pro) II helix; short dashed line, irregular structure.*[31]

2.2.6 Chirality density

Optical rotation dispersion and circular dichroism measure the chiral effects in the interaction of the optical field with the sample. However, it is of both fundamental and practical interest to introduce a measure of the chirality of the optical field itself. Tang and Cohen[32] introduced the local measure of the chirality of a nonparaxial monochromatic field. To emphasize its local nature, this is referred to here as optical "chirality density". The chirality density C was first introduced by Lipkin[33]:

$$C \equiv \frac{\varepsilon_0}{2}\boldsymbol{E}\cdot\nabla\times\boldsymbol{E}+\frac{1}{2\mu_0}\boldsymbol{B}\cdot\nabla\times\boldsymbol{B} \qquad 27)$$

The time average of C is generally also noted C and is equal to:

$$< C >_t \equiv C = -\frac{\varepsilon_0\omega}{2}Im(\widetilde{\boldsymbol{E}}^*\cdot\widetilde{\boldsymbol{B}}) \qquad 28)$$

For a monochromatic plane wave, the relationship between chirality density and ellipticity is: [34]

$$C \simeq \frac{W}{\omega}\delta \tag{29)}$$

Where W is the energy density of the light beam and ω is the angular frequency. This remarkably simple result would suggest that increasing the chirality density of light could be achieved by simply increasing the flux of photons or the ellipticity. However, we will see that in the evanescent fields, the relation is less simple.

In a chiral field, the field lines wind around a central axis while also having a component that is parallel to this axis. The quantity C, is the embodiment of this geometric picture. Subsequently, Tang and Cohen[32] demonstrated that C determines the degree of asymmetry in the excitation rate of a small chiral molecule by circularly polarized light. A chiral molecule exposed to the monochromatic EM field generates an electric dipole moment $\widetilde{\boldsymbol{p}}$ and magnetic dipole moment $\widetilde{\boldsymbol{m}}$, which are given from:

$$\widetilde{\boldsymbol{p}} = \tilde{\alpha}\widetilde{\boldsymbol{E}} - i\tilde{G}\widetilde{\boldsymbol{B}} \tag{30)}$$

$$\widetilde{\boldsymbol{m}} = \tilde{\chi}\widetilde{\boldsymbol{B}} + i\tilde{G}\widetilde{\boldsymbol{E}} \tag{31)}$$

$\tilde{\alpha}$, $\tilde{\chi}$ and $\tilde{G}$ are frequency–dependent complex scalars, i.e., $\tilde{\alpha} = \alpha'(\omega) + i\alpha''(\omega)$. They denote the electric, magnetic, and magneto-electric coupling polarizabilities, respectively.

By combining Eq. 30) and 31) with the rate of excitation of the molecule:

$$A^{\pm} = \langle \boldsymbol{E} \cdot \dot{\boldsymbol{p}} + \boldsymbol{B} \cdot \dot{\boldsymbol{m}} \rangle \tag{32)}$$

Tang and Cohen have shown that the absorption by chiral materials for RCP (+) and LCP (−) polarized light, A$^{\pm}$, was[32]:

$$A^{\pm} = \frac{\omega}{2}\left(\alpha''\left|\widetilde{\boldsymbol{E}}\right|^2 + \chi''\left|\widetilde{\boldsymbol{B}}\right|^2\right) \pm G''\omega Im\left(\widetilde{\boldsymbol{E}}^* \cdot \widetilde{\boldsymbol{B}}\right) \tag{33)}$$

We can see that the difference between A^+ and A^- contains two components: one associated with the chiral molecule through the imaginary part of its magneto-electric polarizability (G'') and one associated with the chirality of the light through the term $\omega(Im(\widetilde{\boldsymbol{E}}^{*} \cdot \widetilde{\boldsymbol{B}}))$ where we recognize the time-averaged chirality density of Eq. 28). Since the properties of the molecules are fixed, maximizing the chirality density will maximize the CD.

Cohen have proposed the concept of "superchiral" (SC) fields that show chiral asymmetries hundreds of times larger than the asymmetries of circularly polarized light (Figure 6) in small regions of space [35]. The key is to set up an imperfect standing wave consisting of two counter-propagating CPL plane waves with slightly different amplitudes. An enhancement of the chiral asymmetry is predicted at the nodes of the standing wave. Near the superchiral nodes, the ratio of optical chirality (C) to electric energy density (U_e) is larger than in the incident light. In this plot, the ratio of the left- and right-field amplitudes is 2:1. In the experiment, the ratio was 1.17:1.[35]

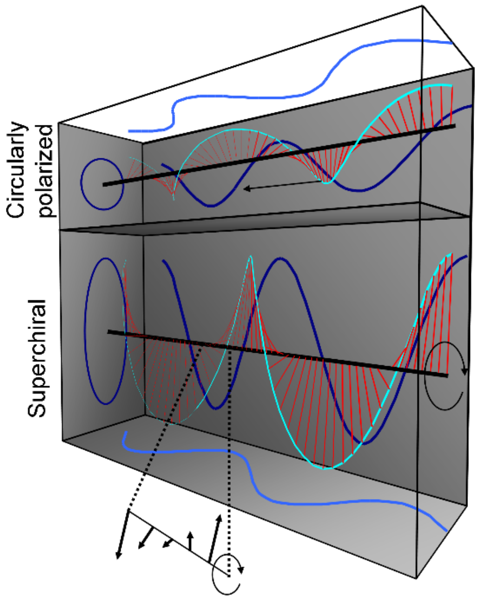

Figure 6 *Electric field in LCP light (top) and SC light (bottom). In LCP light, the field has uniform optical chirality and energy density throughout space. Also plotted are projections of the field onto the xy, xz, and yz planes at a single point in time (dark blue). The arrows indicate the direction of propagation of the field. In SC light, the field line rotates about its axis but does not propagate. At any instant, the projection of the field along the propagation axis is an ellipse, but over time the field at each point traces out a circle.*

I will discuss in the following other solutions proposed to generate superchiral fields. However, it must be noted, that superchiral fields will be superchiral only due to the enhancement of the electromagnetic fields with respect to the incident field as can be inferred from Eq. 29), the ellipticity will always remain bounded between -1 and 1.[36]

2.2.7 Conclusion

In this part, I have started with the basics of polarized light, exploring the concepts of the Jones vector and Jones matrix as essential tools for characterizing the properties of light. Building on this foundation, I then delve into the fascinating realm of optical activity and circular dichroism, highlighting their crucial role in chirality detection. Finally, I introduce the concept of optical chirality density, providing a comprehensive framework for understanding and quantifying chirality in the context of light interactions.

2.3 Resonators and chiral media

2.3.1 Optical resonators

Optical antennas are nanoscale structures designed to manipulate and enhance the interaction of light with matter. These tiny devices play a pivotal role in the field of optics by enabling precise control of light at the nanoscale. They are critical in applications such as nanophotonics, where they improve the efficiency of light-emitting devices and sensors. Optical antennas are also instrumental in the development of advanced imaging techniques, enabling super-resolution imaging and single-molecule detection. Optical antennas play a key role in plasmonics by focusing and amplifying electromagnetic fields at the nanoscale, enabling the manipulation of light-matter interactions. This capability is fundamental to plasmonics for applications ranging from high-resolution imaging to efficient energy harvesting and advanced sensing technologies.

2.3.2 Plasmonic

Plasmonics describes the interaction between light and free electrons within a metal, resulting in the creation of oscillating electron density waves known as plasmons. These plasmons can effectively enhance light-matter interactions.

Localized Surface Plasmon Resonance (LSPR) enables a precise manipulation of electromagnetic fields at the nanoscale, resulting in highly sensitive and tunable sensors.[37] Their role in concentrating electromagnetic energy at specific locations on metallic surfaces enhances the detection capabilities, making them invaluable tools for applications such as biosensing and environmental monitoring. For the case of localized surface plasmons, light interacts with particles much smaller than the incident wavelength (Figure 7a). This leads to a plasmon that oscillates inside the nanoparticle at a given frequency known as the LSPR with a strong nearfield enhancement (Figure 7b).

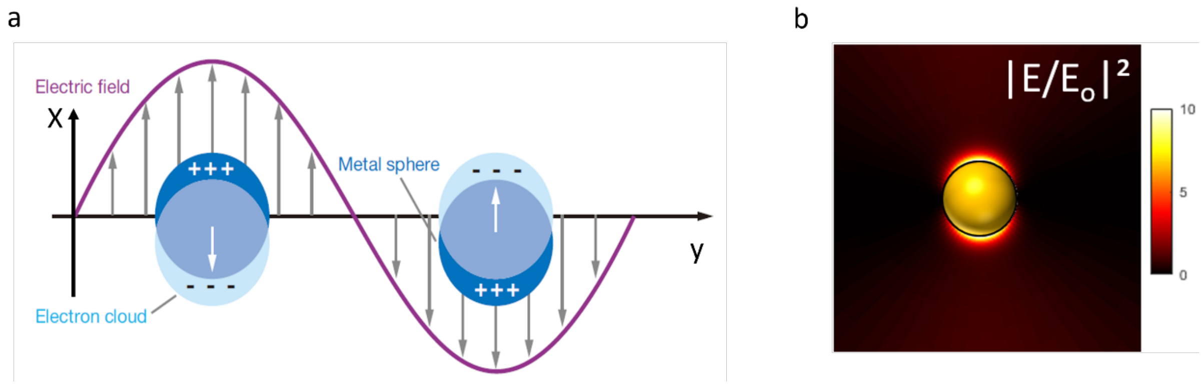

Figure 7 ***a)*** *Schematic diagrams illustrating a localized surface plasmon.*[37] ***b)*** *repartition of the electric field intensity around a 5nm diameter gold nanoparticle in air at the LSPR. The black line delineates the contour of the nanoparticle.*

These resonances, which are intricately linked to the specific geometry and material composition of the nanostructures, [38] lead to the formation of exceptionally sharp spectral absorption and scattering peaks. One way to describe the spectral dependence of the interaction of light with a metallic nanoparticle which dimensions are smaller than the mean free path of the electrons is by writing the motion (Figure 7) of the electrons:

$$m_e\frac{\partial^2 x}{\partial t^2} = -\gamma\frac{\partial x}{\partial t} - kx - qEe^{i\omega t} \qquad 34)$$

Where m_e is the mass of the electron, γ is a damping factor due to the scattering of the electrons by the surface or defects, k is the restoring force introduced by the surface limiting the movement of the electrons and q is the charge of the electrons. The solutions of x sought for are supposed to be harmonic solutions in time so that the amplitude of x have a Lorentz line shape centered in ω_o with a broadening of γ:

$$x = -\left(\frac{1}{\omega_0^2 - \omega^2 - i\gamma\omega}\right)\frac{q}{m}E_o \qquad 35)$$

Where $\omega_0^2 = k/m_e$.The polarizability of the nanoparticle is $\boldsymbol{P} = -Nqx$, with N the density of electrons, and the electric displacement is $\boldsymbol{D} = \varepsilon_0\boldsymbol{E} + \boldsymbol{P} = \varepsilon_0\varepsilon_r\boldsymbol{E}$. Inserting Eq. 35) yields the spectral dependence of the relative permittivity ε_r of a small plasmonic nanoparticle:

$$\varepsilon_r = n^2 = \left(1 + \frac{\omega_p^2}{\omega_0^2 - \omega^2 - i\gamma\omega}\right) \qquad 36)$$

Where $\omega_p^2 = \frac{Nq^2}{m\varepsilon_0}$ is the plasma frequency which for gold is in the UV part of the spectrum at approximately 137 nm. The frequency ω_0 of the LSPR of a sphere in a medium of permittivity ε_0 is related to the plasma frequency by $\omega_0 = {}^{\omega_p}/_{\sqrt{3}}$.[39] In air, a metallic nanoparticle with such plasma frequency should have a LSPR at 237 nm. However, due to the presence of interband transitions, which modify the resonant behavior of electrons in the nanoparticles, the LSPR of a small gold nanoparticle in air is near 510 nm.

2.3.3 Chiral resonators with chiral media

Owing to the strong nearfield intensity generated, LSPR have been used in sensing applications, mostly to detect the presence of specific biomolecules.[40,41] Building on this expertise and having in mind the need of detecting the small signal of ORD and CD (see Sections 2.2.4 and 2.2.5), there has been a strong effort in the scientific community with the aim of introducing chirality sensitive detection based on plasmonics and superchiral fields. The published works can be separated in two categories as I will illustrate in this Section. The maybe first logical type of resonators are chiral resonators.

Kadodwala[42] introduces superchiral polarimetry as a novel spectroscopic technique capable of rapidly detecting minute ligand-induced conformational changes in higher-order protein structures at the picogram level. (Figure 8) The experiment involved measuring ΔΔλ of two enantiomeric plasmonic chiral metasurfaces coupled to ligand solutions containing chiral molecules. The concept of ΔΔλ is that in the presence of a dielectric environment the LSPR of a chiral resonator is redshifted by Δλ. If the dielectric environment is chiral, the LSPR of a right-handed metasurface will be shifted by $\Delta\lambda_R$ while that of a left-handed metasurface will be shifted by $\Delta\lambda_L$. If the LSPR is sensitive to the chirality of the environment $\Delta\lambda_R \neq \Delta\lambda_L$ which is characterized by $\Delta\Delta\lambda = \Delta\lambda_R - \Delta\lambda_L$. In Ref 42, the chiral materials used were specifically shikimic acid, ADP, shikimate-3-phosphate, and glyphosate for Shikimate kinase (SK) and 5-enolpyruvylshikimate 3-phosphate synthase (EPSPS) proteins. The ligands, even in the absence of proteins, exhibited small ΔΔλ values of opposite sign due to their inherent chirality, reflecting their limited interaction with the electromagnetic fields, while proteins inheriting chirality from their constituent amino acids exhibited strong ΔΔλ values as large as 16 nm for some proteins.[2] Unlike traditional chiral methods such as CD spectroscopy, superchiral polarimetry exploits enhanced chirality within evanescent fields to achieve remarkable sensitivity to mesoscale chiral structures. This technology offers the potential for label-free biophysical measurements and, with specially designed cells, can be applied to nanoliter quantities of ligand solutions. In addition, the micron-scale nanopatterned surface (Shuriken) required for analysis allows unprecedented multiplexing capabilities, making it a promising tool for applications such as high-throughput drug screening.

The chiral resonators used in Kadodwala's study were fabricated using e-beam lithography and had slender arms that intentionally reduce its fineness. As a result, achieving precise reproducibility for these resonators proves challenging. These design choices, such as the slim arms, affect the fineness of the resonator and the reproducibility of the experimental setup. This is a strong limitation, as part of the ORD or CD measured on the bare resonators may be affected by linear dichroism and birefringence induced signals associated with residual asymmetries resulting from fabrication imperfections.[43, 44]

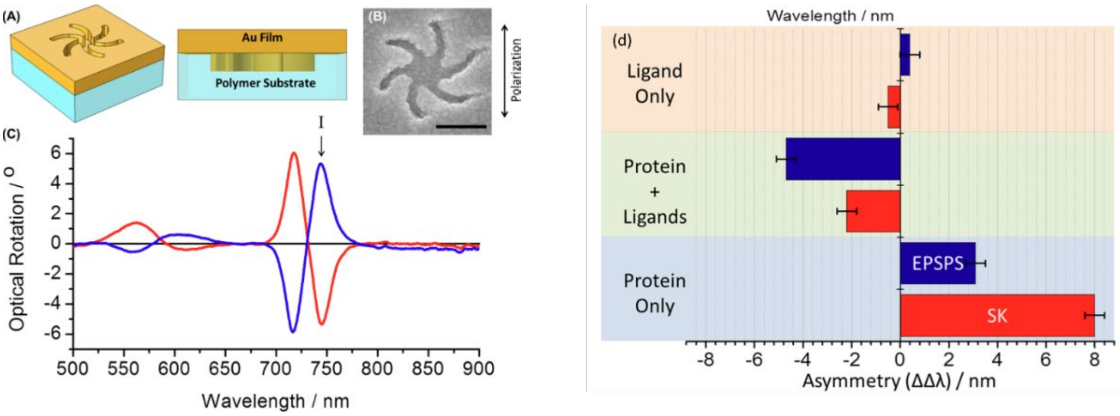

***Figure 8** Taken from ref [42] **a)** Graphical description of a single LH nanostructure in the TPS. **b)** SEM of a Shuriken nanostructure from a LH TPS (scale bar shows 250 nm). **c)** ORD spectra for LH (red) and RH (blue) TPS. **d)** ΔΔλ values for the data obtained from the ORD spectra.*

Chiral resonators have also been investigated in the group of R. Quidant[45] .Chiral gold nanostructures (Gammadion) with zero intrinsic circular dichroism (CD) but chirality density and electric field enhancement were studied. (Figure 9) This was achieved by creating a 'racemic' surface containing both right- and left-handed gammadions. In this work, chiral gold nanostructures were coated with a 150nm thin layer of molecular enantiomers of D-, L-phenylalanine or a racemic mixture of D- and L-phenylalanine. While the metasurface exhibited nearly no CD, the presence of L- (D-)phenylalanine induced positive (negative) CD near the plasmon resonance of the metasurface. A racemic mixture of L- and D-phenylalanine deposited on the metasurface showed no CD. This innovative approach demonstrated that plasmonic sensors can provide chiral selectivity without inherent macroscopic CD, a significant advancement in chiral detection technology. Because of the fabrication process, the chiral layer was a 150 nm thick dense layer.

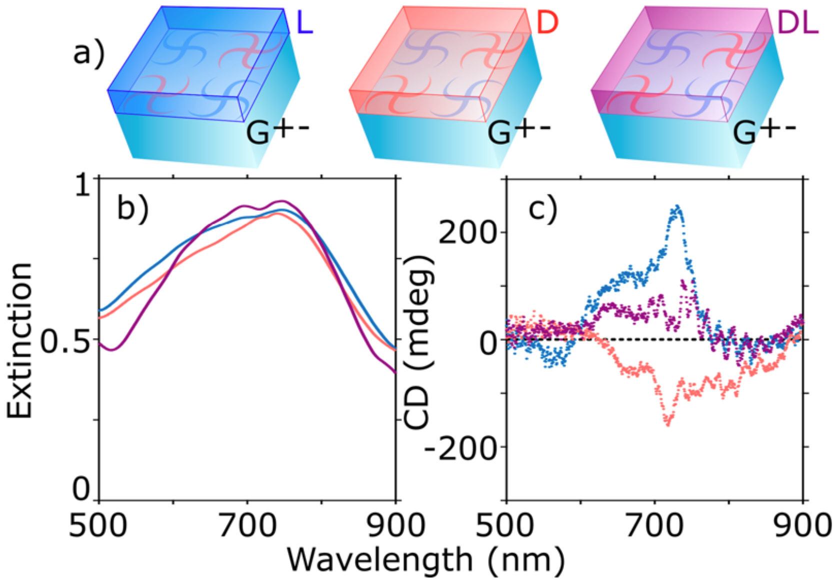

Figure 9 *Taken from ref [45] Enantiomer detection in the visible spectral range using racemic gammadion arrays.* ***a)*** *The molecules were deposited on different sensor arrays, showing the corresponding* ***b)*** *extinction and* ***c)*** *CD spectrum.*

Quidant's group extended their study with achiral dielectric resonators made of silicon cylinder arrays.[46]. (Figure 10) Although achiral, these simple dielectric resonators support electric and magnetic modes which overlap spectrally with presumably magneto-electric coupling in the overlap region. The experiment involved measuring the induced CD for different molecular enantiomers, specifically L-, D-, and a racemic mixture of the amino acid phenylalanine. These sensors exhibited enantiomeric sensitive CD enhancements in the VIS-NIR range near the resonance of the Si disks. However, the study found that the spectral position of the electric dipole (ED) and magnetic dipole (MD) resonances did not significantly affect the CD enhancement, with the ED contribution being the dominant factor.

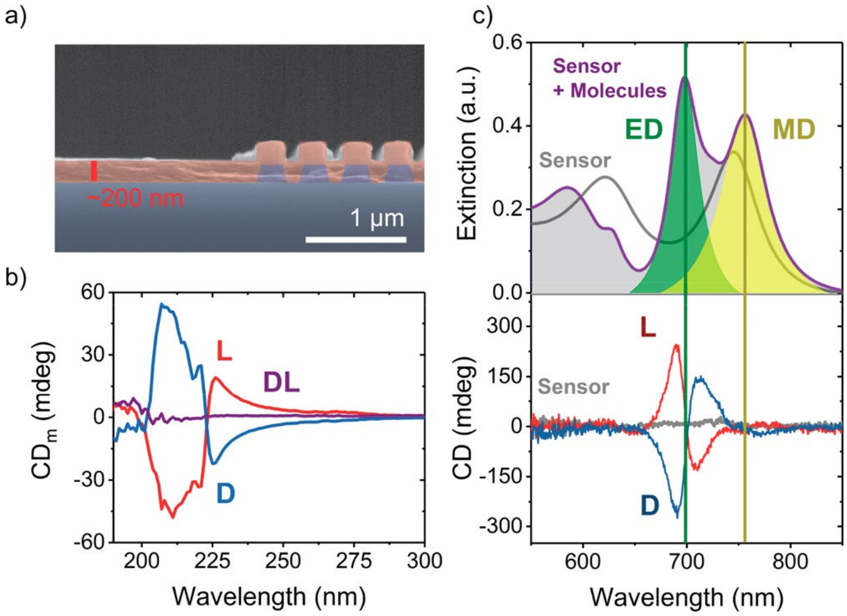

Figure 10 *Taken from Ref [46]* ***a)*** *Scanning electron micrograph of the transverse section of Si sensors (purple colored) coated with a ~200 nm thick phenylalanine coating (red-colored).* ***b)*** *Experimental molecular UVCD (label as* CD_m*) for L-, D-, and DL- (racemic mixture) coatings of phenylalanine on quartz (without sensors), in red, blue, and purple, respectively.* ***c)*** *Experimental extinction (top) and CD (bottom) spectra of the bare and coated sensors for a 120 × 120* μm^2 *cylinder array with 130 nm height, 160 nm diameter, and 420 nm period. The gray lines correspond to extinction and CD of the bare sensor before the molecular coating. The purple lines correspond to the extinction of the coated sensors. The green and yellow shaded areas indicate the position of ED and MD resonances, respectively. The red and blue curves in the CD plot correspond to the L- and D-enantiomers of phenylalanine coatings on sensors. The green and yellow vertical lines across the plots indicate the position of the ED and MD, respectively.*

2.3.4 Achiral resonators with chiral media

Achiral plasmonic, resonators have been investigated. Achiral plasmonic structures, such as gold nanoparticles, nanodisks, and nanorods, do not exhibit CD when interacting with circularly polarized light: any measured CD is then presumably attributed to the presence of a chiral environment.

Govorov[47] explored the manipulation of ellipticity in nanomaterials in solution using chiral peptides adsorbed on non-chiral gold nanoparticles (Figure 11a). The interaction between these biomolecules and nanoparticles generated optical activity as confirmed by circular dichroism spectroscopy, with a distinct signal observed at the plasmon resonance frequency at approximately 520 nm.

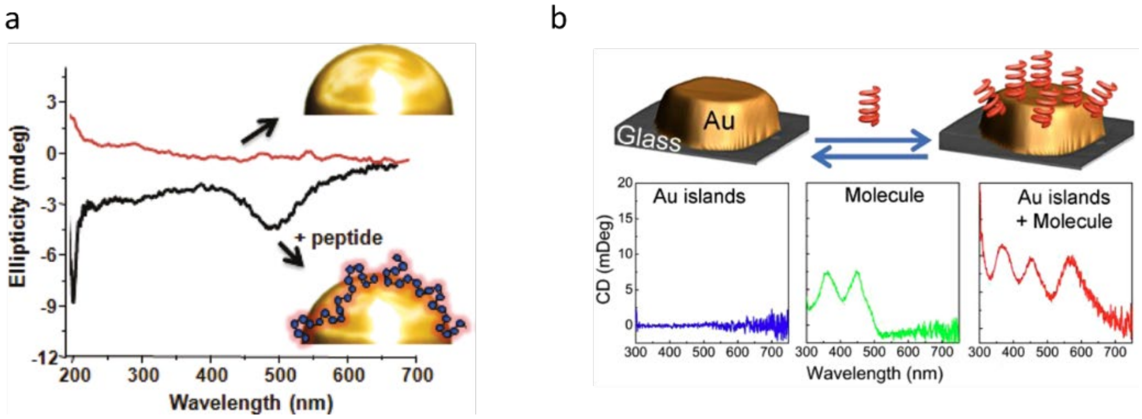

***Figure 11** Taken from Ref [47] **a)** Optical characterization of gold nanoparticles functionalized with the FlgA3 peptide (8.6 µM) with 1.14×10^{13} particles/mL. CD spectra of UV region. **b)** taken from Ref [48] A scheme of the experiment, bare gold islands (lateral dimensions: 75 nm × 64 nm, average height ~20 nm) are covered with a 19 nm thick PMMA film which includes embedded riboflavin molecules. CD spectra of the Au nanodisk, molecule only and nanodisk with molecule.*

In a similar study, Markovich[48] explored the same phenomenon of CD induced by chiral molecules in the vicinity of gold nanostructures (nanodisk), in contact with chiral molecules embedded in PMMA. (Figure 11b) His study showed that even the minimal presence of two monolayers of chiral molecules could induce measurable CD at the plasmonic resonance, while these molecules alone would not exhibit such properties. Importantly, the plasmonic substrates used in this research offer several advantages, including tunable surface plasmon bands spanning the visible to near-infrared region, reproducibility, cost-effectiveness, and robust stability against various environmental conditions. Consequently, this innovative approach represents a promising avenue for broad-spectrum molecular chirality sensing with potential applications in identifying the organic origin of test materials. The mechanism at the origin of transfer of chirality observed in these studies is still not perfectly clear. It should be noticed that the CD enhancement was large because it was compared to the zero-signal observed for the bare resonators, however the values remained in the mdeg range.

The effects observed experimentally were also investigated numerically[49] (Figure 12). In Ref. 49, the study focuses on the electromagnetic interactions between a homogeneous chiral medium and plasmonic structures (nanorod) using the software COMSOL. The chiral medium was described by using bi-isotropic constitutive relations. The orientation of the incident circular polarization with resonantly enhanced field vectors in plasmonic hot spots is shown to be crucial, leading to a significant enhancement of the plasmon resonance by 3 orders of magnitude, although the CD signal remains small. These findings were in line with the experimental results described above.[47] It was also shown that achiral plasmonic gap antennas outperformed their chiral counterparts, such as Born-Kuhn-type [50] plasmonic dimers, in enhancing CD signals.

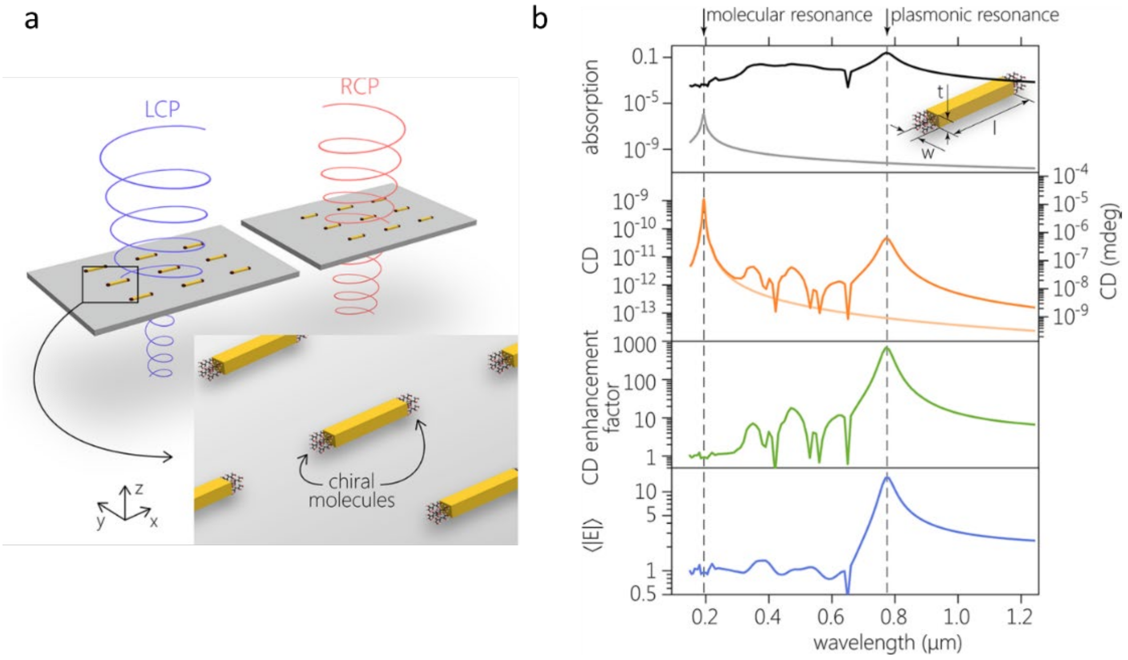

***Figure 12** taken from Ref [49] **a)** Schematic of plasmon-enhanced circular dichroism (PECD) detection scheme. The inset shows the chiral material patches that are placed at the hot-spots of the plasmonic antennas. **b)** Optical responses of chiral medium patches located at the hot-spots of a plasmonic rod antenna array. Paler lines indicate the chiral response of the patches without antennas. (Black solid line) Absorption for linearly polarized normal incidence. (Orange solid line) Circular dichroism signal (absolute values). The scale on the right marks CD values as ellipticity in millidegrees. (Green solid line) Enhancement factor of the CD signal. (Blue solid line) Averaged electric field enhancement within the volume occupied by the chiral patches.*

The same group has extended this study while developing a modal theory.[51] This theory elucidates the intricate mechanisms underlying nanophotonic chiral sensing, including chirality-induced resonance shifts and changes in the excitation and emission efficiencies of resonator modes. Surprisingly, resonance shifts are often not the dominant source of signals, especially in achiral sensors where they are strictly zero to the first order. Instead, changes in excitation and emission efficiencies emerge as the primary driving force for improving circular dichroism spectroscopy. Even in the case of symmetric nanostructures (nanorod) exposed to linearly polarized light optical chirality can be observed as seen in Figure 13: it results from the superposition of the radiated fields and the incident fields.[52]

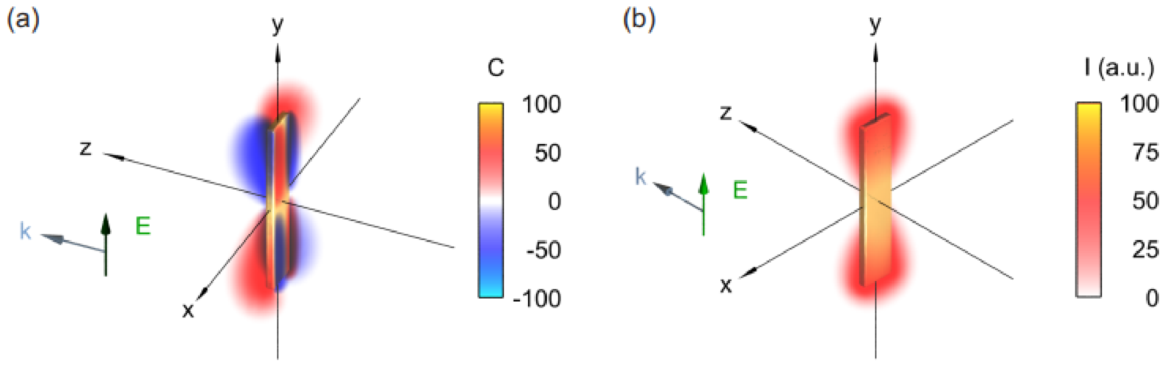

Figure 13 *Taken from Ref [52]* ***a)*** *Optical chirality induced by a linear plasmonic nanoantenna illuminated with light polarized parallel to the antenna axis under normal incidence at resonance (217 THz). The values have been normalized by the optical chirality of circularly polarized light.* ***b)*** *The fundamental antenna mode exhibits strongest intensity of the electric field at the ends of the rod. The distribution differs significantly from the regions with strongest optical chirality.*

However, the nanorod's chiral field exhibits simultaneous regions of opposite sign, resulting in a cancelling effect that significantly reduces the overall nanorod's chiral field. This intriguing finding highlights the need for a more comprehensive understanding of the complex interactions within the chiral nearfield, potentially opening avenues for further investigation and refinement of chiral field manipulation techniques.

2.3.5 Point like dipole model

In analyzing the chiral field of the nanorod above, it can be observed that the mechanism for polarization control of the localized optical field generated by a single gold nanorod, as demonstrated by Giessen[52], involves calculating the chirality density spatial distribution for illumination with light linearly polarized. The calculation is based on a simple model in which the longitudinal plasmon excited in the nanorod is approximated as an oscillating electric dipole ***p*** and the chirality density is obtained by adding the incident field to the field radiated by the electric dipole (Figure 14).

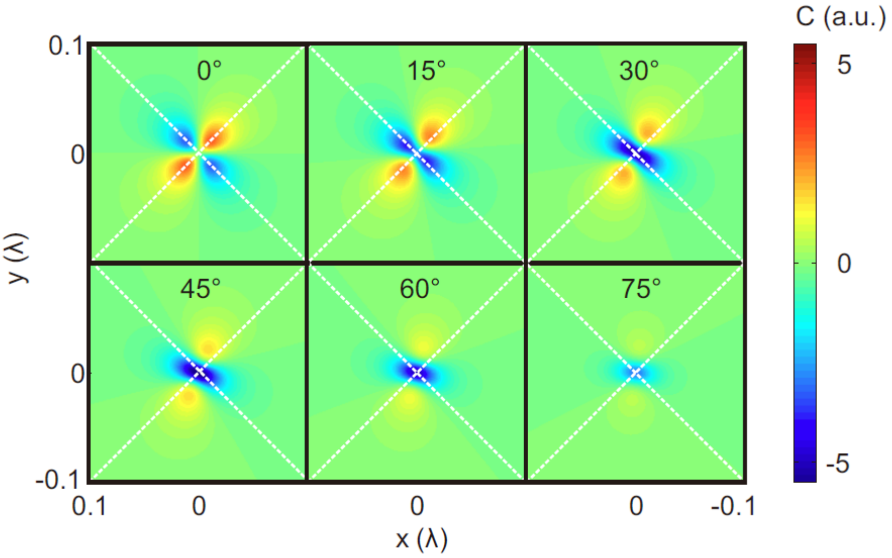

Figure 14 *taken from Re [52] Optical chirality of a Hertzian dipole illuminated with linearly polarized light at a distance of z = 0.02λ behind the dipole. The distribution changes with increasing polarization angle. The white dashed lines are guides to the eye to see the rotation of the initial lobes of optical chirality.*

This simple model was used by Okamoto[53] to describe in an experimental study where the excitation was obtained in the nearfield with a polarization maintaining SNOM tip. (Figure 15) The chirality of the nearfield was determined by measuring the ellipticity of the light radiated into the far-field for incident linear excitation. The pattern found agreed very well with the ones expected with the model assuming that the local field resulted from the superposition of the incident field and the field radiated by an electric dipole.

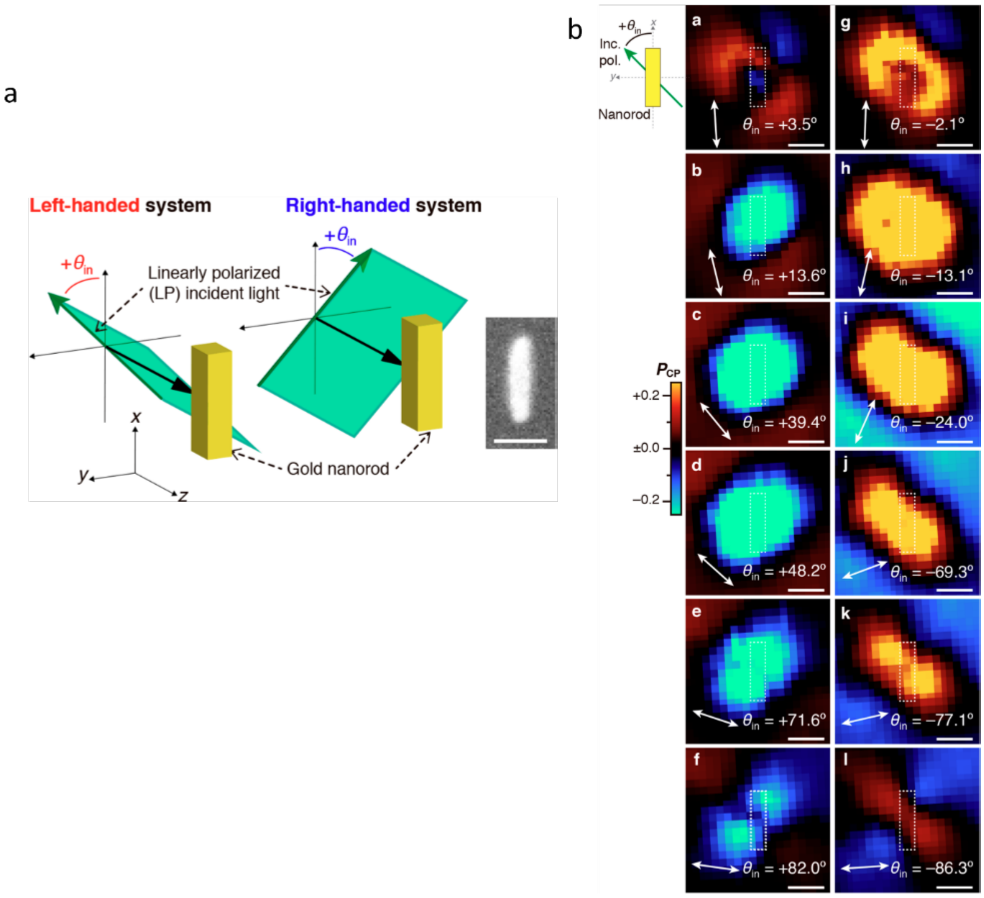

Figure 15 *Taken from Ref [53]* ***a)*** *Strategy for introducing symmetry breaking in the system and active control of the local chiral optical field by adjusting the azimuth angle (θ_{in}) of the incident linearly polarized field relative to the axis of the nanorod, Inset: Scanning electron micrograph of a gold nanorod (160 nm × 40 nm × 55 nm) used in this study. Scale bar: 100 nm.* ***b)*** *Experimentally observed maps for the degree of circular polarization of the optical fields (PCP) near a single gold nanorod.*

2.3.6 Conclusion

In summary, optical resonators play a key role in harnessing and manipulating light at the nanoscale, enabling a wide range of applications in photonics and nano-photonics. Plasmonic resonators use surface plasmon resonances to focus electromagnetic fields and enhance light-matter interactions. Chiral resonators, when coupled with chiral media, exhibit unique circular dichroism properties that are invaluable in chiral sensing and spectroscopy. In addition, achiral resonators in chiral environments allow tuning of optical properties by chirality, opening new avenues for versatile optical devices. Finally, the point-like dipole model has been used as a fundamental framework for understanding the behavior of these resonators, providing valuable insights for their design and optimization in various optical applications.

2.4 Numerical methods

2.4.1 Introduction of FDTD

The Finite-Difference-Time-Domain (FDTD) method is a powerful numerical technique widely used in the field of electromagnetic simulations. It allows accurate modeling and analysis complex optical resonator systems by discretizing both space and time. FDTD has gained popularity for its ability to solve Maxwell's equations in a straightforward and versatile manner, making it an indispensable tool for studying the behavior of light in various optical structures. The accuracy of the results is partly related to a proper definition of the cell containing the nanostructure (size, boundary conditions), of the definition of the excitation and of the mesh size. These parameters are also related to the wavelength domain sought for. In this work I have used the software Lumerical FDTD by ANSYS. I will provide a basic description of the calculation configuration I have used while explaining the reasons of the choices made.

2.4.2 Unit cell

The calculations were performed in a cubic unit cell as shown in Figure 16. I was interested mostly in the nearfield of isolated nanostructures which has implied some choices and constraints in the design parameters of the unit cell.

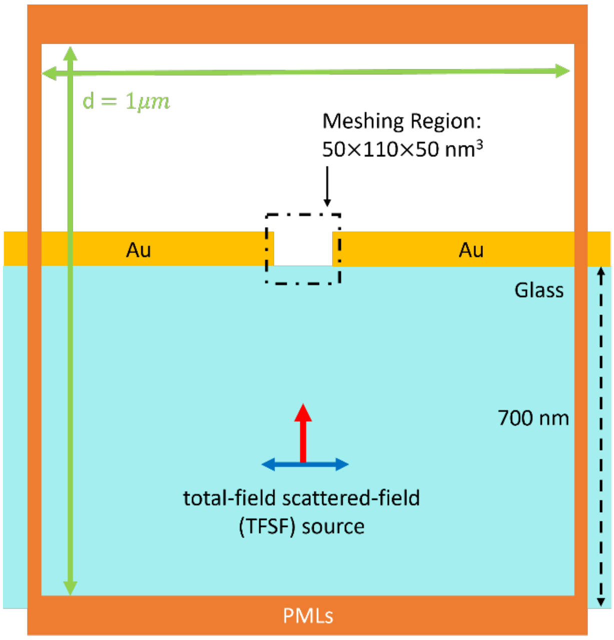

Figure 16 *Schematic diagram of FDTD simulation unit cell*

1. Boundary Conditions:

   - The whole computational window was surrounded by a Perfectly Matching Layers (PMLs) to avoid unwanted reflections.

The PMLs is a common absorbing boundary condition. PMLs are used to prevent unwanted reflections at the simulation boundaries. Without PMLs, reflections from the boundaries could interfere with the results and distort the behavior of the nano resonator. The PMLs allow describing single objects and semi-infinite media.

2. Simulation Domain:

   - Calculation window size: 1 micrometer in all three spatial dimensions.

The size of the simulation domain should be large enough to encompass several wavelengths of the electromagnetic waves being simulated. This is important to ensure that boundary effects do not significantly affect the results. Besides, the simulation region should be large enough to accommodate the placement of sources and structures of interest and make sure that the objects are far enough away from the boundaries to exhaust the nearfield. On the other hand, the simulation domain should be as small as possible to limit the computation time. A 1-micrometer domain minimization ensured that there was enough space to enclose the nanoslit and study its propagation and scattering without boundary effects affecting the simulation results.

   - The gold film is placed on a semi-infinite glass substrate.

The use of a "semi-infinite" glass substrate in the simulation is a common approximation to mimic realistic experimental setups in which light does not undergo reflection at the back of the substrate. This was effectively ensured by the PML boundary at the bottom of the simulation cell. While this simplification is practical and computationally efficient, it is important to recognize that no substrate is truly infinite in reality.

3. Optical Constants:

   - Optical constants were taken from the Lumerical database and correspond to the usual values for gold thin film [Johnson & Christy] and fused silica.

Accurate optical constants are essential for realistic simulation results. Gold has complex wavelength-dependent refractive indices and absorption coefficients and glass although transparent is dispersive too. Lumerical database contains the optical constants of these materials to accurately capture these properties.

4. Excitation Source:

- The source was a linearly or circularly polarized plane wave.

The choice between linear and circular polarization allows studying how different polarization states of the incident light interact with the nano resonator. By using linear polarization, it is possible to study how the orientation of the incident electric field with respect to the geometry of the nanoslit affects its response.

The polarization of the incident light for linear polarization is set by changing the polarization angle directly in the general menu of the total-field scattered-field (TFSF) source (see subsection 2.4.3), while the setting of the incident light for circular polarization is generated by adding two orthogonal linear polarizations with a phase difference of 90 degrees. The left- and right-handed are determined by the order of the phase difference.

The excitation source positioned at -350 nm from the nano resonator, exciting the nanostructure from the substrate side. This positioning allows precise targeting of the nanoslit from one side of the substrate, which is a typical configuration in experiments. A distance of 350nm is chosen to ensure that the distance is within the calculation window size, while ensuring that the incident light interacts effectively with the nanoslit.

- The source was a short pulse with a duration of 2.66 fs.

The use of a short pulse allows the study of ultrafast optical phenomena and the precise capture of rapid nano resonator interactions, which is particularly important when studying plasmon resonances and transient optical effects. I will go into more detail in the next subsection (2.4.4). However, in this work, the decision to use a short pulse of 2.66 fs duration, followed by Fourier analysis was driven by the need to broaden the spectrum and center it at 700 nm with a spectral width of 600 nm. This large spectral range allowed a comprehensive study of the response of the resonator in different wavelengths, facilitating the identification of resonant modes and spectral features.

5. Data Collection:

    - The electric and magnetic optical fields were then collected in a volume of 50×110×50 nm^3 enclosing the nano resonator by 1 nm mesh step.

The specific dimensions here refer to the actual dimensions of the nanoslit that I have studied. The specific dimensions of the nanoslit will be given in Chapter 3, its electric and magnetic field analysis, and later the calculation of the chirality density throughout the nanoslit for all wavelengths contained in the optical pulse will also be shown in Chapter 3. The mesh will cover the entire calculation window, but we set the mesh region to cover the area we want to focus on, so mesh=1nm was used for this region.

2.4.3 External sources

The total-field scattered-field (TFSF) source is a technique commonly used in numerical simulations, particularly finite-difference time-domain (FDTD) and finite-element method (FEM) simulations, to separate incident and scattered fields for analysis. The TFSF source is used to inject a finite span plane wave into a computational region. Its primary purpose is to separate the incident and scattered fields within the region. The computational region is divided into two parts: inside the source region, both incident and scattered fields are present, while outside the source region, only the scattered fields are considered. The TFSF source subtracts all light directly transmitted through the source region or reflected from a flat substrate at its boundaries. This ensures that only scattered light from features inside the source region propagates to the outside. When a substrate is present, the TFSF source uses an edge as a reference and calculates the fields that would be directly reflected or transmitted by the reference refractive index profile. This information is subtracted at the boundaries. The injection power of the source depends on the size of the plane wave it injects. To obtain meaningful results, normalization by source intensity (in units of cross section) is often used instead of the standard method. There are specific rules for setting up TFSF sources, such as ensuring that the source does not extend into PMLs boundaries, and that the source injection axis is perpendicular to the substrate.

Overall, TFSF sources are a valuable tool for computational electromagnetics, allowing the study of the behavior of electromagnetic waves in structures and materials.

2.4.4 The electromagnetic spectrum

To simulate a wide spectral range, start with a broadband pulse source. This pulse source typically has a defined temporal shape (e.g., Gaussian or other waveform) and is centered at a specific frequency (or wavelength). After performing a broadband pulsed FDTD simulation, the electromagnetic field data are collected over time in the simulation domain. The time domain field data is then Fourier transformed to obtain the corresponding frequency domain or spectral information. The Fourier transform essentially decomposes the time-domain signal into its constituent frequency components, providing amplitude and phase information for each frequency component. Repeat this procedure for various center wavelengths or frequencies of interest. For each iteration, select a different center wavelength and adjust the characteristics of the broadband pulse source accordingly. While the excitation source is a pulse, the simulation is often run for a sufficient time until the pulse has passed through the domain and no longer interacts significantly with the structures. This allows to observe the stationary or steady-state response of the structures to the excitation.

To account for the dispersion of optical constants, the complex refractive index of the materials in simulation (e.g., gold and glass) is often provided in a database as a function of wavelength. During simulation, the software interpolates or directly uses the appropriate optical constants corresponding to the current wavelength/frequency of the pulse. This accounts for dispersion and accurately models how the refractive index of the material changes with wavelength.

2.4.5 Conclusions

In this section, we have covered the basics of FDTD simulation techniques. Subsection 2 explored various critical components, such as the simulation domain, optical constants, excitation source, boundary conditions, and data acquisition methods. In addition, subsections 3 and 4 introduced two essential sources: the broadband pulse source and the TFSF source.

Chapter 3

Electromagnetic Field and Chiral Field in Nanoslits

3.1 Introduction

In the study of nanorod in Section 2.3.4, we have seen that a chiral field can be formed by combining an achiral structure with an achiral incident field. However, we can still see that in the case of a nanorod, the chiral field always has both left- and right-hand properties[54], and they cancel each other out in the unit cell around the nanorod, resulting in the reduction of the total chiral field.

Here, we theoretically and numerically propose to generate a pure and nanoscale hot spot of chiral light in the nearfield by using a single achiral plasmonic nanoresonator based on a rectangular nanoslit[55,56,57] behaving as a magnetic dipole (Figure 17b) in accordance with the Babinet principle[63,58,59,60].

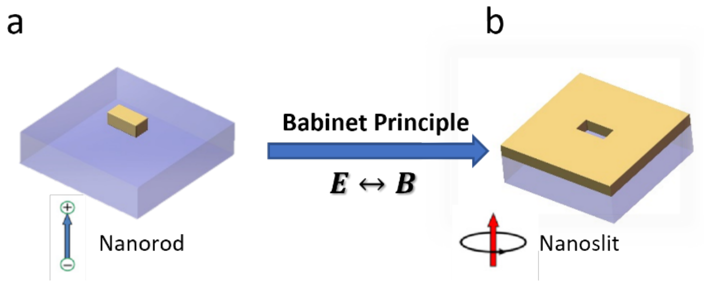

Figure 17 *Schematic representation of the structure of* ***a)*** *nanorod and* ***b)*** *nanoslit. nanorod is a rectangular body on a glass medium. Equivalent to an electric dipole, nanoslit is a rectangular slit, also on a glass medium, equivalent to a magnetic dipole. They are related by the Babinet Principle.*

The illustration of this principle can be seen in the field maps of the electric and magnetic field enhancements in the plane of observation, where the electric and magnetic fields are plotted at resonance for a nanoslit and a nanorod for excitation polarized along or perpendicular to the long edge of the resonator (Figure 18). We see, in good agreement with Babinet's principle, although I did not use an infinitely thin perfect conductor, that the distribution of the electric and magnetic fields are opposite with respect to an electric dipole antenna such as a plasmonic nanorod[59,60]. In particular, the E-field is concentrated homogeneously in the center of the nanoslit while the B-field is maximum at the edges.

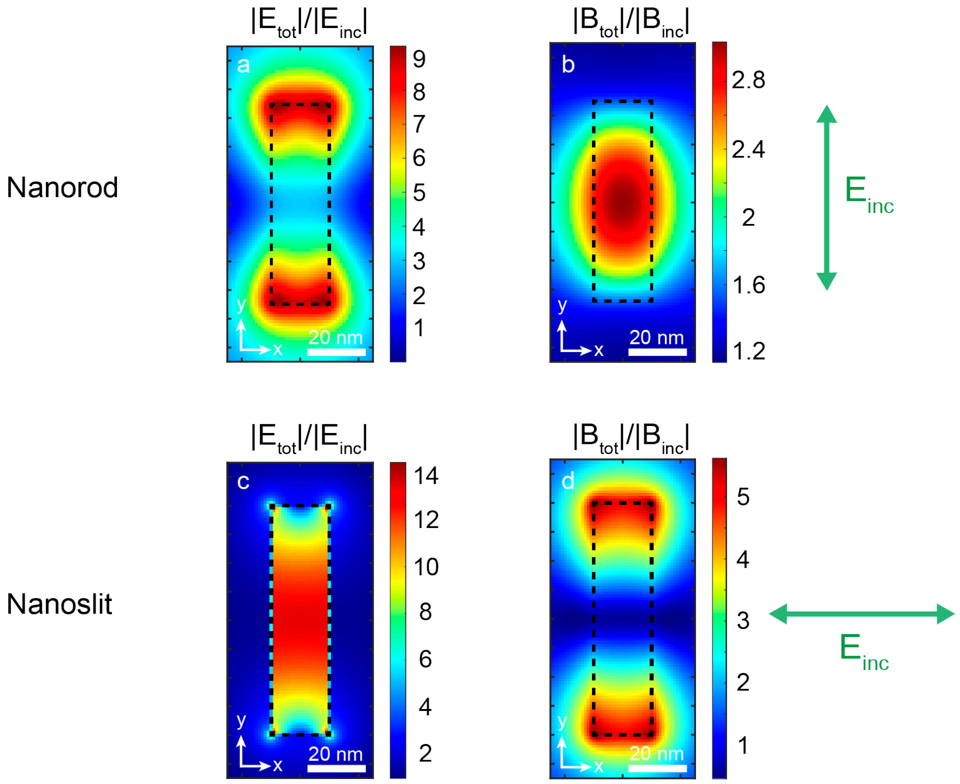

Figure 18 *Electromagnetic field distribution in the plane of observation of a nanoslit and a nanorod. Spatial distribution of* ***a)*** *electric and* ***b)*** *magnetic fields in an XY plane 5nm above nanorod in Z, at lambda=680 nm, and for a polarization angle θ = 90°. Spatial distribution of* ***c)*** *electric and* ***d)*** *magnetic fields in an XY plane at the center of the nanoslit in Z, at lambda=680 nm, and for a polarization angle θ = 0°.*

In this Chapter, I will be particularly interested in describing the behavior of the nanoslit. The idea is that the excitation wavelength may go through the liquid containing the chiral molecules (Figure 19). In the case of an experiment that would be based on Fluorescence-Detected Circular Dichoism (FDCD), no contribution would be expected from the molecules in the liquid in the path of the linearly polarized excitation light and any measured dichroic signal would originate only from the interaction region defined by the volume of the nanoslit. I will explain in this Chapter why and how all the FDCD signal would only originate from the interaction volume contained in the nanoslit.

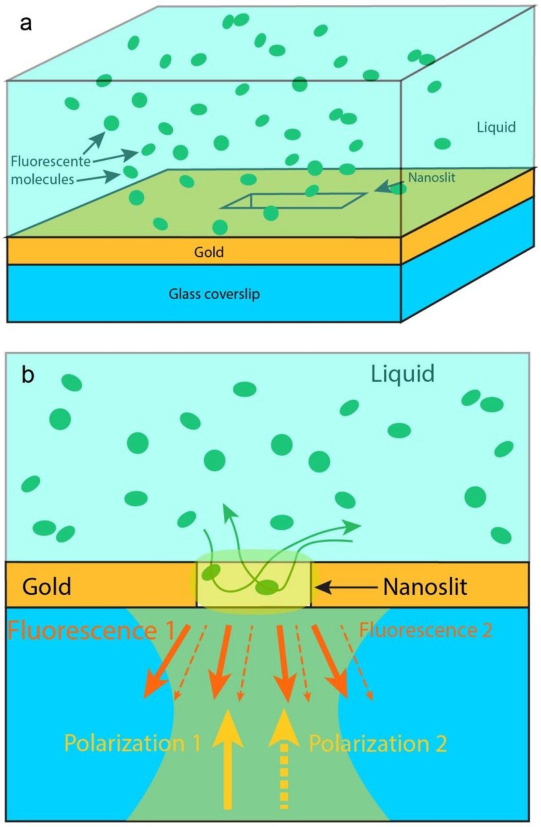

Figure 19 *Principle of a Fluorescence-Detected Circular Dichroism (FDCD) experiment in the vicinity of a plasmonic nanoslit. Chiral molecules in solution are placed on the sample containing the nanoslits. Next, optical excitation is made from the substrate side to excite the nanoslits with different polarizations, creating different chirality densities. As a result, chiral molecules in solution can freely flow inside the nanoslits. The photons emitted during this interaction are then collected from the same side as the excitation so that only the fluorescence of the molecules inside the nanoslit is collected, not the reflection. This fluorescence is then used to measure the FDCD by estimating the difference in emitted fluorescence for both polarizations before normalizing this signal with respect to the sum of fluorescence intensities. This normalization procedure means that the sensitivity of the fluorescence signal to the quantum yield of the molecule and to the collection efficiency of the experimental setup cancels out, meaning that the FDCD signal is directly proportional to the change in excitation efficiency, namely the chirality density C. Plasmonic nanoholes in gold films have already been exploited for the detection of single molecules in solution thanks to their fluorescence signal.*

3.2 Simulation of nanoslit

3.2.1 Simulation parameters

As I described at the end of Chapter 2, the simulations were performed with the FDTD commercial software Lumerical. All simulation parameter settings are summarized there. The rectangular nanoslit used in this study is schematically represented in Figure 20a. It is made in a thin gold layer of thickness H=40 nm deposited on a glass substrate. The width W of the nanoslit is fixed at 20 nm and its length L varies from 50 to 90 nm in steps of 10 nm. The excitation is performed from the glass substrate by a linearly polarized plane wave, with a polarization angle θ, and propagates along the positive Z axis (Figure 20a). θ was chosen with respect to the short axis of the nanoslit, light polarized at θ = 0° being along the X axis of the nanoslit (Figure 20b). We mainly observe the distribution of electromagnetic fields in a plane within the rectangular nanoslit (XY plane when Z=20 nm) and for two points, point A is the geometric center (0,0) of the nanoslit and point B is 5 nm away from the short edge and on the y axis. These two points correspond to the positions of the maximum electric and magnetic fields in the nanoslit, respectively (Figure 18).

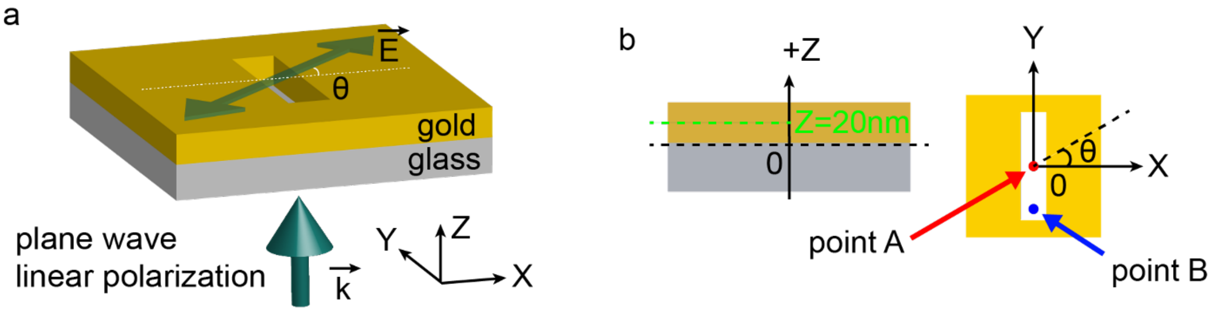

Figure 20 *Schematic representations of the magnetic dipolar nanoslit.* ***a)*** *3D and* ***b)*** *2D representation of the rectangular nanoslit in a thin gold layer of 40 nm. The vector* ***k*** *represents the direction of propagation of the linearly polarized incident plane wave, and θ, the angle of this polarization with respect to the nanoslit's transverse axis (Ox).*

3.3 Electromagnetic field of nanoslit

3.3.1 Spectral responses of the nanoslit for different dimension

Figure 21 shows the spectral responses of the nanoslit for different lengths L. These spectra represent the enhancement of the electric (Figure 21a) and magnetic (Figure 21c) fields normalized to the incident wave, in the center (point A) and side (point B) of the nanoslit, 20 nm above the glass substrate and for θ = 45°, respectively. We observe resonant behaviours of the electric and magnetic fields with a linear red shift when the length of the nanoslit increases. In the following, we will focus on a nanoslit length of 80 nm, yielding a resonance at 680 nm. The reason for this is that we are mainly targeting visible applications and molecules that absorb in this wavelength range. The biomolecule that our team was considering was a light-harvesting complexes (LHCII) extracted from plants. These are chiral molecules that have been selected throughout evolution to harvest the energy of light extremely efficiently, which make them very interesting for photovoltaic technologies for instance. They also present model system for the study of quantum coherence in systems in contact with the environment. The Light Harvesting complexes present a strong absorption band in the red part of the visible spectrum associated with circular dichroism which make them ideal probes to study the electromagnetic coupling of chiral molecule to plasmonic resonators.

However, as shown in Figure 21, by changing the length of the nanoslit, the entire spectrum is accessible.

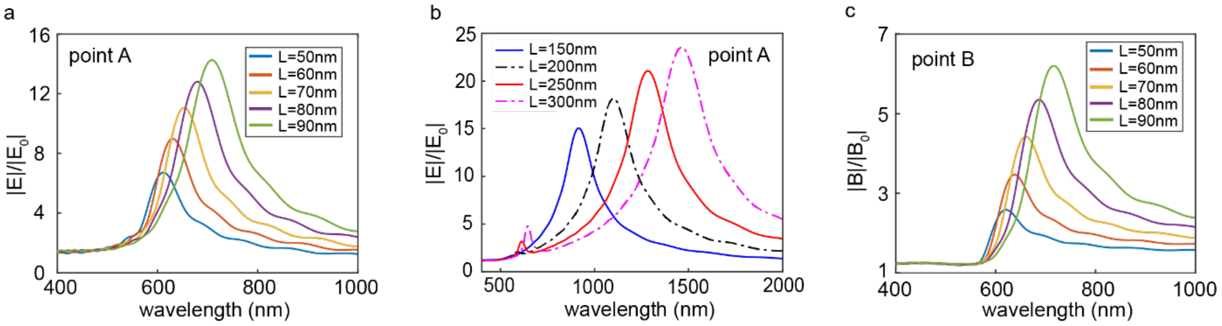

Figure 21 *Spectral responses of the magnetic dipolar nanoslit.* ***a) b)*** *Electric and* ***c)*** *magnetic spectral responses for different lengths of the optical nanoslit shown in Figure 20a, for a width of 20 nm and θ = 45°. The spectra represent the electric and magnetic fields normalized by the incident wave, respectively, at points A (geometric center of the nanoslit in the three dimensions of space) and B (at the center of the nanoslit in XZ and 5 nm from the edge of the nanoslit in Y), as shown in the inset in Figure 20b.*

The resonant behaviour of the electric and magnetic fields agrees well with the variations expected for a resonant object. A continuous variation of the resonance position with length was also observed as can be seen in the Figure 21b (for the lengths up to the IR). It is also noticeable in Figure 21 that the magnitude of the fields increases when the aspect ratio of the nanoslit increases. Another way of playing with the aspect ratio of the nanoslits can be achieved through the modification of the thickness of the gold layer (Figure 22). As can be seen, increasing thickness results in a shifting of the resonance towards the blue up to a saturation level associated with the presence of the inter-band transitions of gold.

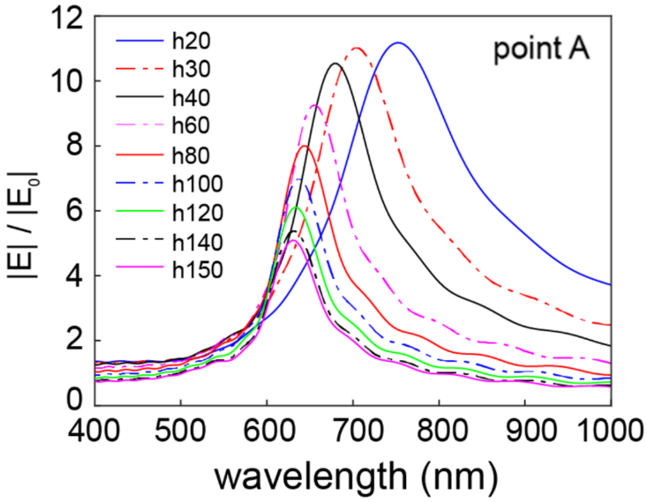

Figure 22 *Spectral response in electric field enhancement for gold nanoslit of width 20 nm, length 80 nm, and different thicknesses.*

The amplitude variations are directly associated with the position of the resonance and the reduction of the ohmic losses in gold when the wavelength of light increases. At this stage, I have shown that nanoslit behave as plasmonic resonators with resonant properties all mirroring those of nanorods according to the Babinet’s principle.

3.3.2 Electric and magnetic energy density

Figure 23a and Figure 23b display the time-average electric and magnetic energy density $U_e = \frac{\varepsilon_0}{4}|\boldsymbol{E}|^2$ and $U_b = \frac{|\boldsymbol{B}|^2}{2\mu_0}$ at the points A and point B of the nanoslit as a function of the wavelength of the incoming plane wave and of the angle of its linear polarization with respect to the nanoslit for angles comprised in the range [-90:15:90]. We see that U_e and U_b are maximum at λ = 680 nm for a polarization angle of $\theta = 0^{\circ}$ corresponding to a polarization along the short axis of the nanoslit.[60, 61] These observations support the hypothesis of a magnetic dipole character for the nanoslit. It is important to notice that the electric and magnetic energy densities are the same inside the nanoslit for opposite angles ±θ.

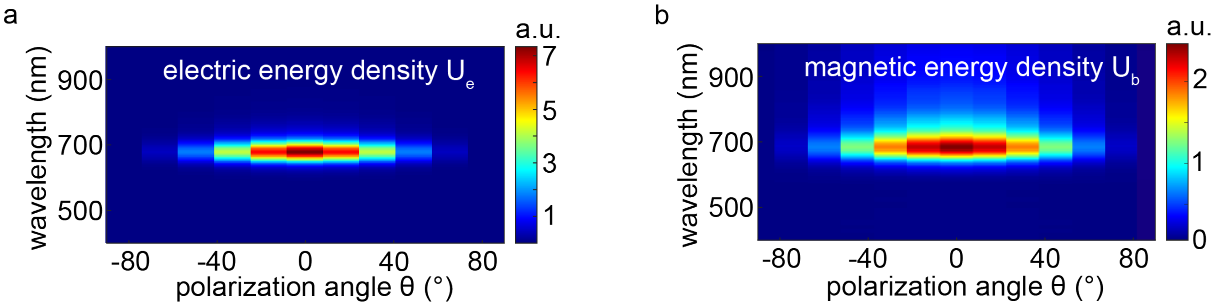

***Figure 23** Spectral responses of the **a)** electric energy densities U_e and **b)** magnetic energy densities U_b simulated by FDTD as a function of the incident polarization angle θ and wavelength respectively at points A and B (inset of Figure 20b) for nanoslit.*

A second mode is expected for the electric field of light polarized along the long axis of the nanoslit. In a nanorod it would correspond to the transverse mode (observed for light polarized perpendicularly to the short axis of the nanorod. This mode is expected to be around 530 nm but is strongly damped by the inter-band transitions of gold and cannot be seen with the colour scale used in Figure 23. However, it can be observed in the plot of $|\boldsymbol{E}| \,/\, |\boldsymbol{E_0}|$ for a polarization angle of ±90° and is presented in Figure 24a. This mode will not contribute significantly to the chiral properties inside the nanoslit, and it will not be further discussed in this Chapter. However, its presence will be of major importance in the ellipticity of the fields and it will be discussed in the next Chapter.

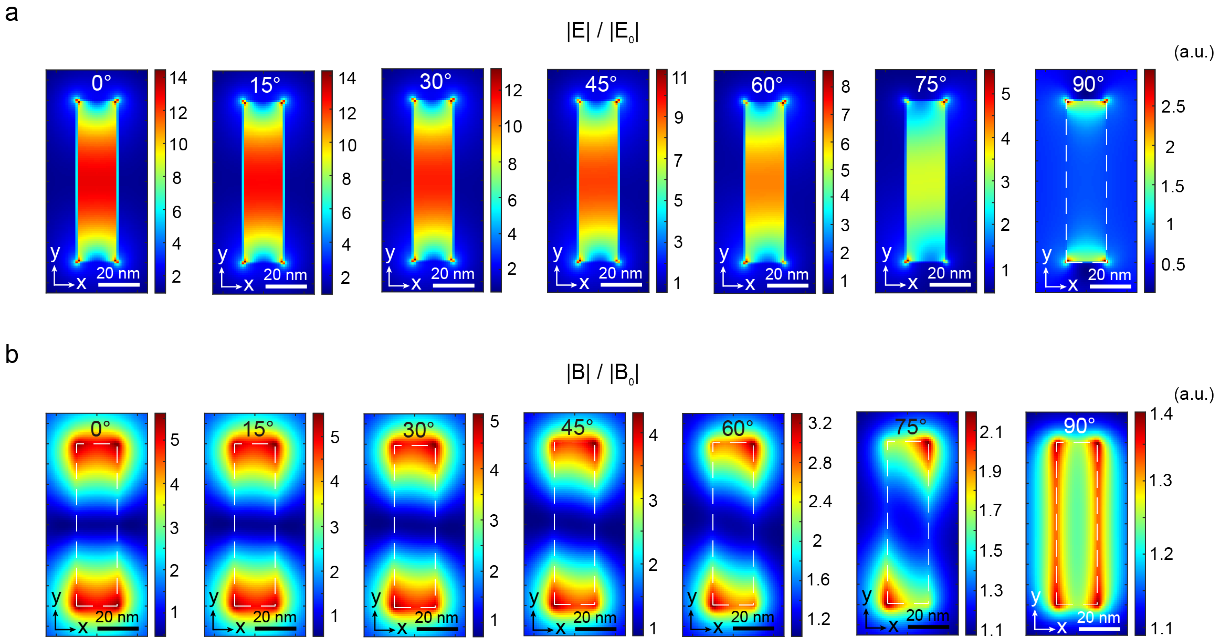

Figure 24 *Evolution for different θ angles of* ***a)*** *electric and* ***b)*** *magnetic field distributions at the Z-middle of a gold nanoslit 80 nm long, 20 nm wide, and 40 nm thick for wavelengths 645nm, corresponding to the chirality density maxima for linear excitation polarization as we will see in Section 3.4.*

Another comment concerns the uniformity of the fields inside the nanoslit near resonance. The field maps calculated using different incident linear polarizations are shown in Figure 24. The electric field enhancement remains very uniform inside the nanoslit up to very steep polarization angles (75° here). Its magnitude is only reduced constantly as can be inferred from Figure 23a. The magnetic field enhancement seems to be slightly more sensitive to the excitation field orientation although it remains confined at the ends of the nanoslits. We will see in the next paragraphs that these properties are very important to explain the uniformity of the chirality of the fields inside the nanoslit and their variations with wavelength. Obviously, for a polarization angle of 90°, the main resonance is no longer excited, and the field enhancement is much smaller and reflects the local polarizations at the edges of the nanoslit.

In order to describe the electromagnetic behavior of this nanoslit further, Figure 25a and Figure 25b provide the spatial distributions of the electric and magnetic field enhancements in the observation plane of the nanoslit, and excited for θ=45° at the the resonant frequency (λ=680 nm). Indeed, as we will see later, we found that the highest chiral density was under these illumination conditions. In particular, the E-field is concentrated homogeneously in the center of the nanoslit while the B-field is maximum at the edges. Also, these electric and magnetic fields are increased by a factor of about 13 and 6 with respect to the incoming light, respectively.

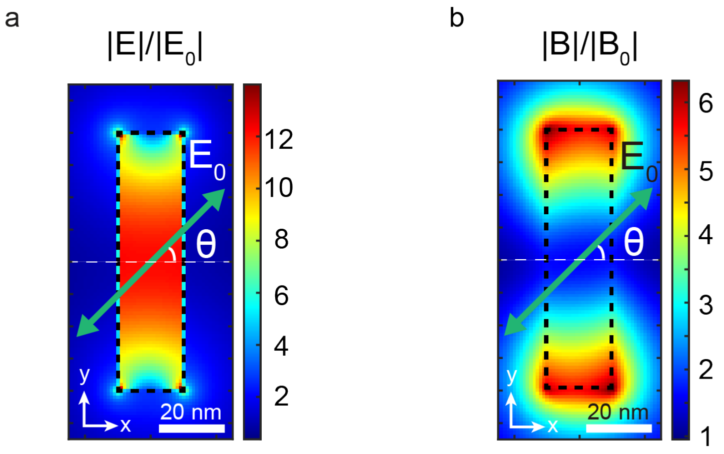

Figure 25 *Electromagnetic field distribution and spectral energy responses. Spatial distribution of* ***a)*** *electric and* ***b)*** *magnetic fields in an XY plane at the center of the nanoslit in Z, at lambda=680 nm, and for a polarization angle θ = 45°.*

In the next sections I will address the chirality density of the electromagnetic field inside the nanoslit and propose an explanation for the properties observed. I will investigate then the robustness of the effects against variations in shape and organization of the nanoslits.

3.4 Chirality density of nanoslit

3.4.1 Spectral responses of the chirality density

From the electromagnetic fields calculated and displayed in Figure 25a and Figure 25b, I have computed the chirality density enhancement C_{enh} in the nanoslit, defined as $C_{enh} = \frac{C}{C_{CPL}}$, with C_{CPL} the chirality density of a circularly polarized light, without the aperture, carrying the same power as the linearly polarized excitation impinging on the nanoslit. Figure 26 presents C_{enh} at the geometric center point A of the nanoslit as a function of the wavelength for two polarization angles (45° and -45°). The results are striking. As we can see, for opposite polarization angles θ=±45°, the sign of chirality density is reversed. Also, and surprisingly, the sign of the chirality density is changed when crossing the resonant frequency of 680 nm, C_{enh} being close to 0 at the resonance. Two opposite extrema are then observed on each side of the resonance, one at 645 nm and the other at 718 nm, with chirality density enhancements of respectively 4.5 and 3.5, in absolute value.

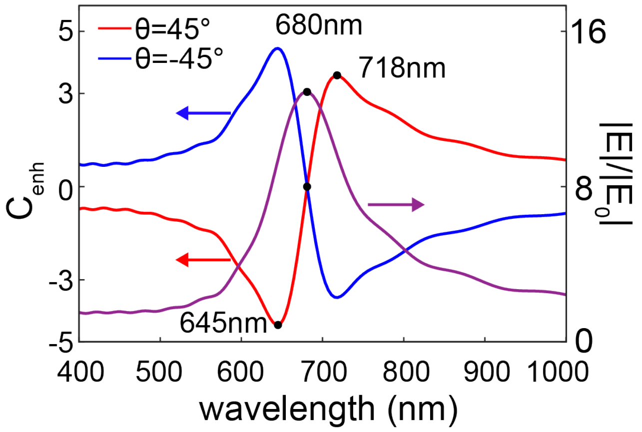

Figure 26 *Spectral responses of the chirality density. Spectral responses in chirality density (blue and red lines) and intensity (purple line) for a nanoslit of length 80 nm, width 20 nm, for two opposite angles θ = ±45° and at point A (inset of Figure 20b).*

The enhancement of the chirality density C_{enh} in the nanoslit was calculated at point A in the center of the nanoslit for any polarization angle θ and the wavelength range from 400 to 1000 nm (Figure 27). This plot generalizes what was observed in Figure 26. The chirality density disappears when the incident polarization is along the short nanoslit axis (x-axis or θ=0°) or the long nanoslit axis (y-axis or θ=90°).

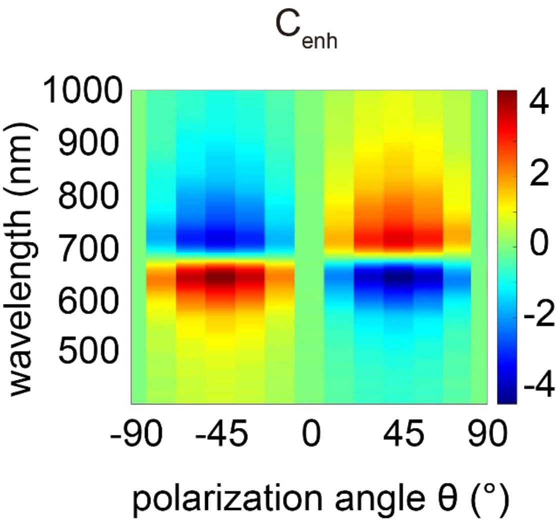

Figure 27 *Variations of C_{enh} as a function of the incident polarization angle θ and wavelength in the center of the nanoslit.*

For different polarization angles, we consider the average chiral density in the internal volume of the nanoslit, called the volumetric chirality density C_{vol}. Indeed, as we can see, not only for opposite polarization angles θ=±45°, the sign of average chirality density is reversed, but also something that is true for any pairs of opposite angles θ but with a lower magnitude of C_{enh} (Figure 28).

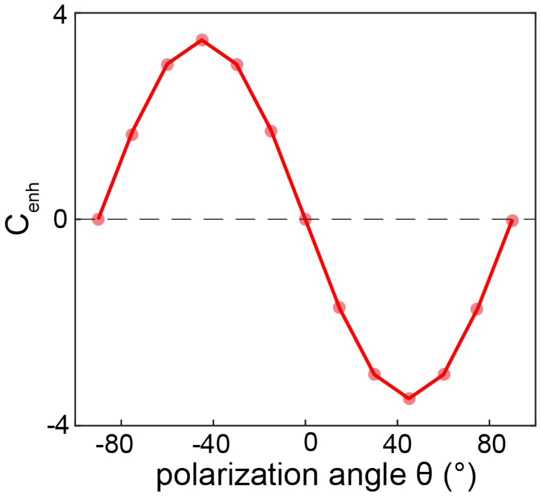

Figure 28 *Volumetric chirality density inside the nanoslit for different angles θ of the linear polarization of the excitation light.*

3.4.2 Spatial responses of the chirality density

From these results, the spatial distributions of the chirality density in the observation plane and for the wavelengths of 645, 680 and 718 nm are shown in Figure 29a and Figure 29b, for θ = +45° and θ = -45°, respectively. Remarkably, while the local chirality density distributions around positive plasmonic antennas (disks, nanorods, gammadions…) have always been observed as non-uniform[61, 62], in this case, they are perfectly homogeneous at the wavelengths of the two extrema (645 and 718 nm). Also, as we can see in Figure 29a and Figure 29b, the sign of the chirality density changes altogether by switching the polarization from +45° to -45°. Therefore, the nanoslit provides a pure chiral light tunable using either the incoming wavelength or polarization and free of any background. Surprisingly, the chirality distribution averages 0 within the nanoslit at the resonance wavelength for a linearly polarized excitation. The spatial response of the chirality density in different planes is shown in Appendix 2.

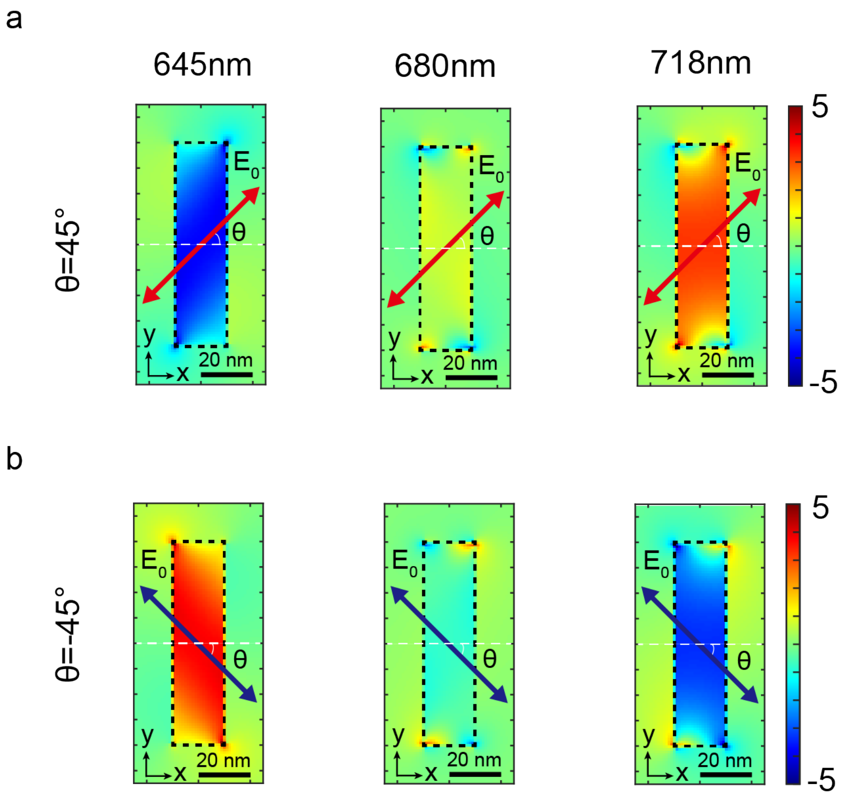

Figure 29 *Spatial distribution of the chirality density in an XY plane within the nanoslit in Z, for three characteristic wavelengths and for* ***a)*** *θ = +45° and* ***b)*** *θ = -45°.*

3.5 Comparison with nanorods

3.5.1 Chirality density enhancement study for nanorod

The chiral field around nanorods has been observed to exhibit significant inhomogeneity, as documented in references 61 and 62. This suggests that the chirality density distribution around nanorods is not uniform, which may affect their ability to consistently interact with chiral molecules.

In contrast, nanoslits appear to offer a distinct advantage in terms of the homogeneity of their chiral field. The distribution of chiral field strength within the center plane of nanoslits is remarkably uniform, as I have shown. This homogeneity can be advantageous when probing the chirality of molecules in solution, especially when molecules flow within the confined space of the nanoslit. It implies that the chiral interaction experienced by molecules passing through nanoslits is relatively consistent throughout the volume, making it a practical choice for experiments involving the detection of chiral molecules in solution.

However, it is important to note that in practical experiments, such as using resonators to probe the chirality of molecules in solution, the molecules themselves are in motion within the solution. This dynamic environment can introduce additional complexity into the assessment of chirality density. Therefore, to make a meaningful comparison between nanorods and nanoslits, it is critical to quantitatively assess and compare the magnitude of chirality density within the same volume when molecules are present and in motion. This will provide valuable insights into the practical effectiveness of nanorods and nanoslits in the detection of chiral molecules, taking into account both their intrinsic properties and the dynamic nature of the experimental setup.

The volumetric chirality density C_{vol} generated by the nanoslit is compared to that of a gold nanorod, having the dimensions W=20 nm, H=40 nm and L=70 nm, and creating a C_{enh} maximum at λ = 645 nm.

I have numerically calculated the spectral variations of $C_{enh}$for an incident polarization angle θ of 45° in the wavelength range 400-1000 nm for a nanorod consisting of gold deposited on glass. C_{enh} values were monitored at point C located 5 nm from one end of the nanorod and 20 nm above the glass substrate, where the increase in the electric field was most significant

(Figure 30a). I have first determined the dimensions of a nanorod that would have a C_{enh} extremum at the same wavelength as that observed at the lowest nanoslit wavelengths, i.e., at 645 nm (Figure 26). For this purpose, I have used a width (W) of 20 nm and a height (H) of 40 nm and adjusted the length (L). It was found that C_{enh} was maximum at 645nm for a length L=70 nm (Figure 30b). In contrast to the case of the nanoslit (Figure 27), we can see that the sign of the chirality density is always the same throughout the spectral range for a given polarization angle (Figure 30b). [49]

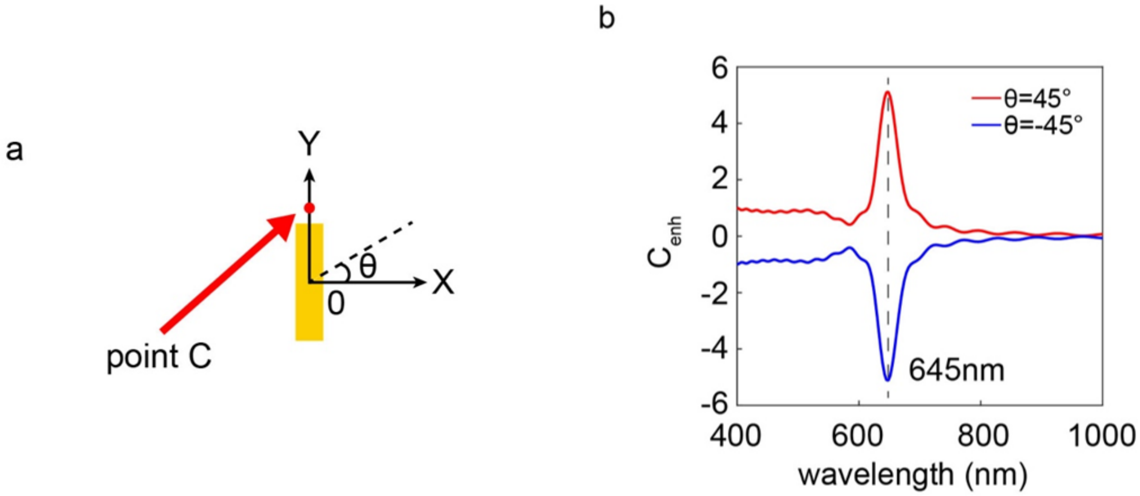

Figure 30 a) *Schematic of the nanorod and position of the point C.* ***b)*** *Variations of* C_{enh} *as a function of the wavelength for a nanorod with dimensions W=20nm, H=40nm and L=70nm, and θ =* $\pm 45°$*.*

3.5.2 Volumetric chirality density

The determination of C_{vol} shown in Figure 31a and Figure 31b was obtained with the dimensions mentioned above. I have simulated the electromagnetic response of both types of antennas (nanoslit and nanorod) supported by glass and excited by a plane wave propagating along the positive Z-axis from the substrate. The wavelength was set to 645 nm and the incident field was linearly polarized with an angle θ with respect to the short axis of the nanoslit and nanorod (Figure 31a and Figure 31b). If we assume that such antennas could be exploited experimentally to study chiral molecules, in the case of the nanoslit, only the internal volume of the nanoslit should be considered useful in terms of nearfield light-matter interactions, and this volume is equal to 64000 nm^3. On the other hand, only the part surrounding the nanorod would be accessible to potential chiral molecules, which, for a similar volume, corresponds to a thickness, of 6 nm around the nanorod (64704 nm^3, when neglecting the plane on which the nanorod sits on the glass substrate). Figure 31c plots C_{vol} for the nanoslit and nanorod as a function of the angle θ. Several observations can be made. First, we see that for the same angle, the volumetric chirality densities have opposite signs. Second, in absolute value, the nanoslit featured C_{vol} values that are increased by a factor of 9 compared to the nanorod, for all polarization angles. This is due to the non-uniformity of the chirality density around the nanorod which decreases the volumetric average C_{vol}, in contrast to the nanoslit which generates a pure chiral light as illustrated by the insets of Figure 31c. In the insets of Figure 31c, the chirality density distributions were calculated in middle plane of the nanoslit and 5 nm above the nanorod. Finally, the comparative advantage of the nanoslit is not limited to the increase of the chirality density in the nearfield but must also be highlighted with respect to the interaction volume that a far field excitation generates. Indeed, while the chiral signal provided by the nanoslit would be free of any background signal due to the opacity of the gold layer in the case of transmission measurements, the one generated by the nanorod would be added to background chiral light-matter interactions occurring during the propagation of the incoming plane wave far from the antenna. This is something that must be considered if one wants to use such achiral antennas experimentally.

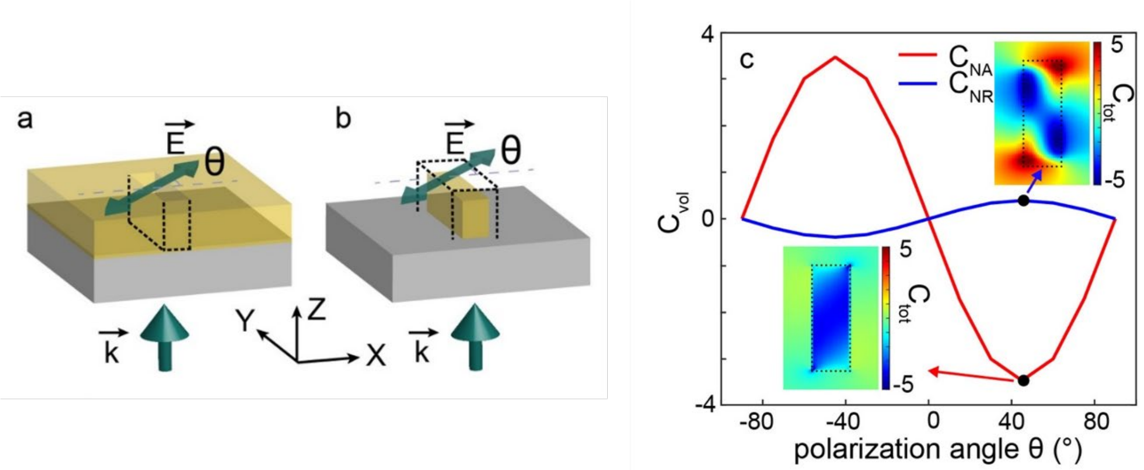

__Figure 31__ Comparison of gold nanoslit versus nanorod. Schematic representations of __a)__ the nanoslit and __b)__ the nanorod, excited by a plane wave linearly polarized by an angle θ with respect to the transverse axis of the antennas (Ox). The dotted lines determine the volume considered in the calculation of C_{vol}. __c)__ Volumetric chirality density inside the nanoslit and in the nearfield of the nanorod for different angles θ of the linear polarization of the excitation light. In the insets are represented the spatial distributions of the chirality density around these two antennas for θ = +45°, demonstrating the inhomogeneity of C in the case of the plasmonic nanorod.

3.6 Point like dipole model

The Babinet Principle is a fundamental concept in electromagnetism that describes the relationship between the diffraction patterns produced by complementary infinitely thin and perfectly conducting objects. It states that the diffraction pattern produced by an object is complementary to the diffraction pattern produced by its aperture or negative counterpart. In other words, if you have two objects, one with an aperture (opening) and the other with a solid structure in place of the aperture, the sum of their diffraction patterns will produce a uniform plane wave. This principle is widely used in optics and electromagnetic theory to understand and design various optical devices, such as diffraction gratings, and to manipulate the behavior of light at the nanoscale, as in the case of nanorods and nanoslits. In addition, if the nanorod can be modelled by an electric dipole $\boldsymbol{p}$, the nanoslit should be modelled by a magnetic dipole $\boldsymbol{m}$.

3.6.1 Equivalent to a magnetic dipole

To describe the response of the nanoslit, I have used a 3x3 diagonal magnetic polarizability tensor α^{mm}. In the Cartesian reference frame, with the nanoslit in the Oxy plane having its minor axis along x and neglecting the transverse mode because of the small field generated, only the first element $\alpha_{xx}^{mm}(\lambda) = \alpha'(\lambda) + i\alpha''(\lambda) \neq 0$. I will describe its spectral dependence with a Lorentzian profile (Figure 32). The Lorentz oscillator is centered at 677 nm with a broadening of 67 nm and has an amplitude of unity. The spectral position and broadening were chosen so as to fit to the calculated field enhancements.

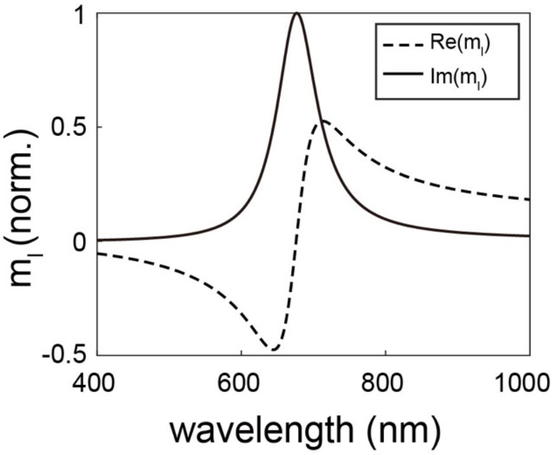

Figure 32 *Spectral dependence of the real and imaginary parts of* α_{xx}^{mm}

The magnetic moment $\boldsymbol{m}$ of the nanoslit is obtained as:

$$\boldsymbol{m} = \alpha^{mm}.\boldsymbol{H_o} \qquad 37)$$

with $\boldsymbol{H_o} = \boldsymbol{B_o}/\mu_o$ with $\boldsymbol{H_o}$ the magnetic field of the incident wave. The incident plane wave propagated along the z-axis and was linearly polarized with an angle θ with respect to the x-axis. The normalized coordinates of the incident electric field were $\boldsymbol{E_o} = (\cos\theta, \sin\theta, 0)$. The incident magnetic field was then obtained as $\boldsymbol{B_o} = \frac{1}{c}\boldsymbol{k} \times \boldsymbol{E_o}$ with $\boldsymbol{k}$ the wavevector of the incident light.

The total fields radiated by a point-like magnetic dipole with moment $\boldsymbol{m}$, containing both nearfield and far-field contributions and decomposed in a magnetic field $\boldsymbol{B}_{rad}$ and an electric field $\boldsymbol{E}_{rad}$ contributions observed in the direction n at a distance r from the position of the dipole, are given by:[63]

$$\boldsymbol{B}_{rad} = \frac{1}{4\pi\mu_o}\left\{k^2(\boldsymbol{n} \times \boldsymbol{m}) \times \boldsymbol{n}\frac{e^{ikr}}{r} + [3\boldsymbol{n}(\boldsymbol{n}.\boldsymbol{m}) - \boldsymbol{m}]\left(\frac{1}{r^3} - \frac{ik}{r^2}\right)e^{ikr}\right\} \qquad 38)$$

$$\boldsymbol{E}_{rad} = -\frac{Z_o}{4\pi}k^2(\boldsymbol{n} \times \boldsymbol{m})\frac{e^{ikr}}{r}\left(1 - \frac{1}{ikr}\right) \qquad 39)$$

with Z_o the impedance of vacuum.

3.6.2 Chiral field calculation of magnetic dipoles

We note that $\boldsymbol{E}_{rad}$ and $\boldsymbol{B}_{rad}$ are always orthogonal; therefore, the chirality density $C_{rad} = -\frac{\varepsilon_0 \omega}{2} Im\left(\widetilde{\boldsymbol{E}}_{rad}{}^{*} \cdot \widetilde{\boldsymbol{B}}_{\boldsymbol{rad}}\right)$ is always equal to zero. This is exactly what was found for the electric dipole in the works published described above. This means that for the nanoslit, any chirality density will also result from the superposition of the incident field and the radiated field. In order to generate chirality, it is then necessary to add the contribution of the incident fields ($\boldsymbol{E}_o$, $\boldsymbol{B}_o$) which are here linearly polarized.

The superposition of the two linearly polarized transverse fields, incident and radiated, and the phase shift between them results in an elliptically polarized light. The phase shift reaches π/2 when the dipole is driven at resonance, and it varies gradually with frequency between 0 and π due to the broadening of the Lorentzian profile chosen here for the polarizability. The total chirality density is then obtained as:[61,62,64]

$$C_{tot} = -\frac{\omega \varepsilon_0}{2} Im((\boldsymbol{E}_{rad} + \boldsymbol{E}_o)^{*} . (\boldsymbol{B}_{rad} + \boldsymbol{B}_o)) \qquad 40)$$

A final important ingredient of the model was to consider the enhancement of the nearfields in the nanoslit, as suggested by the numerically calculated field maps (Figure 21a and Figure 25a). It can be seen from these distributions that the electric field is mainly enhanced by a factor ξ, especially in the area where the chirality density is large, so that $\xi = \frac{\boldsymbol{E}_{tot}}{\boldsymbol{E}_o} = \frac{\boldsymbol{E}_{rad} + \boldsymbol{E}_o}{\boldsymbol{E}_o}$. To reproduce this effect, I have applied a field enhancement factor ξ, to the radiated electric field only, so that $\boldsymbol{E}_{rad} \rightarrow (\xi - 1)\boldsymbol{E}_{rad}$ while $\boldsymbol{B}_{rad}$ remained unchanged resulting in:

$$C_{tot} = -\frac{\omega \varepsilon_0}{2} Im([(\xi - 1)\boldsymbol{E}_{rad} + \boldsymbol{E}_o]^{*} . (\boldsymbol{B}_{rad} + \boldsymbol{B}_o)) \qquad 41)$$

The total chirality density was then calculated taking all these contributions into account. Finally, using Eq. 37), Eq. 38) and Eq. 39) of Chapter 3 in Eq. 41), the total chirality density is given by:

$$C_{tot} = \frac{\omega}{8 Z_o c^2 r^3} [k.r.\xi(\alpha' + k.r.\alpha'') - \alpha''] . sin(2\theta) \qquad 42)$$

This relation explicitly shows the $sin(2\theta)$ dependence of the sign of the chirality density on the polarization angle and in particular the change in sign as the polarization angle changes from θ to $-\theta$. Eq. 42) also shows that the chirality density should be maximal at ±45°. If we neglect the $k.r.\alpha''$ which yields a $(k.r)^2$ term and use 45° for θ, we find:

$$C_{tot} \approx \frac{\omega}{8Z_o c^2 r^3}\left[k.r.\xi.\alpha' - \alpha''\right] \qquad 43)$$

Figure 33a shows the spectral dependence of C_{tot} derived from Eq. 41), 20 nm above the dipole in z and for both polarization angles ±45°. The results observed are in excellent agreement with the spectral responses of the nanoslit (Figure 26). The sign of the chirality density changes with the angle of the polarization of the plane wave incident on the dipole. These observations are perfectly explained by Eq. 42) due to the $sin(2\theta)$ term. An inversion of the sign of the chirality density is found at the resonance of the magnetic dipole, with two spectral extrema on each side of the resonance's wavelength. This spectral dependence can be directly related to the large field enhancement factor which allows the term $k.r.\xi.\alpha'$ of Eq. 43) associated with real part of the magnetic dipole moment to dominate the α'' term in the spectral variations of C_{tot}. One can expect the spectral variations of C_{tot} to be dominated by the imaginary part of the magnetic dipole moment for smaller electric field enhancements.

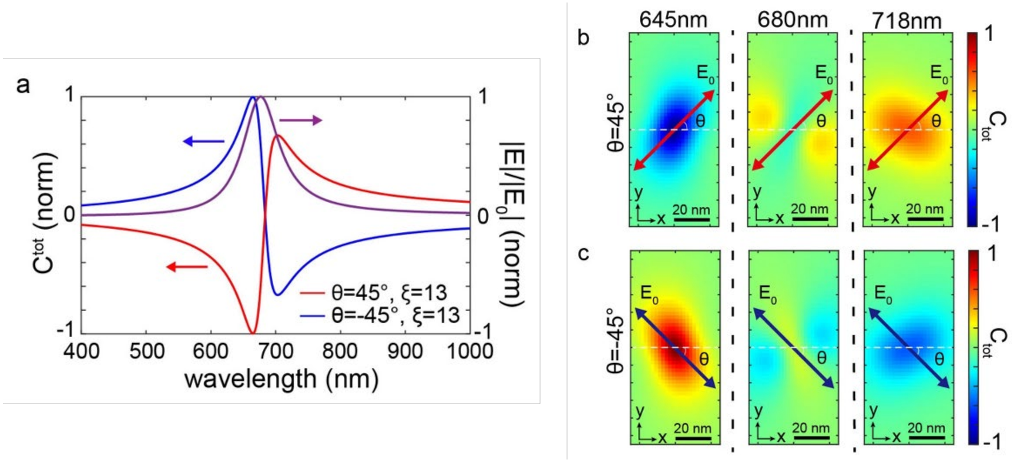

Figure 33 *Spectral and spatial chirality density responses obtained using a magnetic dipole model.* ***a)*** *Spectral chirality density and intensity responses 20 nm above a magnetic dipole interacting with a linearly polarized plane wave propagating along the positive Z axis and having a polarization angle relative to the dipole of θ = ±45°. Spatial distribution of the chirality density in an XY plane, 20 nm above the magnetic dipole, for the three characteristic wavelengths corresponding to the extrema and the resonance and for* ***b)*** *θ = +45° and* ***c)*** *θ = -45°.*

Also using the expression of C_{tot} (Eq. 41)), the chirality density distributions in an Oxy plane 20 nm away from the dipole were calculated and are shown in Figure 33b. We used an incident polarization of 45° and -45°, a field enhancement ξ = 13 and wavelengths of 645 nm, 680 nm, and 718 nm. In addition to the sign change, another striking feature is that the C_{tot} field distribution becomes very uniform. These field maps are in excellent qualitative agreement with those calculated numerically within the nanoslit in Figure 29. This confirms that the critical parameter for obtaining spatially uniform values for the total chirality density is to generate a strong electric field enhancement as spatially extended as possible. This feature is achieved in the nanoslit (Figure 25a), resulting in a uniform distribution of chirality density within the nanoslit volume.

As presented in Figure 33, with a value of ξ = 13, this model reproduces quite well the variation of C_{tot} as a function of wavelength and polarization angle. I present in Figure 34 the influence of the value of ξ on the spectral dependence of C_{tot} for a polarization angle of 45° and at 20 nm above the point-like dipole. Using a polarization angle of -45° would give exactly opposite spectral variations, they are not shown here for clarity.

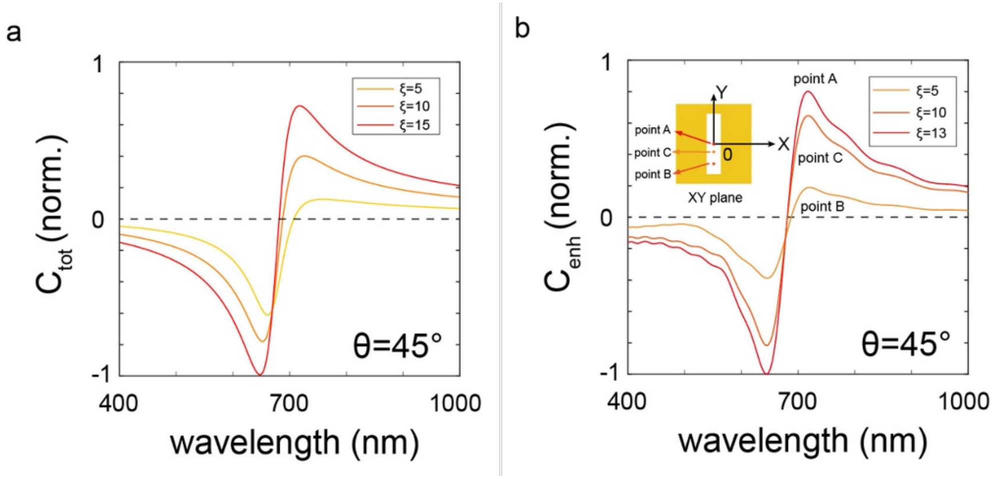

***Figure 34** Spectral variation of C_{tot} calculated for different values of the electric field enhancement factor ξ for **a)** the dipolar model and **b)** the nanoslit. The values of C_{tot} were all normalized to the maximum value obtained (for $\xi = 15$ and wavelength = 646 nm).*

Figure 34a and Figure 34b compare the numerical calculations with the dipole model for different ξ values to test the validity of Eq. 43). The smaller values ξ were obtained in the nanoslit at different positions since the electric field enhancement can be reduced near the ends of the nanoslit while the magnetic field remains small as we have seen in Figure 34. It can be seen that excellent agreement is found between these two approaches, confirming that increasing the electric field is indeed an important parameter in assessing the chirality density in the vicinity of a nano-antenna.

3.7 Robustness of the chiral field of nanoslit

In this subsection, I will discuss how manufacturing defects affect the properties and response of the chiral field. Although manufacturing processes are advanced, they are not completely immune to defects and variations. These deviations from ideal geometry may introduce unexpected perturbations into the chiral field, which can alter its behavior and performance. To ensure the reliability and reproducibility of nanoslit, the effects of fabrication defects must be thoroughly investigated. I first attempted to process different sizes of nanoslit by e-beam lithography. Then I will use simulations to understand the relationship between fabrication errors and chiral field response using a parametric study.

3.7.1 Fabrication processing

The fabrication process I have described for creating nanoslits using e-beam lithography is a precise and complicated technique used in nanofabrication. Here's a step-by-step breakdown of the process (Figure 35):

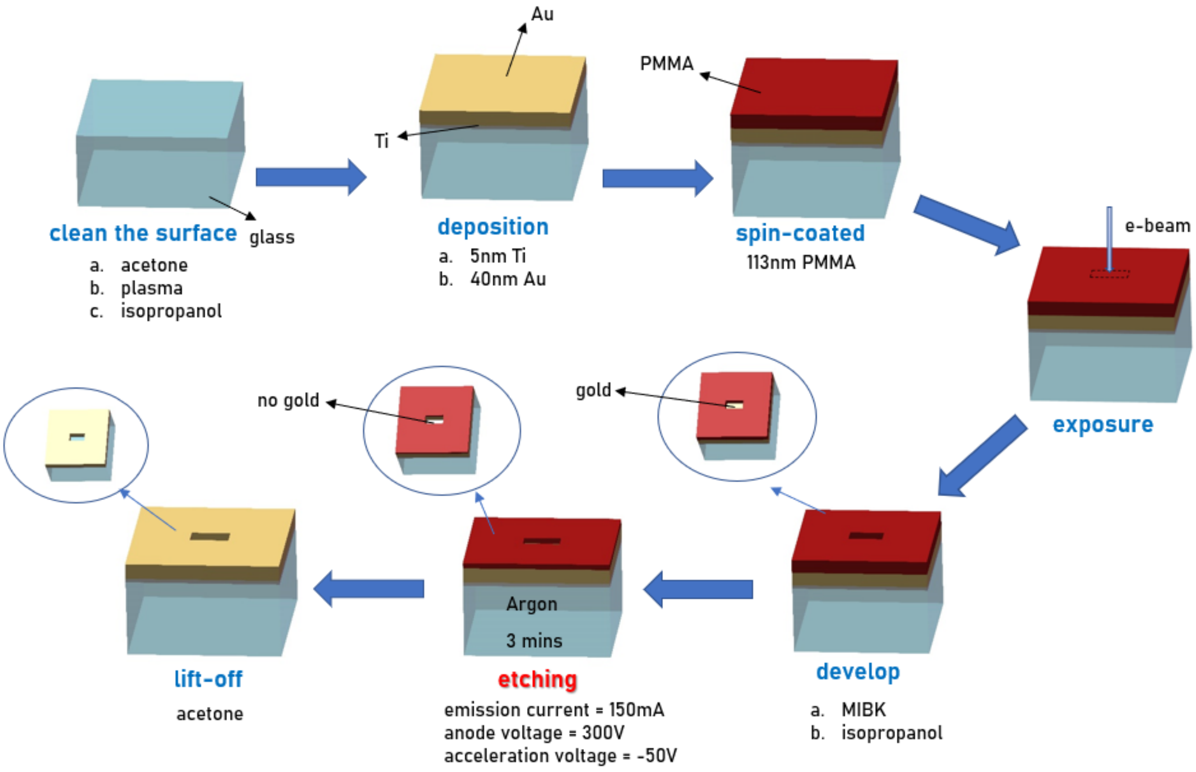

Figure 35 *The process of creating nanoslits using e-beam lithography.*

1. Surface Cleaning:

The process starts with surface preparation. The substrate is cleaned to remove any contaminants. This is accomplished by a combination of an ultrasonic bath (37 kHz) in acetone for 1 minute and isopropanol solution rinsing, followed by an oxygen plasma treatment for 5 minutes. The plasma treatment was used to further clean the surface and possibly modify its properties to make it more suitable for the subsequent steps.

2. Metallization:

In the second step, thin layers of materials are deposited on the cleaned surface. First, a 5nm of adhesion layer of titanium (Ti) is deposited, followed by a 40nm thin film of gold (Au). This layer serves as the starting point for creating the nanoslit structure.

3. Resist deposition:

To create a protective layer and facilitate the subsequent patterning step, a 113 nm of polymethyl methacrylate (PMMA) is spin-coated onto the Au surface. The resist is then annealed on a hotplate at 180°C for 1 minute to ensure a good polymerization. The PMMA layer will act as a resist material and its thickness is carefully controlled in this step.

4. E-beam exposure:

The desired pattern for the nanoslit is exposed to the PMMA-coated surface using e-beam lithography. This involves directing a focused beam of electrons at an acceleration voltage of 20kV and a beam current of 20 nA onto the PMMA. Different doses multiple of 150µC were tested. This breaks the polymer in the exposed areas, allowing for the creation of the pattern of nanoslits in the development step.

5. Development:

After exposure, the PMMA layer is developed. This involves the selective removal of the PMMA affected by the e-beam exposure. The development is typically performed with a developer solution of methyl isobutyl ketone (MIBK) for 50 seconds and then isopropanol for 30 seconds.

6. Etching:

Etching was performed by an argon plasma through the exposed gold areas in the PMMA pattern. Importantly, the etch rate of the PMMA is slower than that of the gold, allowing selective etching of the gold while leaving the PMMA nearly intact in the areas where the nanoslits are defined. This selective etching process creates the nanoslits in the gold layer.

7. Lift-Off:

The final step is to remove any remaining PMMA from the substrate. This is done by washing the sample with an acetone solution at 40°C for 15 minutes. The acetone dissolves the PMMA, leaving behind the nanoslit structures in the gold layer.

3.7.2 Characterization of the nanoslit

The experimental design for processing nanoslits includes a 2cm × 2cm glass substrate with a 100-micron square central area. (Figure 36) This are containing nine subarrays, each measuring 20µm × 20µm and spaced 1µm apart. These subarrays are labeled from 1 to 9, and within each subarray, nanoslits of varying dimensions are created. The nanoslit dimensions increase incrementally from 20nm × 80nm in subarray 1 to 120nm × 240nm in subarray 9, with a constant aspect ratio. The spacing between adjacent nanoslits in each subarray is 500 nm, which defines the lattice constant. This design allows the effects of nanoslit processing to be studied under different conditions.

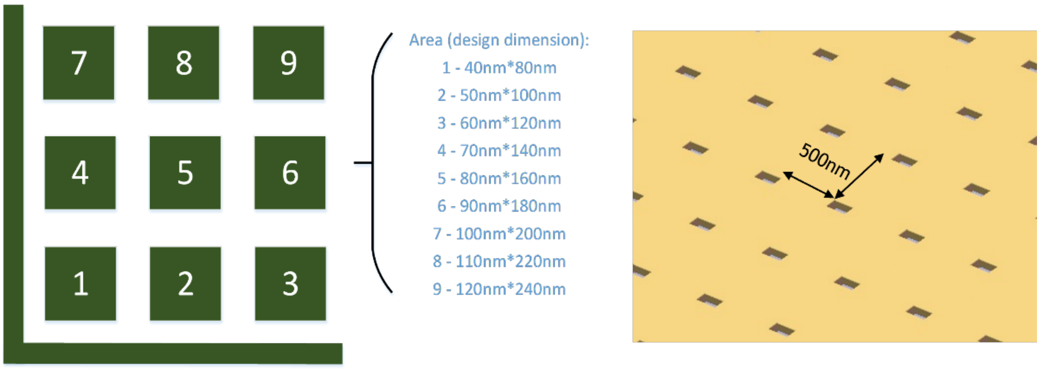

Figure 36 *Nanofabrication design of nanoslits sample*

In Figure 37, there are four sub-figures labeled a) – d). Sub-figures a) and b) represent patterns observed with an optical microscope. Sub-figure a) represents the entire region of the specimen and is taken in the BRIGHT-field, while sub-figure b) represents the entire region but is taken in the DARK-field. Subfigures c) and d) are scanning electron microscope (SEM) images. Sub-figure c) shows the entire region of the sample, while sub-figure d) specifically shows one of the sub-fields, providing a detailed SEM image of a specific portion of the sample. Some darker contrast can be observed in some areas, possibly originating from residual PMMA remaining on the surface.

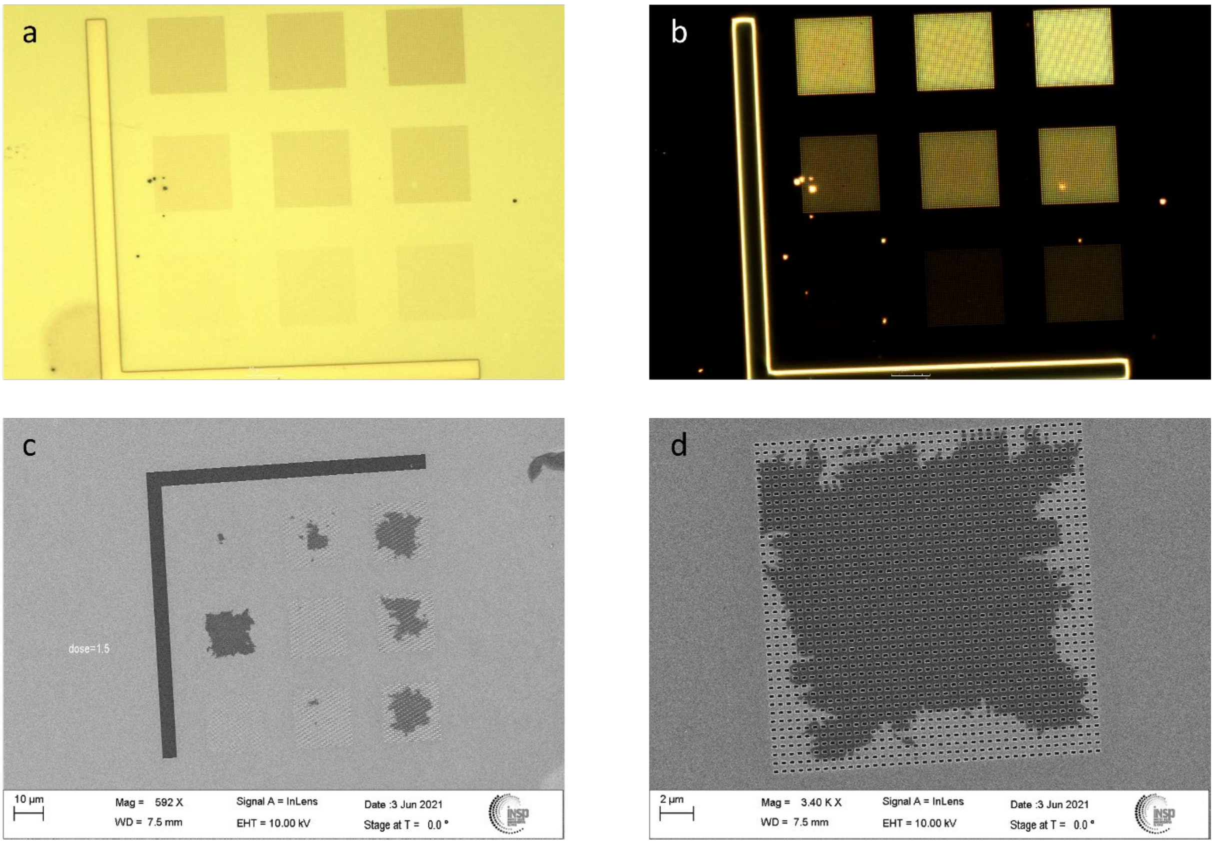

***Figure 37** Observations and Imaging. **a)** Optical microscope: BRIGHT field. **b)** Optical microscope: DARK field. **c)** SEM image of the entire sample region. **d)** SEM image to reveal specific features within that subarray.*

In Figure 38, higher magnification SEM patterns provide a closer examination of the nanoslits within different subarrays. Figure 38a, taken from a smaller size region, illustrates the challenges of maintaining a matrix shape as the nanoslit size decreases, resulting in irregular shapes within the nanoslits. In contrast, Figure 38b, taken from a larger size region, illustrates that a more distinct rectangular aperture shape emerges as the nanoslit size increases. However, a common observation persists across different sizes: the boundaries of each cell exhibit significant roughness, suggesting that the etching process reveals the grain structure of evaporated gold, regardless of nanoslit size.

Following the initial observations in Figure 38, efforts were made to improve the boundary roughness, resulting in Figure 39, which shows two different treatments. In Figure 39a, a different approach involving annealing was used, where the sample was placed on a 180℃ hot plate for five minutes. Alternatively, in Figure 39a, the Focused Ion Beam (FIB) method was used, which significantly improved the boundary roughness of the samples. While both treatments contributed to the reduction of edge roughness to varied degrees, it is evident that the apertures obtained were not perfect, making them less rectangular and more rounded in appearance.

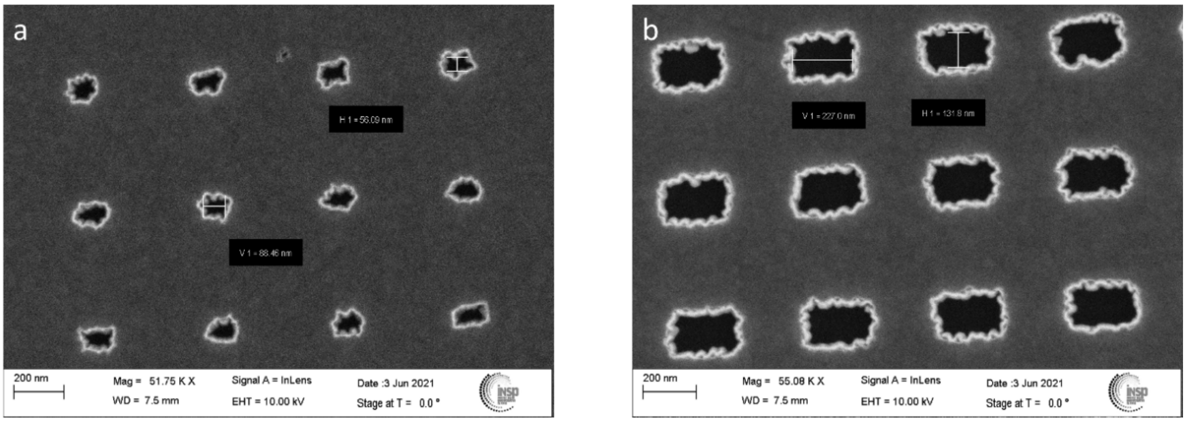

Figure 38 *SEM image of different size of nanoslits unit.*

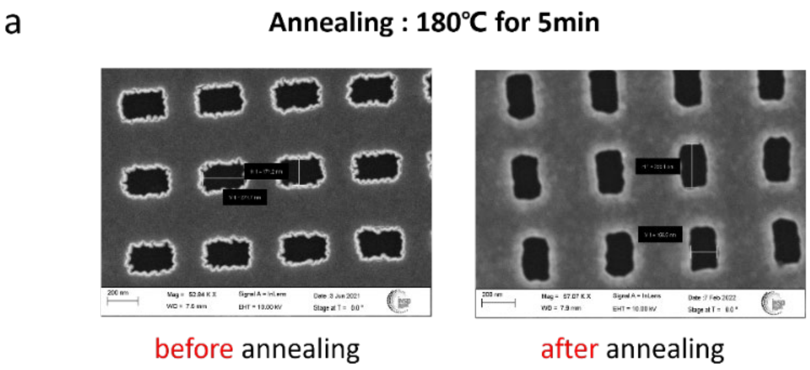

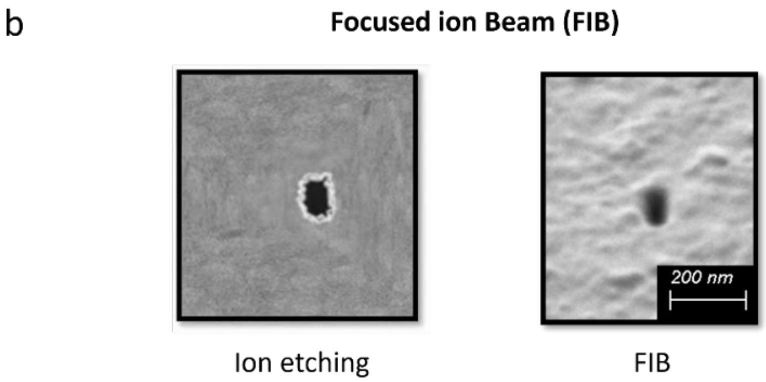

Figure 39 *Boundary roughness enhancement.* ***a)*** *Annealing: 180℃ for 5min* ***b)*** *Focused Ion Beam method.*

Given the challenges encountered during the nanoslit fabrication process, a series of simulations were performed in next subsection to comprehensively evaluate the effects of size variations, shape variations, and cell spacing. These simulations were designed to determine whether the observed discrepancies, would significantly affect the chiral field. Such investigations are crucial to elucidate the practical implications of these variations and guide the optimization of nanoslit design to achieve desired results in chiral field applications. I will plot the spectral dependence of the chirality density for illumination with a linear polarization at 45° from the long axis of the nanoslits. We must keep in mind that all the other properties or the fields will vary accordingly.

3.7.3 Influence of dimensions

We have seen in Figure 21b that by changing the nanoslit's length, the full red part of the spectrum could be covered. It must be noted that the thickness of gold is a parameter which is well controlled by the evaporation process. Going further in the green, blue, or even UV part of the spectrum will require changing the material for silver or aluminium. When the length of the nanoslits increases from 60nm to 100nm for constant width, i.e. the aspect ratio increases, the spectral dependence of the volumetric chirality density keeps its characteristic S-shape but it is shifted towards the near-infrared part of the spectrum as can be seen in Figure 40a. The amplitude of the S-shape increases too as a result of the decrease of the ohmic losses in gold when the wavelength increases as was stated in the description of Figure 21. I have plotted the chirality density map in the middle of the nanoslits for the characteristic wavelengths of the chirality density dispersion, i.e., at the two extrema and at the zero in between the extrema (Figure 40b). We can see that the increase of the amplitude of the S-shape reflects the increase in the chirality density everywhere inside the nanoslit while the distribution remains uniform.

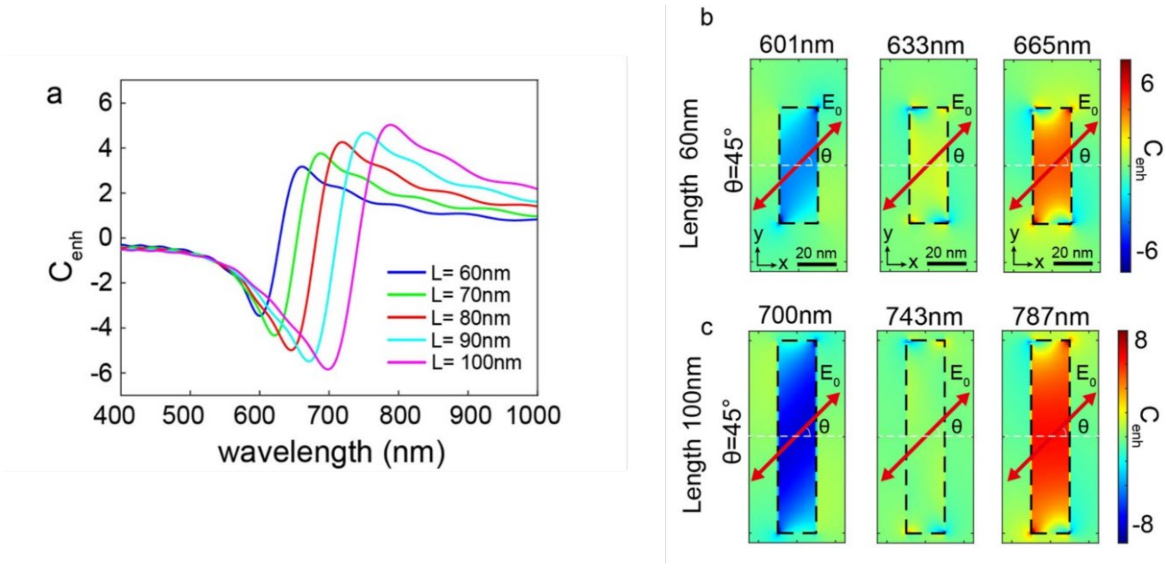

Figure 40 a) *Spectral responses in volumetric chirality density for nanoslits of different lengths made in a gold layer.* ***b)*** *L=60nm* ***c)*** *L=100nm Spatial distribution of chirality density at the center of several representative nanoslits for linear polarization at 45° from the short axis of the nanoslits and wavelengths corresponding to different extrema.*

Another way of varying the aspect ratio is obtained by varying the thickness of the gold layer. As one can see, increasing thickness results in a shifting of the resonance towards the blue up to a saturation level as expected since increasing the thickness results in a decrease of the aspect ratio.

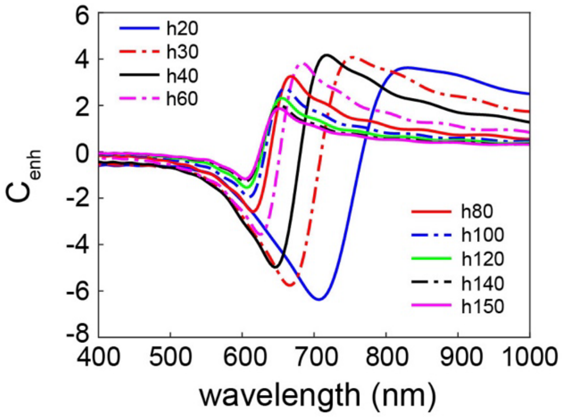

Figure 41 *Spectral response in field enhancement and chirality density for gold nanoslits of width 20 nm, length 80 nm, and different thicknesses.*

3.7.4 Influence of rounded edges

In Figure 39 we have seen that the shape of the nanoslits were not perfect rectangles even when fabricated with FIB. I have modelled the rounded edges introduced by the fabrication as a nanoslit with full rounded corners. It can be seen in Figure 42a that although the lineshape of the spectral dependence of C is maintained, a blueshift of nearly 26nm is observed. This can be understood as an effective reduction of the aspect ratio of the nanoslit. This means that the exact resonance position of the nanoslit will have to be controlled and the fabrication process will need to be adapted if a particular wavelength is targeted. Concerning the distribution of the chirality density inside the nanoslit, the usual uniform distribution is observed.

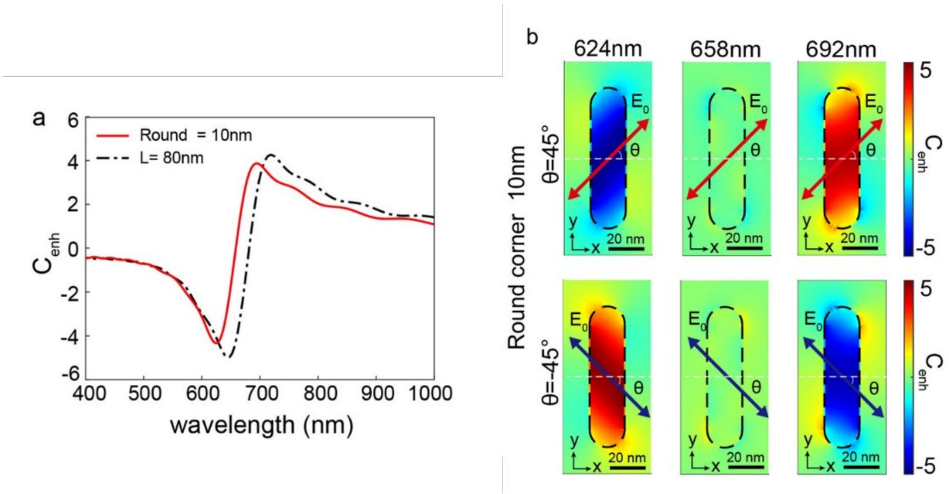

Figure 42 a) *Spectral responses in volumetric chirality density for two types of nanoslit, one with 90° angled corners and the other with rounded corners.* ***b)*** *Spatial distribution of the chirality density at the center of the nanoslit with rounded corners for different polarization angles and wavelengths corresponding to different extrema of a).*

3.8 Conclusion

In conclusion, this chapter highlights four key findings about nanoslits. First, nanoslits exhibit plasmon resonances similar to magnetic dipoles. Second, unlike nanorods, nanoslits exhibit a uniform chirality density that can be excited and manipulated by changes in polarization angle and wavelength. Third, a point-like magnetic dipole model accurately reproduces the simulation results when incident field and electric field enhancement are considered, with a tentative explanation suggesting that the uniform C arises from the uniform electric field within nanoslits. Finally, a parametric study shows that the optical properties of nanoslits, in particular their uniform chirality, remain robust to shape variations. Size and rounded edges induce wavelength shifts, highlighting the importance of optimizing the fabrication process for precise control even if the broad spectral response reduces the criticality of these imperfections. Additionally, the possibility to play with the excitation polarization gives some flexibility, as we will see in the next Chapter.

Chapter 4

Optimization of the Chiral Nearfields

4.1 Introduction

I have shown numerically that a plasmonic resonator based on a rectangular nanoslit could be described as a magnetic dipole and was behaving as a tunable nanosource of purely chiral light.

In Chapter 3, we have seen that for nanoslit, in the nearfield, the phenomena of chiral density and ellipticity have completely different spectral and polarization properties. By exploring the nanoslit for chirality density and ellipticity, I intend to explain mathematically why these two parameters behave so differently in the nearfield of the nanoslit.

Recent advances in computational capabilities and numerical methods, including FDTD and finite-element methods (FEM), have greatly expanded the capabilities of nanophotonic device design[65]. Pure brute force involves exhaustively searching through all possible combinations of parameters to find the optimal solution. While it guarantees finding the global optimum (if the search space is discrete and finite), it becomes computationally infeasible for problems with a large parameter space. When dealing with physical simulations like FDTD or FEM, brute force can be impractical due to the computational cost, especially for high-dimensional problems.

Techniques such as parameter sweep or stochastic optimization methods such as genetic algorithms (GAs) are only suitable for problems with a limited number of design parameters and are effective when a good initial guess is available. While GAs has an advantage over pure brute force in terms of efficiency, they still lack a direct integration of physics into the optimization process. The physical insight comes only through the formulation of the objective function, which represents the fitness of the solutions based on the physical criteria. However, GAs themselves do not directly use any physics-based knowledge to guide the search.

Deep learning algorithms are emerging as a promising alternative for inverse design in nanophotonics, but they require excessively large data sets for training and can be computationally expensive during both training and inference. When it comes to optimization, deep learning can be thought of as a way to learn and generalize patterns from a large library of data, but the process of generating this library can involve brute force or complex simulations. The underlying physics can be lost to some extent when using deep learning, especially if the neural network learns to approximate the underlying physics without fully understanding the underlying principles. The challenge is to ensure that the deep learning model captures the essential physics, rather than memorizing specific cases from the training data.

Gradient based methods (Levenberg-Marquardt, Newton-Gauss…) are fast converging techniques but they require the knowledge of an initial set of parameters that is close enough to the optimal set. This is an intrinsic limitation that I will not solve here. In addition, in the case of the spatial distribution of the fields inside the nanoslit, gradient-based methods require calculating the nearfield at each step of the optimization which can be handled using FDTD. This step would completely limit the interest of a gradient-based method unless it can be done in another faster way. This is the point I will address in this Chapter.

By utilizing an extended Jones matrix formalism, I will show that it is possible to quantitatively relate the excitation to the fields inside the nanoslit for both the transverse and longitudinal modes providing valuable insights into their behavior in the optical nearfield. The nanoslit studied and analyzed will be based on the specific dimensions and materials of the nanoslit studied in the simulation mentioned in Chapter 3. The optimization method will allow quickly exploring and calculating any physical quantity related to the electromagnetic properties of the light in the nanoslit for any polarization state and any wavelength of the incident wave. In the longer term, the method developed in this Chapter would provide a fast mapping of the polarization-dependent nearfield properties of various resonators, which could be used in combination with GA or deep learning algorithms.

4.2 Nearfield to far-field Connection

In classical optics, when studying the behavior of light interacting with objects or surfaces, there are typically two distinct regions: the nearfield and the far-field. The "nearfield" refers to the space close to an object or surface where the distance between the object and the observer is comparable to or less than the wavelength of light.

In order to address the behavior of polarized light in the vicinity of objects and surfaces, diverse methods aimed at extending the principles and applications of polarization theory to the nearfield region have been developed.[66,67] The limitation that requires the development of "polarization principles" relates to the behavior of polarized light in the nearfield region of objects and surfaces. In classical optics, the behavior of light is typically described by scalar wave equations that do not fully account for the polarization state of light and its interactions with materials in the nearfield. However, when light interacts with objects or surfaces at distances comparable to or smaller than the wavelength of light (i.e., in the nearfield region), traditional scalar wave equations are no longer sufficient to fully understand and model the complex polarization effects that occur. As a result, the nearfield requires alternative methods, such as those introduced by F. Nori[68], to accurately account for polarization phenomena, especially unconventional states such as spin angular momentum (AM) and orbital AM.

Nanoantennas can support different resonant modes according to the structure geometry and material properties which can be excited depending on the polarization state of the incident field. In particular, the nanoslits support two modes as evidenced by the simulation with very different polarization properties. In this part, I will present how the polarization properties of the electromagnetic fields in the nanoslit can be obtained for any incident polarization using an extended Jones formalism. I will now describe how I will relate the incident excitation fields to the polarization properties in the nearfield maps.

4.3 Resonant modes of the nanoslit

In the previous Chapters, I have investigated the resonant behavior of a nanoslit antenna using FDTD simulations. The nanoslit (Figure 43a), characterized by its sub-wavelength dimensions, exhibits intriguing dual-mode resonances when exposed to incident fields polarized at $\theta = 0°$ and $\theta = 90°$, corresponding to horizontal and vertical polarization, respectively. Figure 43b and Figure 43c recall the electric field amplitude distribution in the mid-plane of the nanoslit when the incident fields are polarized at $\theta = 0°$ and 90° corresponding to the longitudinal and transverse modes, respectively.

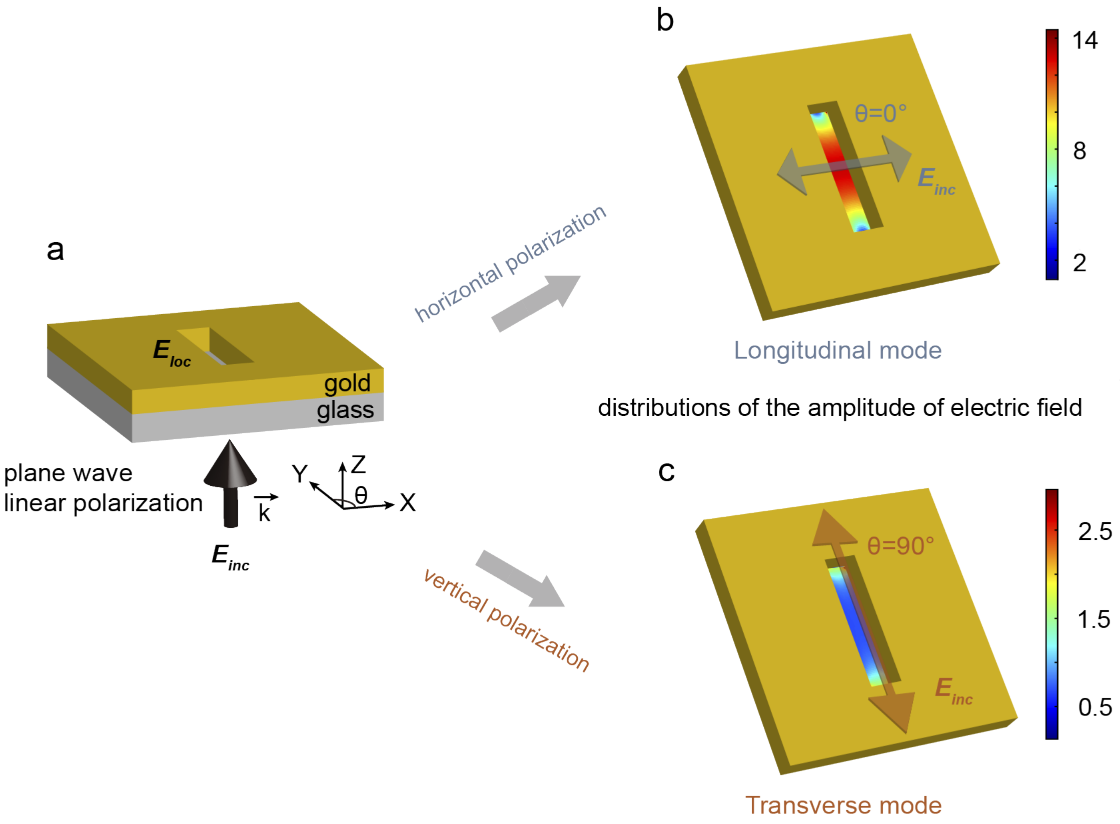

Figure 43 a) *3D representation of the rectangular nanoslit in a thin gold layer of 40 nm thick. The vector k represents the direction of propagation of the linearly polarized incident plane wave (E_{inc}), and θ, the angle of this polarization with respect to the nanoslit 's transverse axis (Ox). The field that has passed through the nanoslit is the local field (E_{loc}).* ***b)*** *Electric field amplitude distribution when the incident polarization angle is 0 degrees (longitudinal mode at 680nm), with strong electric field concentration at the nanogap center.* ***c)*** *Electric field amplitude distribution at a polarization angle of 90 degrees (transverse mode at 558nm), where the electric field is focused at both ends of the short edge of the nanogap, with relatively weaker regions.*

Our primary focus is to characterize the amplitude and phase response of the two resonant modes in the nanoslit. The amplitude reflects the intensity of the electromagnetic field, while the phase describes the temporal and spatial orientation of the oscillating field components. By investigating these key parameters, I am aiming at unravelling the underlying physics governing the interaction of light with the nanoslit structure.

Figure 44a and Figure 44b shows detailed visual representations of the amplitude and phase information at the center of nanoslit for the longitudinal and transverse resonant modes of nanoslit, respectively. The horizontal axis represents the wavelength, spanning from 400nm to 1000nm. On the left side of the vertical axis, we observe the normalized amplitude, calculated as the ratio of the amplitude at the center of nanoslit to the standard amplitude of the incident electric field. The right side of the vertical axis displays the phase information subtracted from the phase of the incident field, ranging from -90 degrees to 90 degrees. The solid line represents the amplitude, while the dashed line depicts the phase. Figure 44a presents the amplitude and phase data for the electric field in the nanoslit for incident light polarized along short side of nanoslit. It can observe a typical resonant behavior of the field inside the nanoslit with a maximum of amplitude at 680 nm associated with a field enhancement of 18, a full width at half maximum of 128nm (from 627nm to 755nm) and a phase crossing zero near resonance. In the following, I will call this resonance ‘longitudinal mode’. Figure 44b presents the amplitude and phase data for the electric field in the nanoslit for incident light polarized along long side of nanoslit. It can also observe a typical resonant behavior of the field inside the nanoslit with a maximum of amplitude at 558 nm associated with a field enhancement of 0.85, a full width at half maximum more than 447 nm (from 400nm to 847nm) and a phase of -41 degrees at resonance. In the following, I will call this resonance ‘transverse mode’. With the knowledge of the fields of the longitudinal and transverse modes only, I will now show how to calculate the total near field for any excitation polarization using the Jones formalism.

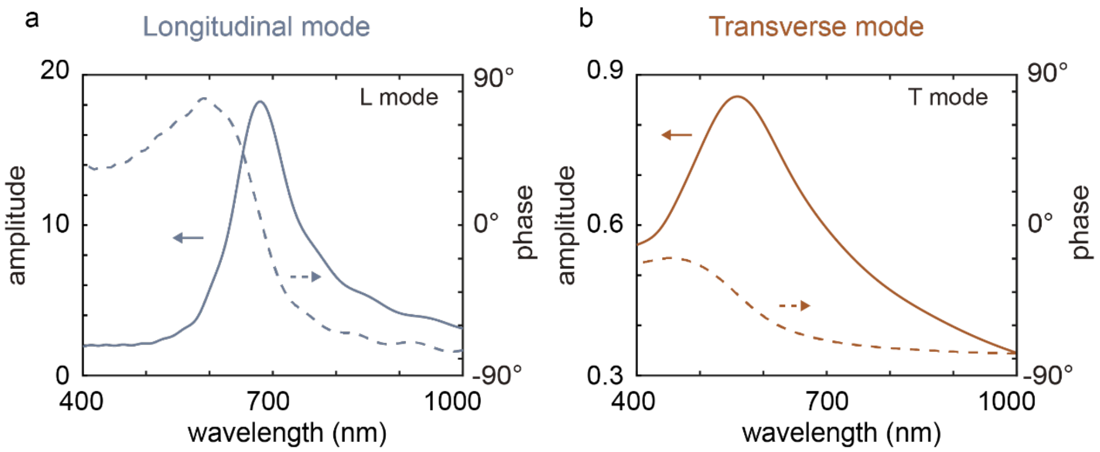

Figure 44 *Amplitude and phase of the* ***a)*** *longitudinal mode and* ***b)*** *transverse mode, where the horizontal axis represents the wavelength (400 nm to 1000 nm), the left vertical axis shows the normalized amplitude, and the right vertical axis shows the phase information (-90 degrees to 90 degrees). The solid line represents the amplitude, and the dashed line represents the phase. The longitudinal mode is shown in light blue and the transverse mode is shown in orange.*

4.3.1 Formalism

In Chapter 3, I have discussed the point-like dipole model, and the magnetic moment $\boldsymbol{m}$ of the dipole was obtained as $\boldsymbol{m} = \alpha^{mm}.\boldsymbol{H_0}$ (Eq. 37). The polarizability α^{mm} is a 3*3 diagonal tensor:

$$\alpha^{mm} = \begin{pmatrix} \alpha_{xx} & 0 & 0 \\ 0 & \alpha_{yy} & 0 \\ 0 & 0 & 0 \end{pmatrix} \qquad 44)$$

Combined with Eq. 37) in Chapter 3, this gives:

$$\boldsymbol{m} = pl_{H,L} * \boldsymbol{m_L} + pl_{H,T} * \boldsymbol{m_T} \qquad 45)$$

Where:

pl_L and pl_T are the amplitudes of the incident magnetic field polarized in the longitudinal and transverse direction components (H_y and H_x). $\boldsymbol{m_L}$ and $\boldsymbol{m_T}$ are the magnetic moment vectors in the longitudinal and transverse components, where $\boldsymbol{m_L} = \begin{pmatrix} \alpha_{xx} \\ 0 \\ 0 \end{pmatrix}$ and $\boldsymbol{m_T} = \begin{pmatrix} 0 \\ \alpha_{yy} \\ 0 \end{pmatrix}$.

For a point-like dipole with moment $\boldsymbol{m}$, the total radiation field includes contributions from both the near and far fields, as we discussed in Chapter 3, and Eq. 38) and Eq. 39) have given the radiated magnetic field and the electric field contributions that are observed in the direction $\mathbf{n}$ at a distance r from the position of the dipole. All the operations involved in the calculation of the fields (rotational and dot product) are linear so the fields radiated and the derived quantities (chirality density, U_e…) can be calculated from the weighted superposition of the fields radiated by the longitudinal and transverse modes. The total electric and magnetic fields can be written:

$$\boldsymbol{E_{tot}} = pl_{E,L} * \boldsymbol{E_{loc,L}} + pl_{E,T} * \boldsymbol{E_{loc,T}} \quad 46)$$

$$\boldsymbol{B_{tot}} = pl_{H,L} * \boldsymbol{B_{loc,L}} + pl_{H,T} * \boldsymbol{B_{loc,T}} \quad 47)$$

The weighting $pl_{E,L}, pl_{E,T}, pl_{H,L}, pl_{H,T}$ are the component of the incident field. From this relationship, we can deduce that for any polarized input field, as long as we know the longitudinal and transverse modes of the local field of the electric-magnetic fields, we can get the total field in any point of the nanoslit.

I have described in Sections 2.2.2 and 2.2.3 of Chapter 2, how the Jones vector represents the amplitude and phase of the electric field components of the light, and the Jones matrix can be used to determine the polarization state of the incident field. Thus, we can easily obtain pl_L and pl_T by multiplying the incident fields $\boldsymbol{E}_{inc}$ and $\boldsymbol{H}_{inc}$ by the Jones matrix.

The electric field numerically calculated in the nanoslit may be decomposed into x and y coordinate systems set by the nanoslit. So, the Jones matrix $\boldsymbol{J}_E$ is given by:

$$\boldsymbol{J}_E = \begin{bmatrix} J_{E,xx} & J_{E,xy} \\ J_{E,yx} & J_{E,yy} \end{bmatrix} \quad 48)$$

The 2x2 matrix $\boldsymbol{J}_E$ is defined by $\boldsymbol{E}_{loc} = \boldsymbol{J}_E \boldsymbol{E}_{inc}$ where $\boldsymbol{E}_{loc}$ and $\boldsymbol{E}_{inc}$ are the local and incident electric fields, respectively. The FDTD calculated Jones vector, $\boldsymbol{E}_{loc}$, is a 2x1 complex vector that describes the polarization state of the local field in the nanoslit. It must be noted that the local field contains the incident field as well. To define the Jones matrix $\boldsymbol{J}_E$, we need to know the specific values of the elements J_{xx}, J_{xy}, J_{yx}, and J_{yy}, which are determined by the properties of the nanoslit and its effect on the incident light's polarization state.

However, chiral density and ellipticity are not only related to electric field information only and we need to know the information about the magnetic field as well. This information was obtained through for the elements of $\boldsymbol{J}_H$ the equivalent of $\boldsymbol{J}_E$ but for the magnetic fields. The Jones matrix $\boldsymbol{J}_H$ is given by:

$$\boldsymbol{J}_H = \begin{bmatrix} J_{H,xx} & J_{H,xy} \\ J_{H,yx} & J_{H,yy} \end{bmatrix} \qquad 49)$$

Similarly, to $\boldsymbol{J}_E$, the 2x2 submatrix $\boldsymbol{J}_H$ is defined by $\boldsymbol{H}_{loc} = \boldsymbol{J}_H \boldsymbol{H}_{inc}$ with $\boldsymbol{H}_{loc}$ and $\boldsymbol{H}_{inc}$ the local and incident magnetic fields, respectively.

As discussed earlier, the longitudinal and transverse modes correspond to incident linear polarizations at θ=0° and θ=90°. The longitudinal mode is excited with a plane wave defined as $\boldsymbol{E}_{\boldsymbol{inc}} = \begin{pmatrix} 1 \\ 0 \end{pmatrix}$ and $\boldsymbol{H}_{\boldsymbol{inc}} = \begin{pmatrix} 0 \\ 1/Z_0 \end{pmatrix}$. According to the relationships between the local and incident fields, these two illumination conditions were sufficient for the determination of the elements of $\boldsymbol{J}_E$ and $\boldsymbol{J}_H$. So, I developed a 4x4 block diagonal Jones matrix $\boldsymbol{J}_{GEN}$ (Figure 45) that characterizes the nanoslit that contains the 2x2 $\boldsymbol{J}_E$, and the 2x2 $\boldsymbol{J}_H$ on its diagonal:

$$\boldsymbol{J}_{GEN} = \begin{bmatrix} \boldsymbol{J}_E & 0 \\ 0 & \boldsymbol{J}_H \end{bmatrix} \qquad 50)$$

The next step is to generalize this formalism to describe the 2D field repartition in the nanoslit as depicted in Figure 45.

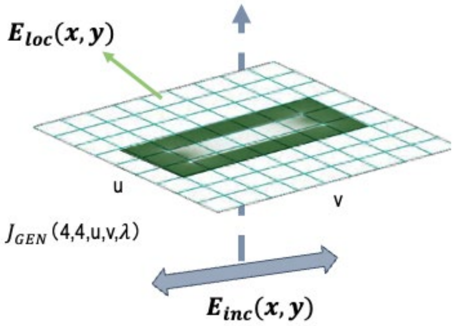

Figure 45 *Jones matrix in relation to incident field and local field. Decomposition of the electric fields on the (x,y) coordinates, the incident field and local field are divided into* $\boldsymbol{E}_{inc}(x,y)$ *and* $\boldsymbol{E}_{loc}(x,y)$. *The middle plane represents a plane of the optical system, the solid blue lines represent the grid. In the plane divided by the grid there is the coordinate system (u, v), and* $\boldsymbol{J}_{\boldsymbol{GEN}}$ *represents the matrix of the two sets of 2x2 Jones matrices containing the electric and magnetic fields in the plane, and it is frequency dependent.*

The electromagnetic field characteristics obtained by the FDTD simulation are shown in Figure 46. Figure 46a - Figure 46c shows the electric field enhancement, magnetic field enhancement and chirality density enhancement of the nanoslit at the resonance frequency (680 nm) with the polarization angle of the incident field lines at 0 degree. Figure 46d - Figure 46f shows the electric field enhancement, magnetic field enhancement and chirality density enhancement of the nanoslit at the resonance frequency (558 nm) with the polarization angle of the incident field lines at 90 degrees.

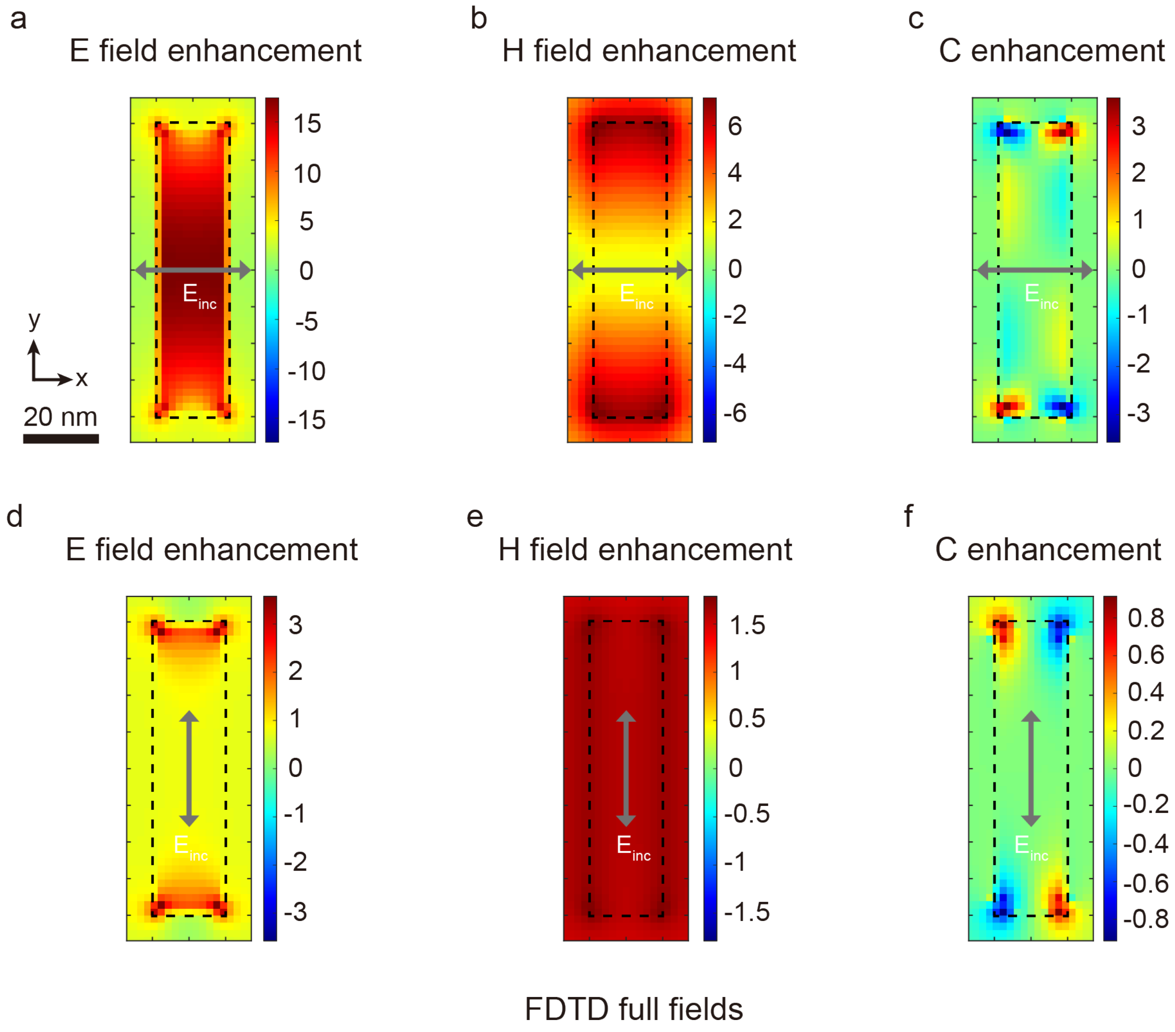

***Figure 46** The distribution of electromagnetic field enhancement and chirality density enhancement in the center plane of the nanoslit obtained from FDTD simulations. **a)** electric field enhancement, **b)** magnetic field enhancement, **c)** chirality density enhancement of the nanoslit at the resonance frequency (680 nm) with the polarization angle of the incident field lines at 0 degree. **d)** electric field enhancement, **e)** magnetic field enhancement, **f)** chirality density enhancement of the nanoslit at the resonance frequency (558 nm) with the polarization angle of the incident field lines at 90 degrees.*

With the knowledge of $\boldsymbol{J}_{GEN}$ it is possible to calculate any electromagnetic property at any incident polarization or wavelength in the same plane as the nanoslit. Comparisons with the FDTD simulation are made here. Figure 47 presents the distribution of electromagnetic field enhancements and chirality density enhancements in the center plane of the nanoslit obtained from $\boldsymbol{J}_{GEN}(4,4,u,v,\lambda)$ calculations. Figure 47a - Figure 47c shows the electric field enhancement, magnetic field enhancement and chirality density enhancement of the nanoslit at the resonance frequency (680 nm) with the polarization angle of the incident field lines at 0 degree. Figure 47d - Figure 47f shows the electric field enhancement, magnetic field enhancement and chirality density enhancement of the nanoslit at the resonance frequency (558 nm) with the polarization angle of the incident field lines at 90 degrees.

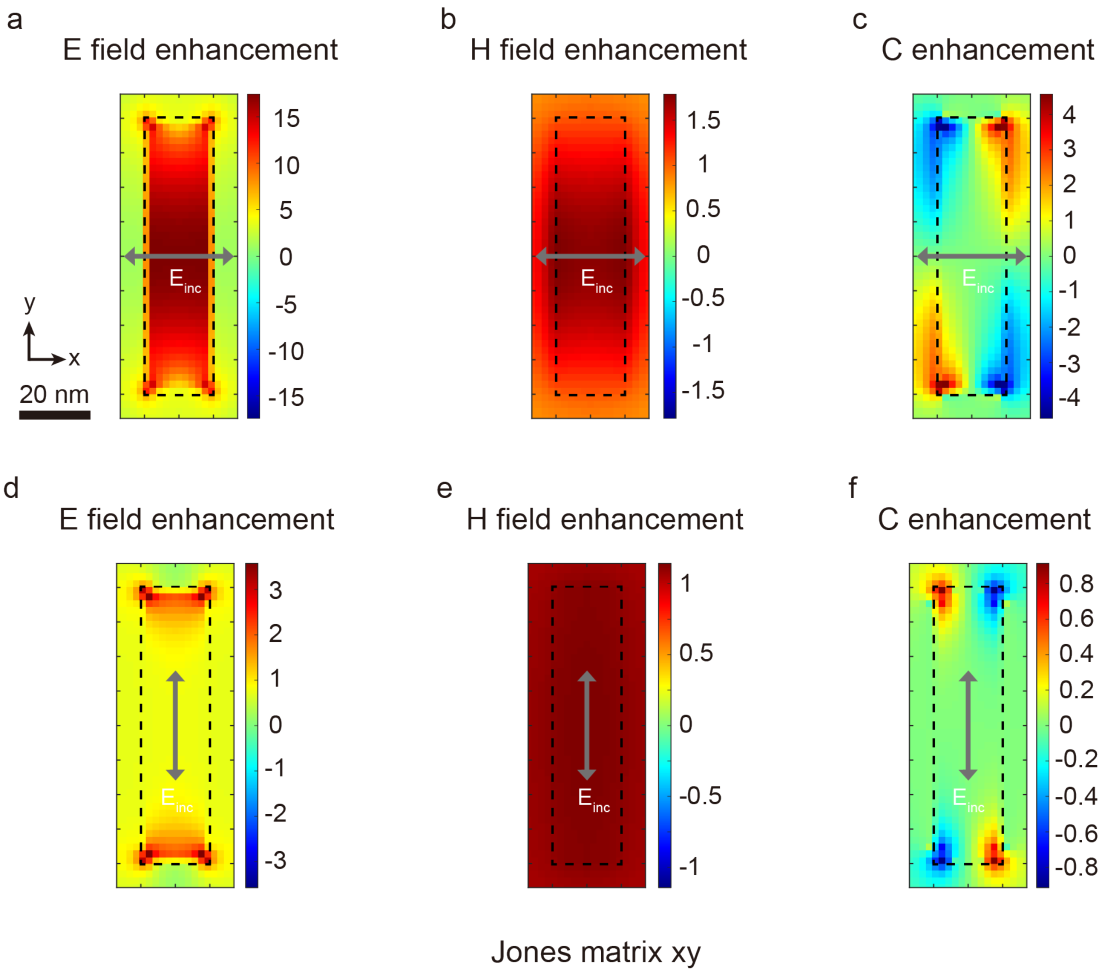

Figure 47 *The distribution of electromagnetic field enhancement and chirality density enhancement in the center plane of the nanoslit obtained from* $\boldsymbol{J}_{GEN}(4,4,u,v,\lambda)$ *calculations.* ***a)*** *electric field enhancement,* ***b)*** *magnetic field enhancement,* ***c)*** *chirality density enhancement of the nanoslit at the resonance frequency (680 nm) with the polarization angle of the incident field lines at 0 degree.* ***d)*** *electric field enhancement,* ***e)*** *magnetic field enhancement,* ***f)*** *chirality density enhancement of the nanoslit at the resonance frequency (558 nm) with the polarization angle of the incident field lines at 90 degrees.*

By comparing Figure 46 (FDTD calculated fields) and Figure 47 ($\boldsymbol{J}_{GEN}$ calculated fields) we see noticeable differences for the magnetic field enhancement distribution (Figure 46b, Figure 46e and Figure 47b, Figure 47e). For the chirality density, a large difference is produced when the incident field polarization angle is 0 degrees; however, it is almost the same when the incident field polarization angle is 90 degrees.

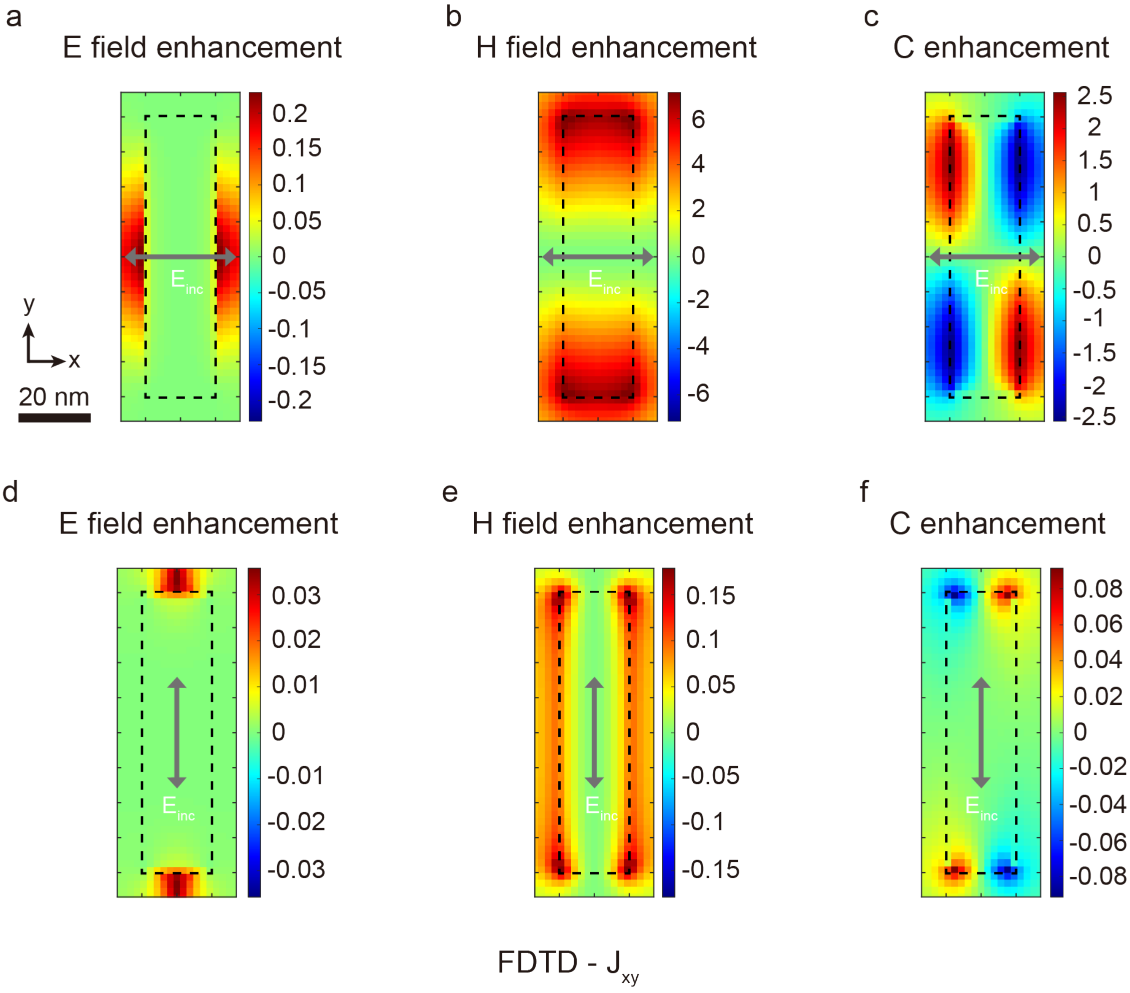

Figure 48 *The distribution of the specific differences of electromagnetic field enhancement and chirality density enhancement in the center plane of the nanoslit obtained from each grid point within this plane, where the differences are calculated by FDTD simulation full-field results minus the results calculated by* $\boldsymbol{J}_{GEN}(4,4,u,v,\lambda)$*.* ***a)*** *electric field enhancement,* ***b)*** *magnetic field enhancement,* ***c)*** *chirality density enhancement of the nanoslit at the resonance frequency (680 nm) with the polarization angle of the incident field lines at 0 degree.* ***d)*** *electric field enhancement,* ***e)*** *magnetic field enhancement,* ***f)*** *chirality density enhancement of the nanoslit at the resonance frequency (558 nm) with the polarization angle of the incident field lines at 90 degrees.*

Figure 48 illustrates the specific differences in these fields in each grid point by subtracting the fields of Figure 46 to those of Figure 47. We can see that for the electric field enhancement (Figure 48a and Figure 48d), the difference is of the order 1.3% and 1%, respectively. In contrast, Figure 48b and Figure 48e shows that for the magnetic field enhancement distribution, the differences can be of the order of 100% and 10%, respectively. As a result, for the chirality density (Figure 48c and Figure 48f), the largest differences amount to 83% and 10% depending on the incident polarization. Up to now, all the results in Figure 47 were based on only the two *xy* components of the fields while the FDTD simulation considered the three *xyz* components of the fields. The origin of these mismatches would be that the z-component of the fields was not taken into account which seems to be particularly critical for the longitudinal mode of the nanoslit. Therefore, it is necessary to extend the $\boldsymbol{J}_{GEN}$ matrix to three-dimensional components.

The electric incident field is expressed as $\boldsymbol{E_{inc}} = \begin{bmatrix} E_{inc,x} \\ E_{inc,y} \\ E_{inc,z} \end{bmatrix}$ with the third coordinate being equal to zero. The magnetic incident field is expressed as $\boldsymbol{H_{inc}} = \begin{bmatrix} H_{inc,x} \\ H_{inc,y} \\ H_{inc,z} \end{bmatrix}$. At the same time, $\boldsymbol{J}_E$ and $\boldsymbol{J_H}$ are expressed as $\boldsymbol{J}_E = \begin{bmatrix} J_{E,xx} & J_{E,xy} & J_{E,xz} \\ J_{E,yx} & J_{E,yy} & J_{E,yz} \\ J_{E,zx} & J_{E,zy} & J_{E,zz} \end{bmatrix}$ and $\boldsymbol{J_H} = \begin{bmatrix} J_{H,xx} & J_{H,xy} & J_{H,xz} \\ J_{H,yx} & J_{H,yy} & J_{H,yz} \\ J_{H,zx} & J_{H,zy} & J_{H,zz} \end{bmatrix}$, respectively.

The elements connecting the local fields to the z-components of the incident fields were set to zero because they could not be determined for normal incidence illumination. In the general case, this formalism would be able to handle oblique incidence illumination. However, the conditions used here emphasize the need of considering the z-component of the local fields even for normal incidence illumination. The Jones matrix $\boldsymbol{J}_{GEN}$ that characterizes the nanoslit is now 6*6 elements of $\boldsymbol{J}_E$ and $\boldsymbol{J}_H$. (Figure 49)

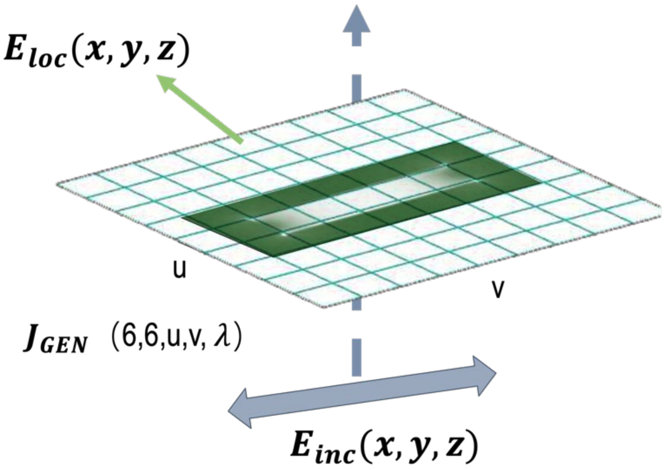

Figure 49 *Jones matrix in relation to incident field and local field. Decomposition of the electric fields on the (x,y,z) coordinates, the incident field and local field are divided into* $\boldsymbol{E}_{inc}(x,y,z)$ *and* $\boldsymbol{E}_{loc}(x,y,z)$. *The middle plane represents a plane of the optical system, the solid blue lines represent the grid. In the plane divided by the grid there is the coordinate system (u, v), and* $\boldsymbol{J}_{GEN}$ *represents the matrix of the two sets of 3*3 Jones matrices containing the electric and magnetic fields in the plane, and it is frequency dependent.*

Figure 50 presents the calculated electromagnetic field enhancement and chirality density enhancement distributions in the center plane of the nanoslit based on $\boldsymbol{J}_{GEN}(6,6,u,v,\lambda)$.

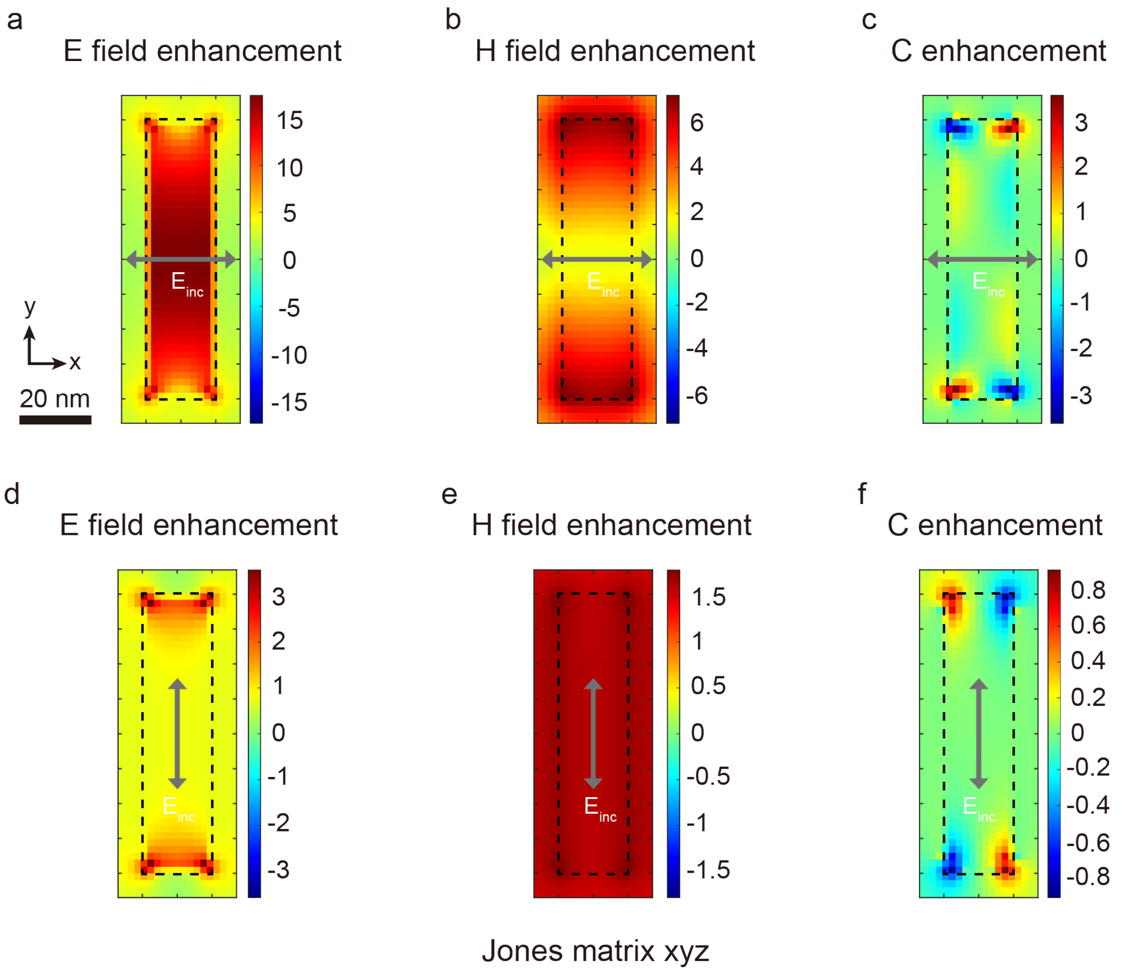

Figure 50 *The distribution of electromagnetic field enhancement and chirality density enhancement in the center plane of the nanoslit obtained from* $\boldsymbol{J}_{GEN}(6,6,u,v,\lambda)$ *calculations.* ***a)*** *electric field enhancement,* ***b)*** *magnetic field enhancement,* ***c)*** *chirality density enhancement of the nanoslit at the resonance frequency (680 nm) with the polarization angle of the incident field lines at 0 degree.* ***d)*** *electric field enhancement,* ***e)*** *magnetic field enhancement,* ***f)*** *chirality density enhancement of the nanoslit at the resonance frequency (558 nm) with the polarization angle of the incident field lines at 90 degrees.*

By comparing the results of Figure 50 with the FDTD full-wave simulation (Figure 46), it can be seen that the electromagnetic properties obtained by $\boldsymbol{J}_{GEN}$ calculations are in good agreement. Since each parameter calculated by $\boldsymbol{J}_{GEN}(6,6,u,v,\lambda)$ agrees with the results of the FDTD simulation, the results of the difference comparison will not be shown here. The method developed so far allows for characterizing the electromagnetic field properties of the light in the nanoslit for polarization angle at 0 and 90 degrees and any wavelength of the incident wave.

Based on our discussion of coordinate transformations, we can conjecture that by using the Jones matrix characterization method we can calculate any physical quantity related to the electromagnetic properties of light in nanoslits for any incident wave wavelength but more importantly for any polarization state (angle, ellipticity). This part of the discussion will be presented in the next subsection.

4.4 Comparison of Jones matrix and FDTD simulation

Based on a point-like magnetic dipole model, I have discussed that the total near-field for any arbitrary polarization should be obtained by calculating the weighted superposition of the longitudinal and transverse mode radiation fields (Figure 51a – Figure 51c). I will check now that these considerations can be extended to the fields inside the nanoslit. Although we developed the Jones matrix to reproduce the FDTD simulation results, the elements of the Jones matrix are still derived from the FDTD simulation. In the previous section, I have compared the nearfields calculated in the same incident polarization angles of 0 and 90 degrees, respectively, which does not bring much improvement in term of computation time. Figure 51 schematizes the processus that I want to develop and compares the chirality density calculated by FDTD and using the $\boldsymbol{J_{GEN}}$ based formalism with the knowledge of the spatial and spectral distributions of the nearfield inside the nanoslit for the longitudinal and transverse modes only.

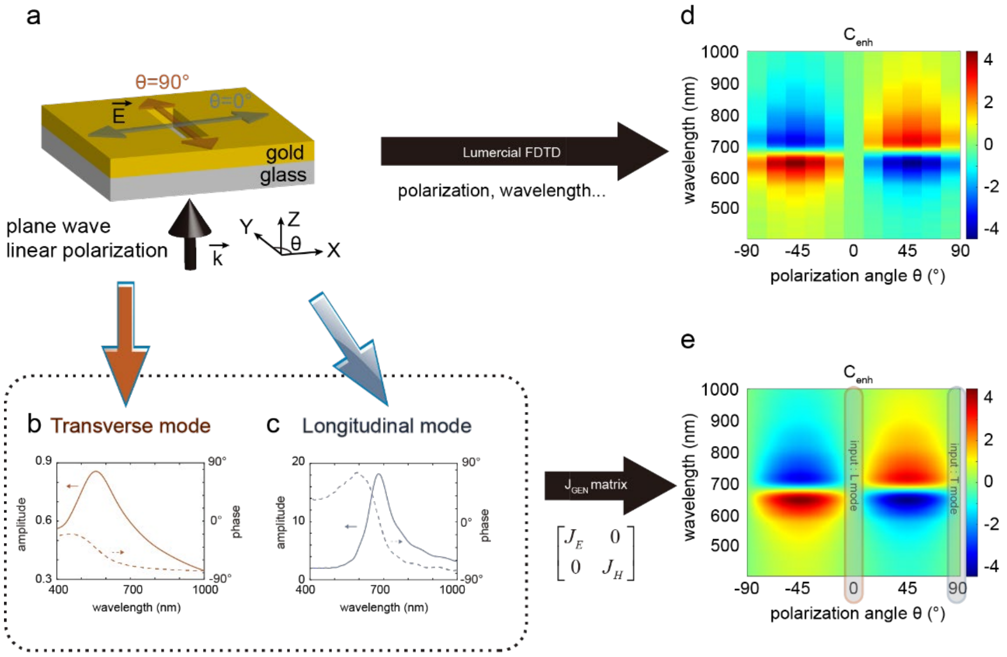

$$\begin{bmatrix} J_E & 0 \\ 0 & J_H \end{bmatrix}$$

Figure 51 a) *3D representation of the rectangular nanoslit in a thin gold layer of 40 nm. The vector k represents the direction of propagation of the linearly polarized incident plane wave, and θ, the angle of this polarization with respect to the nanoslit transverse axis (Ox).* ***b)*** *Transverse mode and* ***c)*** *longitudinal mode spectral responses of the amplitude and phase obtained for θ = 90° and 0°.* ***d)*** *Variations of C_{enh} as a function of the incident polarization angle θ and wavelength in the center of the nanoslit obtained from FDTD simulations (angle θ step by 15°). C_{enh} defined as $C/|C_{cpl}|$, with C_{cpl} the chirality density of a circularly polarized light, without the aperture, carrying the same power as the linearly polarized excitation impinging on the nanoslit.* ***e)*** *Variations of C_{enh} as a function of the incident polarization angle θ and wavelength calculated using the $\boldsymbol{J_{GEN}}$ matrix.*

Here I will present a full comparison of the fields averaged in the nanoslit calculated using the Jones matrix and FDTD. The comparison concerns U_e(Figure 52a, b), U_b((Figure 52c, d), chirality density (Figure 52e, f) and ellipticity (Figure 52g, h), which are several important physical quantities that can be obtained from the total electromagnetic near-field calculations.

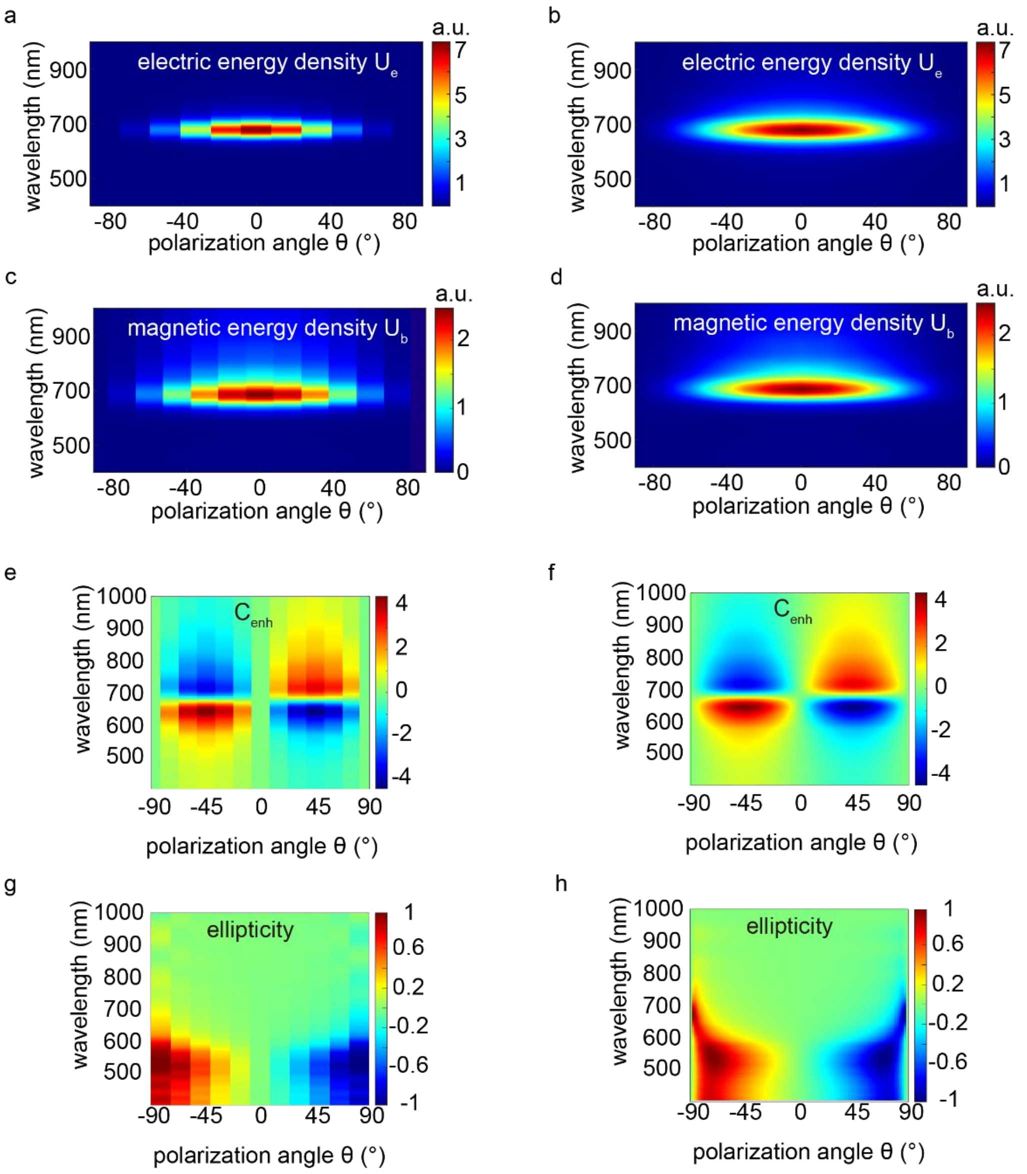

__Figure 52__ Spectral responses of the electric energy densities U_e simulated by __a)__ FDTD and calculated by __b)__ Jones matrix as a function of the incident polarization angle θ and wavelength respectively at point A (inset of Figure 20b) for nanoslit. Spectral responses of the magnetic energy densities U_b simulated by __c)__ FDTD and calculated by __d)__ Jones matrix as a function of the incident polarization angle θ and wavelength respectively at point B (inset of Figure 20b) for nanoslit. Spectral responses of the chirality density enhancement C_{enh} simulated by __e)__ FDTD and calculated by __f)__ Jones matrix as a function of the incident polarization angle θ and wavelength respectively at point A. Spectral responses of the ellipticity simulated by __g)__ FDTD and calculated by __h)__ Jones matrix as a function of the incident polarization angle θ and wavelength, respectively at point A.

The four plots on the right side of Figure 52 are the results of all parameters obtained by Jones matrix calculations as the wavelength and the polarization angle of the incident field are varied. The polarization angle in the Jones-based calculation is 0.1 degree, while the results obtained by the FDTD simulation were obtained for step of the polarization angle of 15 degrees. By comparing the FDTD simulation results with the field results obtained by the Jones matrix, we can see that the Jones matrix not only restores the field results of the FDTD at the calculated position, but also complements the other results at the full polarization angle of the nanoslit without any dead angle.

In terms of running time, FDTD required a total of 13 simulations, and the running time of each simulation varies depending on the mesh precision. For example, we use the same mesh precision as in Chapter 3: 1 nm, and the time to run a simulation is about 2 hours, so if we want to get the plots on the left side of Figure 52, it will take about 26 hours in total. In contrast, the Jones matrix requires any two simulations to obtain the $\boldsymbol{J}_{GEN}$ matrix, and the program itself runs in 0.02 seconds, so the total time to obtain the field results is approximately equal to the time to run two simulations: 4 hours.

The interest of having much better polarization angle resolution can be seen for the ellipticity (Figure 52g and Figure 52h). The Jones-based formalism reveals that pure circular polarization (ellipticity equal to -1 or 1) in the nanoslit could be obtained for polarization angles equal to plus or minus 71.6 degrees at a wavelength of 534nm and a polarization angle of plus or minus 87.9 degrees at a wavelength of 666nm, respectively (Figure 52h). These conditions would have been missed in the FDTD simulations.

4.4.1 Circular polarization state exploration

The point-like dipole model has given us an in-depth understanding of the origin and behavior, both angular and spectroscopic, of the chirality density inside the nanoslit. The ellipticity is a bit more difficult to understand. We can see in Figure 52g and Figure 52h that the maxima of ellipticity are obtained for wavelength and polarization angles much different from the ones yielding large chirality density. In addition, we can see that a finer polarization angle resolution (Figure 52h) reveals points of high ellipticity which were missed with the low polarization angle resolution obtainable with FDTD calculations (Figure 52g). This raises one question: are the particular points of high ellipticity real and were they missed by the FDTD calculations? To answer this question, we must then understand the origin of the large ellipticity values in the nanoslit to confirm/infirm the interest of the Jones matrix formalism that I have developed. This will be the objective of this Section.

From the previous discussion, it is clear that circular polarization can be formed by combining two orthogonal linearly polarized waves with a certain phase difference. For circular polarization, the amplitude and phase requirements for the longitudinal and transverse modes are as follows:

1. Amplitude: The amplitudes of the T and L mode components should be equal.

2. Phase Difference: The phase difference between the T and L mode components should be exactly 90 degrees.

The combination of these two equal amplitudes, orthogonal, linearly polarized waves with the specified phase difference results in circular polarization. Figure 44 presented the amplitudes and phase of the radiated electric field in the center of the nanoslit for excitation of the longitudinal and transverse modes only.

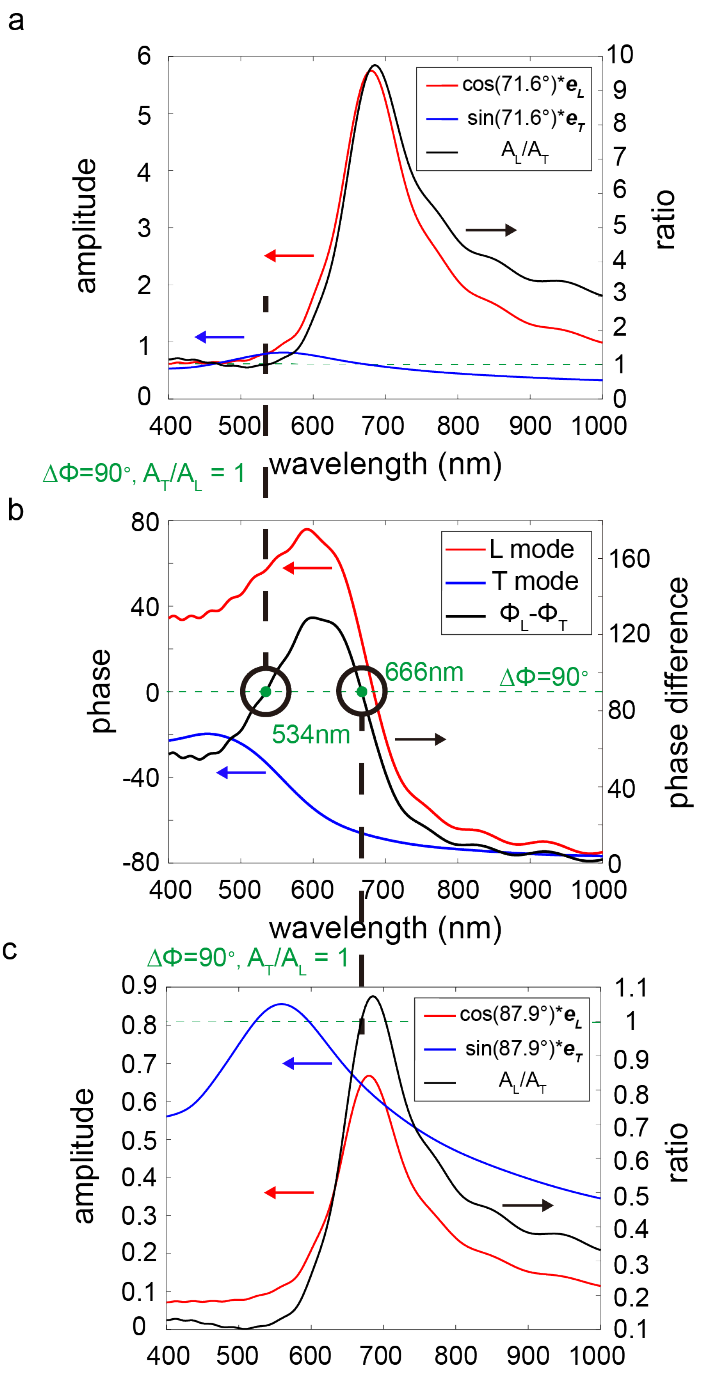

Figure 53 a) *the amplitude of the T and L modes (red and blue solid lines, referenced to the left axis) and the ratio of the amplitude of the T and L modes (black solid line, referenced to the right axis) as a function of frequency for the two modes, respectively, when the angle of polarization of the incident field is 71.6 degrees.* ***b)*** *the phase information of the T and L modes (blue and red solid lines, left axis) and the curves of the phase difference of the T and L mode phases (black solid line, right axis) versus frequency.* ***c)*** *the amplitude of the T and L modes (red and blue solid lines, referenced to the left axis) and the ratio of the amplitude of the T and L modes (black solid line, referenced to the right axis) as a function of frequency for the two modes, respectively, when the angle of polarization of the incident field is 87.9 degrees.*

Figure 53b shows the phase information of the two modes (blue and red solid lines, left axis) and the curves of the phase difference between the two mode phases (black solid line, right axis) versus wavelength, as shown in Chapter 3. The green dashed line marks the reference when the phase difference is 90 degrees. It can be seen that there are two wavelength points at 534 nm and 666 nm exhibiting a phase difference of 90 degrees in Figure 53b.

To reproduce the effect of excitation by a linearly polarized light at an angle θ from the x axis, the amplitude of the longitudinal mode was multiplied by the cosine of θ and the amplitude of the transverse mode by the sine of θ. This effectively reproduces the excitation strength of the two modes. In particular, Figure 53a shows the amplitude of the two modes (red and blue solid lines, referenced to the left axis) and the ratio of the amplitude of the two modes (black solid line, referenced to the right axis) as a function of wavelength for the two modes, respectively, when the angle of polarization of the incident field is 71.6 °. The green dashed line marks the reference when the amplitudes of the two modes are equal (ratio equal to 1). Similarly, Figure 53c shows the curves of the amplitude and amplitude ratio of the two modes versus frequency when the angle of polarization of the incident field is 87.9 The two black vertical dotted lines show that at these two wavelengths (four if we consider negative polarization angles) the amplitude ratio are equal to 1 in the Figure 53a and Figure 53c plots while the phase differences are 90°. These points, correspond exactly to those observed in Figure 52h where values of ellipticity of +/-1 were obtained. We could note the wavelength 703 nm in Figure 53c where the amplitude ratio is also 1, but the phase difference in Figure 53b is 44°, so there is no incident linearly polarized wave that can induce a circular polarization through the excitation of the longitudinal and transverse modes at 703nm. It is clear here that the origin of the ellipticity inside the nanoslit lies in the coherent superposition of the fields radiated by the longitudinal and transverse modes. This supports the Jones based calculation as a fast calculation and accurate method to investigate the polarization properties of the light inside the nanoslit as a function of wavelength and polarization state of the excitation light. I will show now how the Jones based method can be used in optimization routines.

4.5 Optimization program

When comparing the results of the FDTD simulations with those computed using the Jones matrix under identical lighting conditions, the Jones matrix approach was chosen because it provides results that are consistent with the FDTD simulations while significantly speeding up the computational process. In addition, the use of the Jones matrix method revealed previously unnoticed details and insights that were not readily apparent from simulation alone, adding a valuable dimension to our analysis.

I will explain how an optimization procedure based on the Levenberg-Marquardt algorithm can be applied for the nanoslit (Figure 54). I will illustrate the optimization by maximizing the value of the chirality density inside the nanoslit and discuss the results obtained. The procedure could be used for searching any property of the field: specific superchiral field, circular polarization, intensity.... Three optimization parameters were then chosen, namely the polarization angle θ, the ellipticity δ, and the wavelength. The relation between the complex components of the Jones vector and the polarization angle and ellipticity were presented in Chapter 2 (Figure 2). Thus, we can define the polarization state of the incident field by these two input variables. The local field, on the other hand, can be related to the incident field by the generalized Jones matrix $\boldsymbol{J}_{GEN}$.

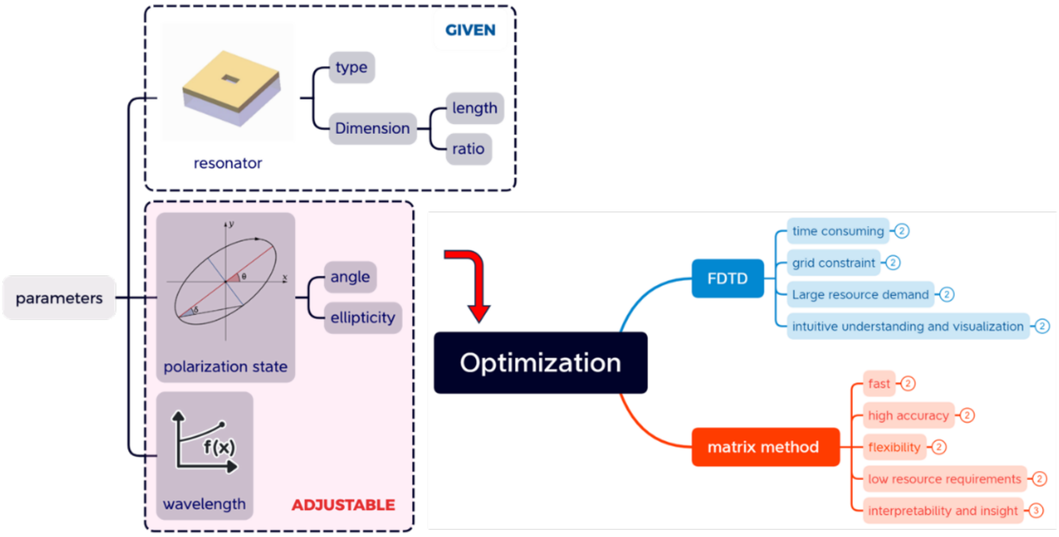

Figure 54 *Optimization parameters of the optimization algorithm, where the type and dimension of the nanoslit are fixed. Instead, the parameters that can be adjusted are related to the incident field: polarization state and wavelength. Polarization state parameters include polarization angle θ and ellipticity δ. The methods used to optimize the incident field are FDTD and Matrix methods. Each has its own characteristics.*

4.5.1 Logic diagram

In this subsection, I study into the logics underlying the optimization algorithm designed to maximize the chirality density, which is a crucial aspect in various scientific and engineering domains, such as plasmonic, nanophononics, and materials science. The optimization code based on the Levenberg-Marquardt algorithm provided by the lsqnonlin.m function in Matlab works by manipulating two input variables: the polarization angle (θ) and the ellipticity (δ). The algorithm iteratively adjusts these input variables to determine the optimal conditions for achieving the maximum chirality density in a step-by-step process (Figure 55).

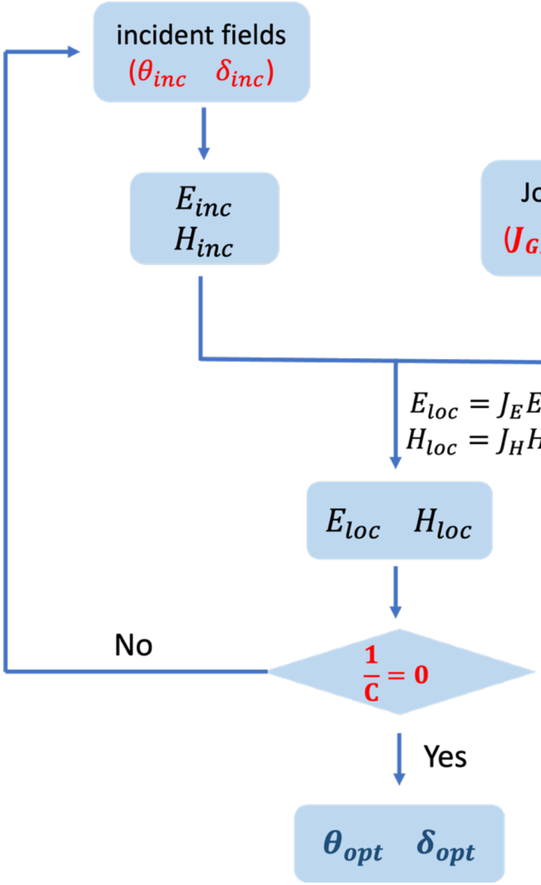

Figure 55 *Logic diagram of optimization code.* θ_{inc} *and* δ_{inc} *are the input values for the incident wave.* $\boldsymbol{J}_{GEN}$ *is the Jones matrix imported from nanoslit. C is the chirality density.* θ_{opt} *and* δ_{opt} *are the optimized results for the input values.*

Step 1: Obtaining the Jones matrix of the incident field. The first step of the optimization algorithm is to compute the Jones matrix, which characterizes the incident electromagnetic field. This has been discussed in the previous Sections of this Chapter.

Step 2: Deriving the local field. To complete this step, the algorithm multiplies the electric and magnetic components of the incident field by the Jones matrix characterizing the nanoslit.

Step 3: Chirality density calculation. With the electric and magnetic field components characterizing the local field, the algorithm can proceed to calculate the chirality density (Eq. 28) in Chapter 2).

Step 4: Optimization process. Optimization algorithms look for a minimum of an objective function. Here, to maximize the chirality density I have chosen $\frac{1}{|C|}$ as the objective function to minimize. The algorithm uses the least squares (function *lsqnonlin*) to adjust the input variables (θ and δ). The least squares method iteratively modifies these variables to approach the conditions that yield the highest chirality density. The process continues until the chirality density reaches its maximum possible value corresponding to the minimum of $\frac{1}{|C|}$. The value of $\frac{1}{|C|}$ was decided as minimum for two exit possibilities: $\frac{1}{|C|} < 10^{-7}$ or $\Delta\frac{1}{|C|} < 10^{-4}$ with Δ referring to the difference between two consecutive optimization steps. The first condition concerns value smaller than the accuracy on the calculated fields, the second the presence of a local minimum (horizontal tangent). We can see in Figure 52f and Figure 52h, that many local minima may be present. I have added a first parametric mapping of the values of $\frac{1}{|C|}$ for θ (from -90° to 90° in steps of 0.01°) and δ (from -45° to 45° in steps of 0.01°) to estimate a good starting point for the LM algorithm. The initial mapping adds 34 seconds to the optimization procedure. When comparing the results of the FDTD simulations with those computed using the Jones matrix under identical lighting conditions, the Jones matrix approach was chosen because it provides results that are consistent with the FDTD simulations while significantly speeding up the computational process. In addition, the use of the Jones matrix method revealed previously unnoticed details and insights that were not readily apparent from simulation alone, adding a valuable dimension to our analysis.

When comparing the results of the FDTD simulations with those computed using the Jones matrix under identical lighting conditions, the Jones matrix approach was chosen because it provides results that are consistent with the FDTD simulations while significantly speeding up the computational process. In addition, the use of the Jones matrix method revealed previously unnoticed details and insights that were not readily apparent from simulation alone, adding a valuable dimension to our analysis.

I will explain how an optimization procedure based on the Levenberg-Marquardt algorithm can be applied for the nanoslit (Figure 54). I will illustrate the optimization by maximizing the value of the chirality density inside the nanoslit and discuss the results obtained. The procedure could be used for searching any property of the field: specific superchiral field, circular polarization, intensity.... Three optimization parameters were then chosen, namely the polarization angle θ, the ellipticity δ, and the wavelength. The relation between the complex components of the Jones vector and the polarization angle and ellipticity were presented in Chapter 2 (Figure 2). Thus, we can define the polarization state of the incident field by these two input variables. The local field, on the other hand, can be related to the incident field by the generalized Jones matrix $\boldsymbol{J}_{GEN}$.

However, the difficulties associated with possible local minima is a general problem of optimization procedures, the initial mapping will not solve the case of different true minima like for the ellipticity and each problem will require different optimization procedures.

4.5.2 Optimization on chirality density

4.5.2.1 Maximum chirality density

Based on this optimization algorithm that I have set up; I am trying to find the illumination conditions that yield the maximum chirality density of the full band of visible light (~400nm-1000nm) anywhere in the central plane within the nanoslit.

In my optimization program, I need to set an optimization objective function to properly express my optimization goal. I want to find the largest chirality density value that occurs at any position in the entire plane within the full wavelength. So, at this point my objective function can be expressed as:

$$C_{max} = min\left(\frac{1}{|C|}\right) \tag*{51)}$$

Figure 56 shows the optimization results for the maximum value of the chirality density obtained after running the program. We found the maximum chirality density value of 8.34 at the corners within the nanoslit at a wavelength equal to 700nm. The input variables to obtain this maximum chirality density are: θ_{opt} equal to ±8.6 degrees and δ_{opt} equal to ±22.97 degrees. The running time of the optimization procedure is related to the position of the input variables, and after a series of trials, the shortest optimization time recorded was 48.9 seconds.

polarization angle $\theta = \pm 8.6°$

ellipticity angle $\delta = \pm 22.97°$

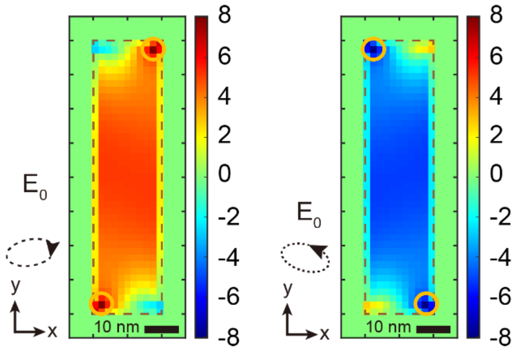

Maximum C : 8.34 in the corner @ 700nm

Minimum optimization time : 48.9 Sec

Figure 56 *The chirality density maximum corresponds to the chirality density field distribution in the nanoslit center plane. The positive and negative signs of the input variables determine the left and right chiral signs of the chirality density. The shape of E_0 shows these two opposite elliptically polarized incident waves. The positions of the chirality density maxima lie on a pair of diagonals in the mid-plane.*

4.5.2.2 Maximum chirality density averaged in center plane

I have found the maximum chirality density achieved by nanoslit in the full frequency band based on a pair of special elliptically polarized incident wave. However, in this case, we can see that the chirality density is maximized only in the corners, but the magnitude of the chirality density in the whole plane is not kept very high and there is a small portion of chiral near field of opposite sign at the same time. Based on our desire to imagine a probe experiment for chiral molecules, which will be Brownian motion inside the nanoslit, we would prefer that the average chiral field in the nanoslit be homogeneous and maximal. So, I replaced my optimization objective with maximum average chirality density in the middle plane.

At this point my objective function can be expressed as:

$$< C_{xy} >= \frac{1}{n}\sum_{loc}(C) \qquad 52)$$

Where: $< C_{xy} >$ is the chirality density averaged over the xy plane at the middle plane of the nanoslit. The number n corresponds to the number of mesh points in the middle plane of the nanoslit.

Figure 57 shows the optimization results for the maximum average chirality density in the middle plane. I find the maximum average chirality density value of 5.65 in the middle plane within the nanoslit at a wavelength equal to 678nm. The input variables to obtain this maximum chirality density are: θ_{opt} equal to $\mp$42.7 degrees and δ_{opt} equal to ±40.99 degrees. The shortest optimization time recorded was 272 seconds after a series of mapping. In this figure, we can see that in the middle plane of the nanoslit we have a homogeneous and single-signed chiral near-field, and that approximately the closer to the center of the nanoslit, the greater the chirality density.

polarization angle $\theta = \mp 42.7°$

ellipticity angle $\delta = \pm 40.99°$

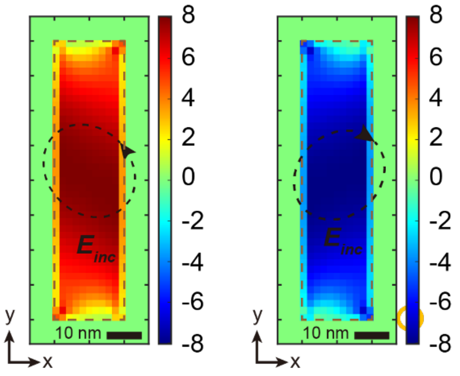

$< C_{xy} >= 5.65$ @ 678nm

Minimum optimization time : 272 Sec

Figure 57 *The maximum average chirality density corresponds to the chirality density field distribution in the whole center plane of nanoslit. The positive and negative signs of the input variables determine the left and right chiral signs of the chirality density. The shape of E_0 shows these two opposite elliptically polarized incident waves.*

In addition, we found that the incident field for which we obtained the average chirality density maximum was closer to circular polarization, even though it was elliptically polarized. This result is in line with the observations made in Chapter 3, where we found that the chiral field was very uniform and strong when we set the incident field to be circularly polarized. So, is the chiral near field created by this particular elliptically polarized incident field stronger or is it circularly polarized? Here we have compared these two incident field situations (Figure 58).

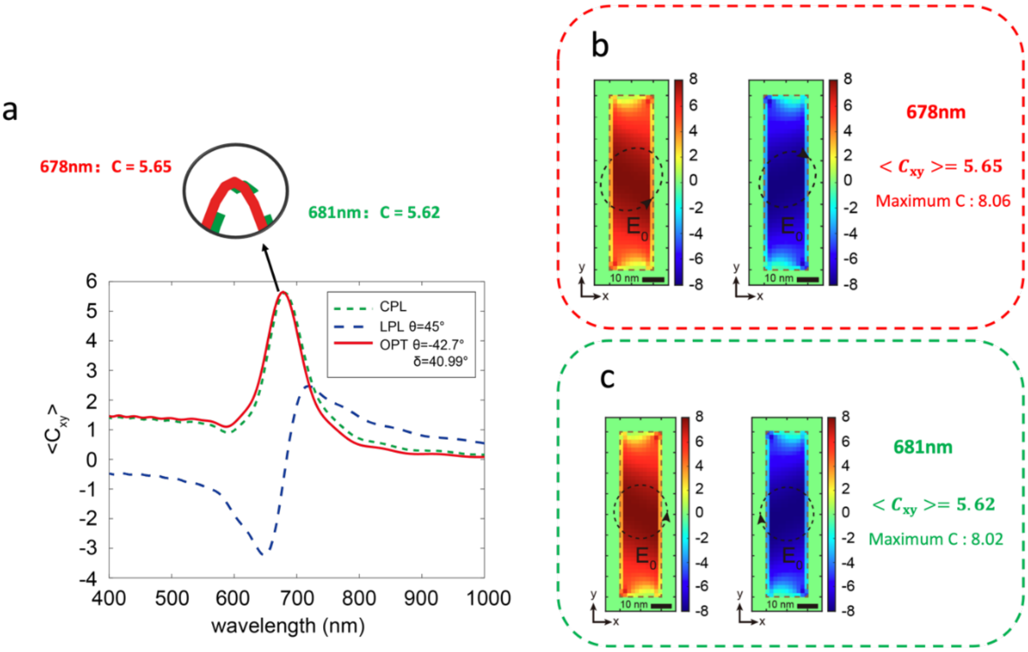

Figure 58 *The maximum average chiral field distribution optimized by the optimization procedure in the nanoslit center plane versus the chiral field distribution when the incident field is circularly polarized.* ***a)*** *The profile of the plane-averaged chirality density versus frequency for the incident field with the following: line polarization angle of 45 degrees (LPL), circular polarization (CPL), and elliptical polarization obtained by optimization (OPT).* ***b)*** *Elliptically polarized and* ***c)*** *circularly polarized incident fields generate a chiral field distribution in the center plane of the nanoslit.*

Figure 58a shows the results of the chirality density versus wavelength already shown in Chapter 3, when the incident field is linearly polarized at 45° (blue dashed line) and circularly polarized (green dashed line), respectively. They are not described here again. The chirality density versus wavelength for the best elliptical polarization obtained after optimization (red solid line) is also shown. The inset presents the values near the maximum value. In this case, the maximum average chirality density value obtained by the optimization (5.65 @678nm) is only slightly larger than the average chirality density obtained for circularly polarized incident light (5.62 @681nm). Figure 58b and Figure 58c shows the chiral field distribution in the middle plane when the incident field is elliptically and circularly polarized, respectively. It can be seen that they both display a homogeneous and single signed chiral field in the nanoslit. If we look for the maximum of chiral points in each case, we can find 8.06 in Figure 58b and 8.02 in Figure 58c, respectively.

With the above comparisons, we have sufficiently demonstrated that the optimization algorithm not only greatly outperforms the FDTD simulation in terms of speed in exploring the performance of the same nanostructures, but also reveals special results that we would not have known directly from the simulation.

4.6 Conclusion

In conclusion, I have demonstrated that by using the Jones matrix-based method, we can quickly calculate any physical quantity related to the electromagnetic properties of light in the nanoslit for any polarization state and any wavelength of the incident wave. Furthermore, we have shown that for the chirality density and ellipticity in the nanoslit, the polarization state inside the nanoslit is well expressed by the Jones matrix, and the results are in complete agreement with the FDTD simulation results. Finally, we have demonstrated that by combining the Jones matrix-based method with the optimization algorithm, we can quickly find the results of the maximum chirality density in the middle plane of the nanoslit and find the incident wave conditions to achieve the maximum chirality density. This work provides a way to characterize any nanoantenna and quickly characterize any physical quantity related to the electromagnetic properties of light. The desired excitation condition can be quickly obtained by changing the optimization target.

Chapter 5 General Conclusions and Perspectives

The focus of my Ph.D. thesis is on the enhancement of interactions between light and "chiral matter" using plasmonic nano-resonators, all with the primary goal of detecting and comprehensively studying chiral molecules. Within this overarching goal, my Ph.D. work can be distilled into two distinct areas of investigation. First, I set out to propose and test the chiral properties of the electromagnetic fields inside nanoslits, laying the theoretical groundwork for their importance in this context. Next, I delved into the intricacies of the chiral properties of the electromagnetic fields inside the nanoslits through rigorous mathematical analysis, gaining a deeper understanding of their behavior and capabilities.

The study of the chiral nearfield of nanoslits is concentrated in Chapter 3. In summary, the results show that nanoslits generate strong and uniform chiral nearfields, quantified by chirality density or ellipticity, as demonstrated by the FDTD simulations. This chiral effect is observed with linear polarization excitation, and its sign can be externally controlled by adjusting the polarization angle and wavelength, providing flexibility in the accessible spectral range (650-750 nm). The phenomenon can be explained by the radiation of a magnetic dipole and suggests that the uniformity of this effect is related to the enhancement of a uniform electric field within the nanoslit. Importantly, this chiral effect remains robust to shape variations, further enhancing its attractiveness for practical applications.

The analysis and study of the chiral nearfield of nanoslits is concentrated in Chapter 4. In summary, the conclusion highlights three key points. First, it is shown that chirality density can be optimized by a precise control of the polarization and wavelength. Second, a novel methodology has been developed that combines FDTD simulations, focusing on the nearfield for the eigenpolarization, with the Jones-based formalism. This innovative approach allows fast computations for any wavelength and polarization (reducing the computation time from hours to seconds) and opens new avenues for optimization. Finally, optimization is applied using a classical optimization method, the Levenberg-Marquardt method, to further improve the understanding and control of chiral near-fields in nanoslits.

Starting in Chapter 4, the prospects include the creation of a library of different shapes using FDTD simulations, the implementation of genetic algorithms for optimization, and the integration of deep learning approaches for further advances in the understanding and control of chiral nearfields. Together, these perspectives represent the potential for further research and practical applications in the field of chiral molecule detection and nanophotonics. The rapid verification of the chiral field properties of nanoslit at different frequencies and polarization states will be an important part of the future once we have established a complete and mature experimental detection equipment. In addition, the exploration of different resonators for chiral molecule detection will be an open topic for optimization.

With regard to future prospects, I contributed to the experimental domain by optimizing the fabrication and calibrating a preliminary experimental setup, a critical start towards the practical realization of highly sensitive chiral molecule detection. With respect to fabrication, as I have shown in Chapter 3, it is based on the previous methods by electron lithography and dry etching in the clean room and annealing, which smoothed the boundary of nanoslits to some extent. For the preliminary experimental part, which I did not present in my thesis due to its complexity and long lead time, I did some calibration and validation work that will provide guidance to later Ph.D. students.

The research results from Chapters 3 and 4 provide several promising perspectives. From Chapter 3, the potential applications include coupling with emissive biomaterials, demonstrating circular dichroism and absorption like LHCII (Figure 59), demonstrating fluorescence through nanoslits (Figure 60). LHCII presents a strong absorption band in the red part of the visible spectrum exhibiting circular dichroism. The fluorescence signal emitted in liquid is sufficient to verify that the signal can still be detected through nanoslits. These measurements are encouraging with the aim of studying the electromagnetic coupling of chiral molecules to plasmonic resonators. The measurement system would obtain the CD properties of chiral molecules by monitoring their PL intensity, technique referred to the literature as Fluorescence Detected Circular Dichroism (FDCD) (Figure 61).

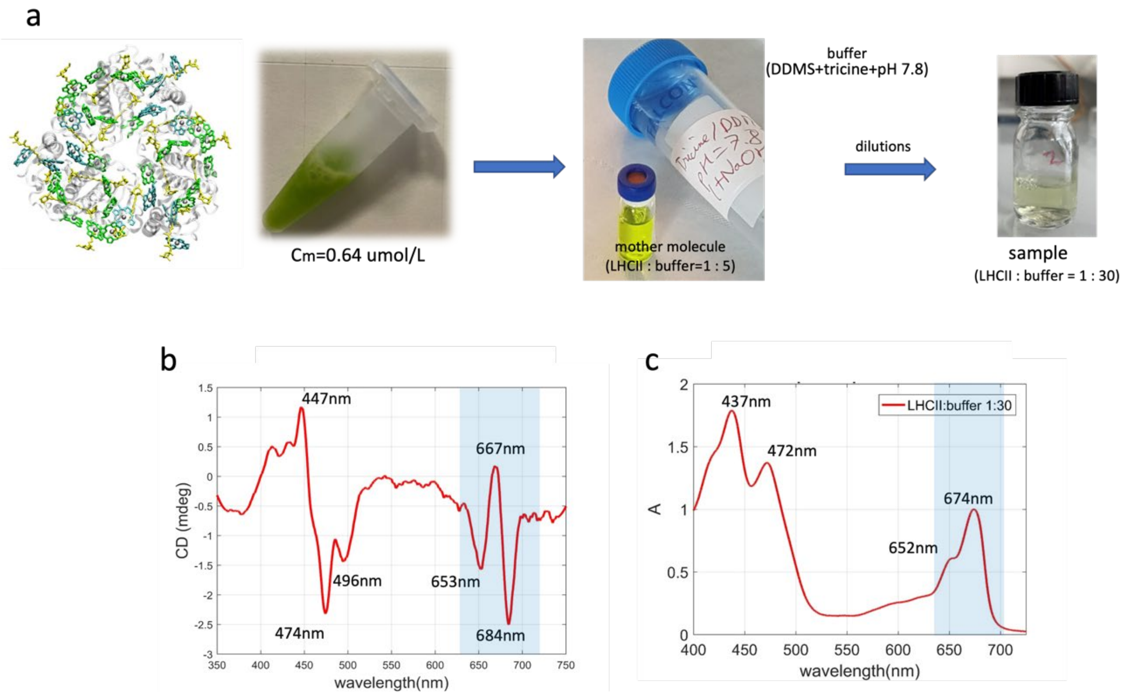

Figure 59 b) *CD and **c)** Absorption spectra of LHCII solubilized in **a)** 0.03% DDM with tricine buffer (PH=7.8). Measurements were performed in a standard glass cell of 1-cm optical path length using a Jasco spectropolarimeter.*

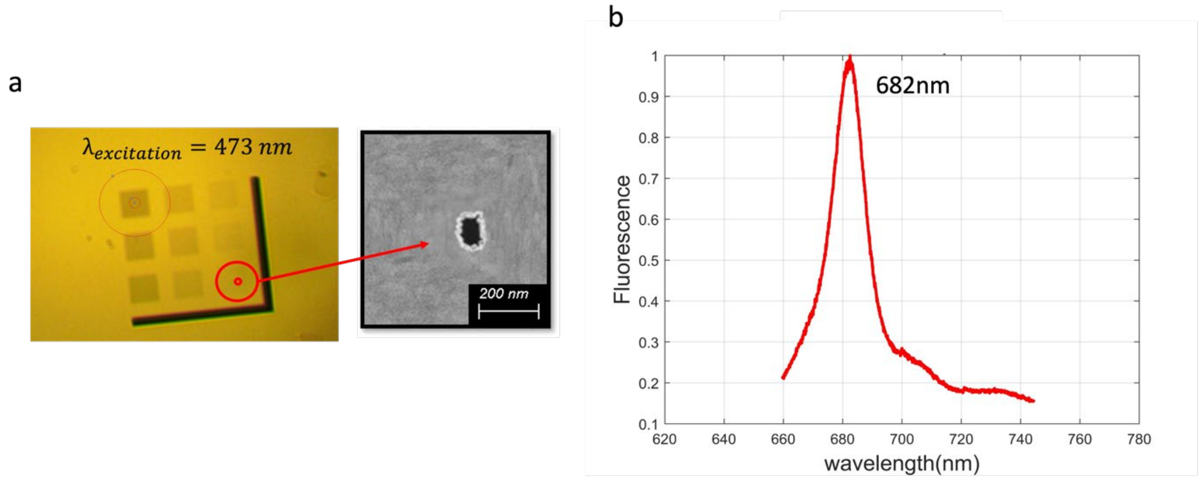

Figure 60 *The fluorescence emission measurement of the LHCII through **a)** nanoslits fabcrited by e-beam lithography. The emission under unpolarized excitation at 473 nm. **b)** Fluorescence spectra of LHCII obtained through c.a. fivenanoslits.*

In parallel, I have started exploring the possibility of measuring of FDCD on highly luminescent CdSe nanoplatelets functionalized with tartrate derivatives (collab. B. Abécassis, ENS Lyon) showing a strong CD near 530 nm (Figure 61c). The incident light was a laser at 532nm which polarization was modulated at 50kHz with a polarizer and a photo-elastic modulator (PEM). The detection was obtained with a photodiode and the signal was demodulated with a lock-in amplifier (EG&G 9210). A microscope objective (NA 0.42) has been placed at 90° from the excitation path and to collect the photoluminescence, and the light was then filtered by a high pass filter to eliminate any spurious signal of the excitation that might have been scattered. The PL was collected with a photomultiplier tube (PMT) and demoludated to obtain the FDCD signal (Figure 61d).

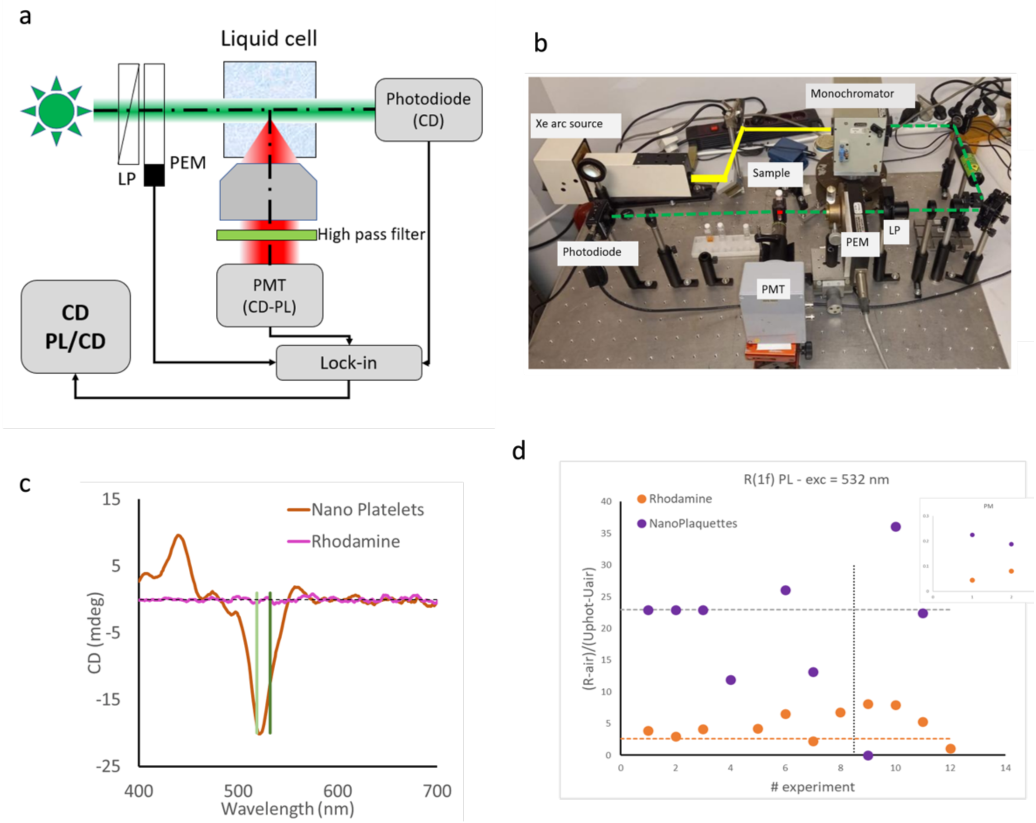

***Figure 61 a)** schematic and **b)** real of the experimental setup. **c)** CD measured on a JASCO polarimeter for rhodamine and functionalized nanoplatelets. **d)** Amplitude of the intensity modulated at 50 kHz measured on the PL signal. The insets show the PL in the cuvettes illuminated at 532 nm.*

This series of preliminary experiments demonstrate that chiral characterization at the molecular level can be achieved by detecting FDCD signals.

Through all interrelated components, my Ph.D. research has advanced our knowledge in the field of chiral matter-light interactions and made valuable contributions to the broader pursuit of high-sensitivity detection techniques.

Appendix

1. Convergence

For the reliability and usefulness of FDTD simulations, the discretization of space, i.e., the mesh size, plays a critical role. As the mesh is refined, the simulation approaches the exact solution of Maxwell's equations, reducing errors and inaccuracies. However, mesh refinement is computationally expensive and, moreover, under some mesh size no further gain may be obtained in the accuracy of the data extracted by reducing the mesh size. Convergence tests help to find a balance between accuracy and computational resources by monitoring the value of some physical quantity as a function of mesh size.

I will present below the convergence test that was performed for the nanoslits. The methodology involves a systematic investigation of simulation accuracy by varying at the mesh size at 1nm, 2nm, 4nm, 8nm, and 16nm. in identical nanoslits. The key parameter under investigation is the chirality density map in the middle plane of the nanoslit obtained (for an illumination at 20 nm with a linearly polarized light at 45° from the axis x. Obviously, the chirality density is an important parameter in this work, but it also contains the information about the complex vector elements of the electric and magnetic fields. The chirality density calculated for each mesh size n = 1, 2, 4, 8, 16 was interpolated on a grid m=1, 2, 4, 8, 16 and is noted C_{nm}. The convergence was tested by comparing the values of C_{nm} for two consecutive mesh sizes. For instance, the C_{nm} of the 2nm grid C_{22}, was interpolated on the 1nm grid yielding C_{21}. The values of C_{21} are then compared to those of C_{11} obtained for the chirality density calculated on the 1nm grid of calculations with a 1nm mesh size. For each point of the 2D map, the value $((C_{21}-C_{11})/C_{21})^2$ was calculated. The square root of the sum of all these values is noted ΔV1, which quantifies the difference in accuracy between the 2nm and 1nm FDTD grids. The same approach was applied iteratively to evaluate the accuracy differences between the 2nm and 4nm, 4nm and 8nm, and 8nm and 16nm grids, yielding ΔVn (n=2, 4, 8) values, as shown in Figure 62. As can be seen, the mesh of 1nm brought an improvement of 0.21% as compared to the 2nm mesh. and the 8nm mesh, brought an improvement of 5.55% with respect to the 16nm mesh. Reducing the mesh size in the FDTD simulation from 16nm to 1nm significantly increased the computation time, with run times ranging from 14 seconds to 1 hour 53 minutes, reflecting a trade-off between spatial resolution and computational efficiency. The choice of mesh size should be carefully balanced to meet simulation accuracy requirements while taking into account available computational resources. In my study, although 2nm is not very different from 1nm, I will base all subsequent FDTD simulation calculations on a 1nm mesh.

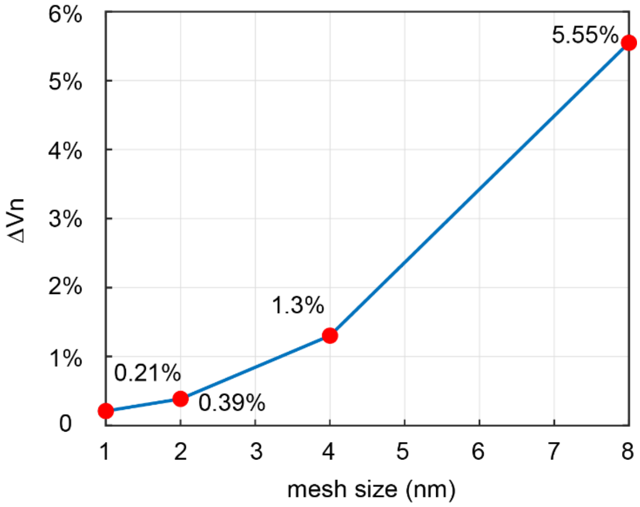

Figure 62 *FDTD convergence study. The x-axis indicates mesh size. The y-axis gives the relative difference of the values of the chirality density maps inside the nanoslit between the mesh size at the x-axis and the larger mesh size (see text).*

2. Spatial response of the chirality density in different planes

To visualize the uniformity of the chirality density within the nanoslit, three cross sections were selected: the xz plane when y is equal to 0 nm, the xy plane when z is equal to 20 nm and the yz plane when x is equal to 0 nm (see Figure 63). Figure 64 displays the distribution of chirality density for these three planes at 645 nm wavelength and -45° of polarization angle. The first important conclusion that can be drawn from Figure 64 is that the sign of the chirality density remains the same with the full volume of the nanoslit. A closer inspection of Figure 64a and Figure 64c show that the chirality density is stronger near interface between glass and air inside the nanoslit. In contrast, in Figure 64b and Figure 64c we see that the chirality density decreases near the ends of the nanoslit or near the open surface. These plots confirm that nanoslits allow generating rather homogeneous pure chiral light. Similar observations would be made at +45° but with the opposite sign of the chirality density.

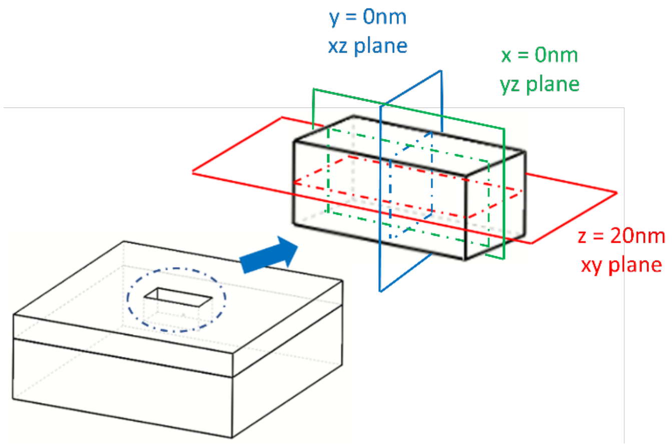

Figure 63 *Schematic representation of three cross sections of nanoslit.*

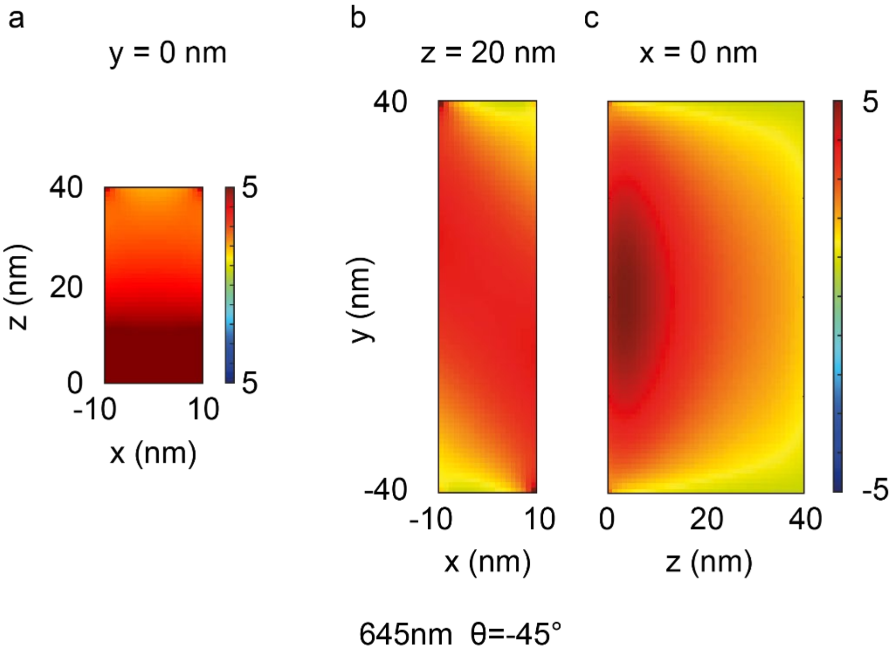

Figure 64 *Spatial distribution of the chirality density in **a)** the xz plane, **b)** the xy plane and **c)** the yz plane within the nanoslit, at the wavelength 645nm and for θ = -45°.*

Reference

---

1 Jack C., Karimullah A. S., Leyman R., Tullius R., Rotello V. M., Cooke G., Gadegaard N., Barron L. D., and Kadodwala M., Biomacromolecular Stereostructure Mediates Mode Hybridization in Chiral Plasmonic Nanostructures, *Nano Letters*, 16 (9), 5806-5814. (2016).

2 Hendry E., Carpy T., Johnston J. et al. Ultrasensitive detection and characterization of biomolecules using superchiral fields. *Nature Nanotech* 5, 783–787 (2010).

3 Jack C., Karimullah A., Tullius R. et al. Spatial control of chemical processes on nanostructures through nano-localized water heating. *Nat Commun* 7, 10946 (2016).

4 Zhao Y., Askarpour A., Sun L. et al. Chirality detection of enantiomers using twisted optical metamaterials. *Nat Commun* 8, 14180 (2017).

5 Proust J., Bonod N., Grand J., and Gallas B., Optical Monitoring of the Magnetoelectric Coupling in Individual Plasmonic Scatterers. *ACS Photonics*, *3* (9), 1581-1588. (2016).

6 Hyuk Yoo T. S., Berthelot J., Guida G., Demaille D., Garcia-Caurel E., Bonod N., and Gallas B., Circularly Polarized Images with Contrast Reversal Using Pseudochiral Metasurfaces. *ACS Photonics*, *5* (10), 4068-4073. (2018).

7 Barulin A, Roy P, Claude JB, Wenger J. Ultraviolet optical horn antennas for label-free detection of single proteins. *Nat Commun.* 5 13(1):1842. (2022).

8 Kelvin L., The Molecular Tactics of a Crystal. *Oxford, UK: Clarendon Press* (1894).

9 Blackmond DG. The Origin of Biological Homochirality. *Cold Spring Harb Perspect Biol.* 11(3): a032540 (2019).

10 Nicolas M., Beito B, Oliveira M., Martins M. T., Gallas B., Salmain M., Boujday S., Humblot V., Strategies for Antimicrobial Peptides Immobilization on Surfaces to Prevent Biofilm Growth on Biomedical Devices, *Antibiotics* 11, 13 (2022).

11 Winogradoff D., Li P.-Y., Joshi H., Quednau L., Maffeo C., Aksimentiev A., Chiral Systems Made from DNA. *Adv. Sci.* 8, 2003113 (2021).

12 Staszak K., Wieszczycka K., Marturano V., Tylkowski B., Lanthanides complexes – Chiral sensing of biomolecules, *Coordination Chemistry Reviews*, Vol. 397, 76-90, ISSN 0010-8545, (2019).

13 Venkataraman N., Magyar G., Lightfoot M., Montbach E., Khan A., Schneider T., Doane J.W., Green L. and Li Q. Thin flexible photosensitive cholesteric displays. *Journal of the Society for Information Display*, 17: 869-873. (2009).

---

14 Jones R. C., A New Calculus for the Treatment of Optical SystemsI. Description and Discussion of the Calculus, *J. Opt. Soc. Am.* 31, 488-493 (1941).

15 Arago J. D., F., *Mém. Inst.*, 1, 93–134, (1811).

16 Kahr B. and Arteaga O., Arago's. *Chem. Phys. Chem*, 13: 79-88. (2012).

17 Biot J. B., Phénomènes de polarisation successive, observés dans des fluides homogènes. *Bull. Soc. Philomath*, 190 (1815).

18 Leclercq F., Arago, Biot, and Fresnel Elucidate Circular Polarization, *Revue d'histoire des sciences*, vol. 66, no. 2, pp. 395-416. (2013).

19 Fresnel A. J., Plane waves and wave propagation. (2001).

20 Oliveira M. H., Miranda, J. A., Biot-Savart-like law in electrostatics, *Eur. J. Phys*. 22 31, (2001).

21 Pasteur L., Mémoire sur la relation qui peut exister entre la forme cristalline et la composition chimique, et sur la cause de la polarisation rotatoire. *C. R. Acad. Sci. Paris* 26,535–538 (1848).

22 Cameron R.P., Götte J.B., Barnett S.M., Yao A.M., Chirality and the angular momentum of light. *Phil.Trans.R.Soc. A.* 375: 20150433 (2017).

23 Snatzke G. Circular Dichroism and Optical Rotatory Dispersion — Principles and Application to the Investigation of the Stereochemistry of Natural Products. *Angew. Chem. Int.* Ed. Engl., 7: 14-25. (1968).

24 Vogel, Arthur I. Vogel's textbook of practical organic chemistry (5th ed.). *Harlow: Longman*. ISBN 978-0582462366. (1996).

25 Mohrig J. R.; Hammond, C. N.; Schatz, P. F. Techniques in Organic Chemistry (Third ed.). *W. H. Freeman and Company*. pp. 209–210. (2010).

26 Weast R. C., Handbook of Chemistry and Physics (55th ed.). *CRC Press*. (1974).

27 The Merck Index Online: Paclitaxel. *Royal Society of Chemistry*. Retrieved 30 June (2014).

28 Fasman G.D. Circular Dichroism and the Conformational Analysis of Biomolecules. *New York, USA: Plenum PublishingCorp*. (1996).

29 Hammes G.G. Spectroscopy for the Biological Sciences. *New York, USA: John Wiley & Sons, Inc*. (2005).

30 Pignataro M. H., Herrera M. G., Dodero V. I., Evaluation of Peptide/Protein Self-Assembly and Aggregation by Spectroscopic Methods. *Molecules*. 25. 4854. (2020).

31 Sharon M. K., Thomas J. J., Nicholas C. P., How to study proteins by circular dichroism, *BBA - Proteins and Proteomics,* Vol. 1751, 2, 119-139, (2005).

32 Tang Y.; Cohen A. E., Optical chirality and its interaction with matter. *Phys. Rev. Lett.* 104 (16), 163901. (2010).

33 Lipkin D. M., Existence of a new conservation law in electromagnetic theory. *Journal of Mathematical Physics*, 5 (5), 696-700. (1964).

34 Bliokh K. Y. and Nori F., Transverse and longitudinal angular momenta of light. *Physics Reports* 592: 1-38 (2015).

35 Yiqiao T and Cohen A. E., Enhanced enantioselectivity in excitation of chiral molecules by superchiral light, *Science*, 332, 333, (2011).

36 Coles M. M. and Andrews D. L., Chirality and angular momentum in optical radiation. *Phys. Rev. A*, 85, 063810, (2012).

37 Yoochan H., Yong-Min H., Dae S. Y., Jaemoon Y., Nanobiosensors Based on Localized Surface Plasmon Resonance for Biomarker Detection, *Journal of Nanomaterials*, vol. 2012, 759830, 13 pages, (2012).

38 Kelly K. L., Coronado E., Zhao L. L., and Schatz G. C., The Optical Properties of Metal Nanoparticles: The Influence of Size, Shape, and Dielectric Environment. *J. Phys. Chem. B* 107 (3), 668-677. (2003).

39 Ed. S. Enoch and N. Bonod, Plasmonics: from basics to advanced topics, *Springer Series in Optical Sciences,* vol. 167, Springer-Verlag Berlin Heidelberg. (2012).

40 Bhakta S. A., Evans E., Benavidez T. E., Garcia C. D., Protein adsorption onto nanomaterials for the development of biosensors and analytical devices: *A review, Analytica Chimica Acta*, Volume 872, Pages 7-25. (2015).

41 Špačková B., Wrobel P., Bocková M. and Homola J., Optical Biosensors Based on Plasmonic Nanostructures: A Review, in Proceedings of the *IEEE*, vol. 104, no. 12, pp. 2380-2408, Dec. (2016).

42 Rotello V. M., Cooke G., Lapthorn A., Kadodwala M., “Superchiral” Spectroscopy: Detection of Protein Higher Order Hierarchical Structure with Chiral Plasmonic Nanostructures, *J. Am. Chem. Soc*. 137, 8380−8383. (2015).

43 Arteaga O.; Sancho-Parramon, J.; Nichols, S.; Maoz, B. M.; Canillas, A.; Bosch, S.; Markovich, G.; Kahr, B. Relation between 2D/ 3D chirality and the appearance of chiroptical effects in real nanostructures. *Opt. Express 24*, 2242−2252, (2016).

44 Kneer L. M., Roller E.M., Besteiro L.V., Schreiber R., Govorov A. O., and Liedl T., Circular Dichroism of Chiral Molecules in DNA-Assembled Plasmonic Hotspots. *ACS Nano*, *12* (9), 9110-9115. (2018).

---

45 Guirado J.G., Svedendahl M., Puigdollers J., and Quidant R. Enantiomer-Selective Molecular Sensing Using Racemic Nanoplasmonic Arrays. *Nano Letters*, *18* (10), 6279-6285. (2018).

46 Jose G. G., Mikael S., Joaquim P., and Romain Q., Enhanced Chiral Sensing with Dielectric Nanoresonators, *Nano Letters*, *20* (1), 585-591. (2020).

47 Slocik J. M., Govorov A. O., and Naik R. R., Plasmonic Circular Dichroism of Peptide-Functionalized Gold Nanoparticles, *Nano Letters*, 11 (2), 701-705. (2011).

48 Maoz B.M., Chaikin Y., Tesler A.B., Elli O.B, Fan Z., Govorov A. O., Markovich G., Amplification of Chiroptical Activity of Chiral Biomolecules by Surface Plasmons, *Nano Letters*, 13 (3), 1203-1209. (2013).

49 Maxim L. N., Yin X., Schäferling M., Giessen H., and Weiss T., The Role of Plasmon-Generated Nearfields for Enhanced Circular Dichroism Spectroscopy, *ACS Photonics*, 3 (4), 578-583. (2016).

50 Gui L, Hentschel M, Defrance J, Krauth J, Weiss T, and Giessen H, Nonlinear Born-Kuhn Analog for Chiral Plasmonics, *ACS Photonics*, 6 (12), 3306-3314, (2019).

51 Both S., Schäferling M., Sterl F., Muljarov E. A., Giessen H., and Weiss T., Nanophotonic Chiral Sensing: How Does It Actually Work? *ACS Nano*, 16 (2), 2822-2832. (2022).

52 Schäferling M.; Yin X.; Giessen H., Formation of chiral fields in a symmetric environment. *Opt. Express*, *20* (24), 26326-26336. (2012).

53 Hashiyada S.; Narushima T.; Okamoto H., Active control of chiral optical nearfields on a single metal nanorod. *ACS Photonics.6* (3), 677-683. (2019).

54 Hashiyada S.; Narushima T.; Okamoto H., Active control of chiral optical nearfields on a single metal nanorod. *ACS Photonics*, 6 (3), 677-683. (2019).

55 Degiron A., Lezec H., Yamamoto N., Ebbesen T., Optical transmission properties of a single subwavelength aperture in a real metal. *Opt. Commun*., 239 (1-3), 61-66. (2004).

56 Curto A. G., Optical antennas control light emission. *Universitat Politècnica de Catalunya*, (2014).

57 Park Y., Kim J., Roh Y.-G., Park Q.-H., Optical slot antennas and their applications to photonic devices. *Nanophotonics*, 7 (10), 1617-1636. (2018).

58 Grosjean T., Mivelle M., Baida F., Burr G., Fischer U., Diabolo nanoantenna for enhancing and confining the magnetic optical field. *Nano. Lett*., 11 (3), 1009-1013. (2011).

59 Ögüt B., Vogelgesang R., Sigle W., Talebi N., Koch C. T., van Aken P. A., Hybridized metal slit eigenmodes as an illustration of Babinet's principle. *ACS Nano*, 5 (8), 6701-6706. (2011).

60 Singh A., Calbris G., van Hulst N. F., Vectorial Nanoscale Mapping of Optical Antenna Fields by Single Molecule Dipoles. *Nano. Lett.*, 14 (8), 4715-4723. (2014).

61 Schäferling M., Yin X., Giessen H., Formation of chiral fields in a symmetric environment. *Opt. Express*, *20* (24), 26326-26336. (2012).

62 Hashiyada S., Narushima T., Okamoto H., Active control of chiral optical nearfields on a single metal nanorod. *ACS Photonics.6* (3), 677-683. (2019).

63 Jackson J. D., Classical electrodynamics. *American Association of Physics Teachers*: (1999).

64 Hashiyada S., Narushima T., Okamoto H., Imaging chirality of optical fields near achiral metal nanostructures excited with linearly polarized light. *ACS Photonics*, *5* (4), 1486-1492. (2018).

65 Molesky S., Lin Z., Piggott A.Y. et al. Inverse design in nanophotonics. *Nature Photon* 12, 659–670. (2018).

66 Sheppard C. J. R., Jones and Stokes Parameters for Polarization in Three Dimensions. *Physical Review A* 90, no. 2. (2014).

67 Setala T., Shevchenko A., Kaivola M., and Friberg A. T., Degree of Polarization for Optical nearfields. *Phys Rev E Stat Nonlin Soft Matter Phys* 66, no. 1 Pt 2: 016615. (2002).

68 Bliokh, K. Y. and Nori F., Transverse and longitudinal angular momenta of light. *Physics Reports* 592: 1-38. (2015).